Anderson Localization: A Density Matrix Approach

Ziyue Qi,[1,2] Yi Zhang,[3,4,*] Mingpu Qin,[5,†] Hongming Weng,[1,2,‡] and Kun Jiang[1,2,§]

[1]Beijing National Laboratory for Condensed Matter Physics and Institute of Physics, Chinese Academy of Sciences, Beijing 100190, China
[2]University of Chinese Academy of Sciences, Beijing 100190, China
[3]Department of Physics and Institute for Quantum Science and Technology, Shanghai University, Shanghai 200444, China
[4]Shanghai Key Laboratory of High Temperature Superconductors, Shanghai University, Shanghai 200444, China
[5]Key Laboratory of Artificial Structures and Quantum Control (Ministry of Education), School of Physics and Astronomy, Shanghai Jiao Tong University, Shanghai 200240, China

(Received 8 October 2025; accepted 29 January 2026; published 2 March 2026)

Anderson localization is a quantum phenomenon in which disorder localizes electronic wave functions. In this work, we propose a new approach to study Anderson localization based on the density matrix formalism. Drawing an analogy to the standard transfer matrix method, we extract the localization length from the modular density matrix in quasi-one-dimensional systems. This approach successfully captures the metal-insulator transition in the three-dimensional Anderson model and in the two-dimensional Anderson model with spin-orbit coupling. It can be also readily extended to multi-orbital systems. We further generalize the formalism to interacting systems, showing that the one-dimensional spinless attractive model exhibits the expected metallic phase, consistent with previous studies. More importantly, we demonstrate the existence of a two-dimensional metallic tendency in the presence of Hubbard interactions and disorder. This method offers a new perspective on Anderson localization and its interplay with interactions.

DOI: 10.1103/y5kd-7prs

Subject Areas: Condensed Matter Physics

I. INTRODUCTION

In real materials, the presence of disorder or imperfections is inevitable which can strongly influence their physical properties. Depending on its strength, disorder can either serve merely as a small perturbation that slightly alters transport properties, or can play a decisive role in reshaping the ground state of a system [1–4]. So it is a central ingredient in understanding the electronic, optical, and magnetic responses of condensed matter systems. An iconic example of disorder-induced phenomena is Anderson localization [5], introduced by P. W. Anderson in 1958 [6]. Anderson localization is a fundamental quantum phenomenon in which disorder prevents electronic wave functions from spreading through the system, leading to the absence of diffusion.

The Anderson localization theory has been extremely successful over the past sixty years, providing a deep understanding of how disorder alone can localize electronic states and suppress transport [2,4]. A wide range of powerful methods have been developed to study this phenomenon, including scaling theory [7–10], perturbation theory [3,11–13], disorder numerical methods [4,14–17], and field-theoretical approaches [18,19]. On the other hand, the interplay between interaction and disorder remains far less understood. While interactions can fundamentally alter localization by giving rise to phenomena such as many-body localization or correlated insulating phases, a comprehensive theoretical framework that unifies disorder and interaction effects is still an open challenge in condensed matter physics [20]. In this work, we introduce a different perspective on Anderson localization based on the density matrix formalism. We find that this formalism is applicable to both noninteracting and interacting systems.

In general, the essential distinction between a localized state and an extended state lies in the nature of their wave functions [1,2,4]. In a translationally invariant metal, electronic states are well described by extended Bloch waves, which remain delocalized across the entire system,

*Contact author: zhangyi821@shu.edu.cn
†Contact author: qinmingpu@sjtu.edu.cn
‡Contact author: hmweng@iphy.ac.cn
§Contact author: jiangkun@iphy.ac.cn

Published by the American Physical Society under the terms of the Creative Commons Attribution 4.0 International license. Further distribution of this work must maintain attribution to the author(s) and the published article's title, journal citation, and DOI.

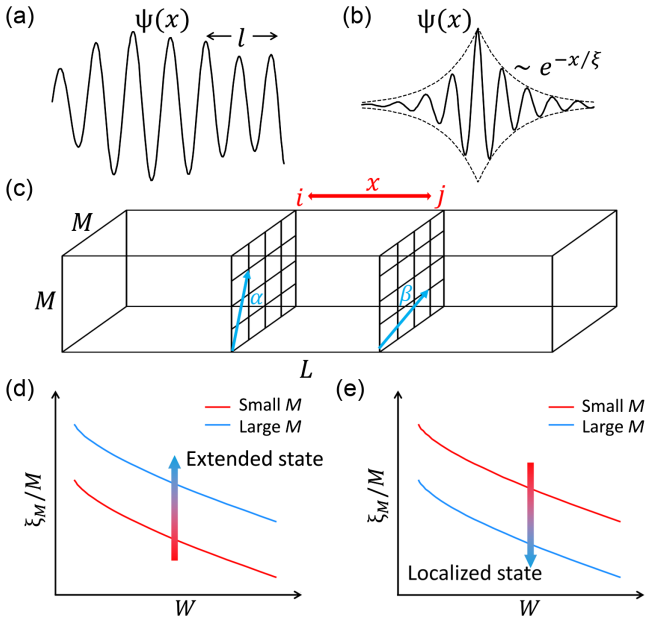

FIG. 1. Schematic diagrams of wave function localization and finite-size scaling in disordered systems. (a),(b) Schematic of the real-space distribution of the extended and localized wave function, respectively. The extended state exhibits undamped oscillations with finite mean free path l, whereas the localized state decays exponentially as $e^{-x/\xi}$. (c) The quasi-1D system of width M and length L, α and β are the site indices in the slice i and j, respectively. x represents the distance between slice i and j. (d),(e) Schematic of the finite-size scaling law of the dimensionless ratio ξ_M/M, which increases with M for the extended states and decreases with M for the localized states.

even in the presence of scattering from a random potential, with a finite mean free path l, as illustrated in Fig. 1(a). In contrast, when disorder becomes sufficiently strong, the wave function can transition to a localized form, where its amplitude decays exponentially away from some spatial point as $e^{-x/\xi}$, as illustrated in Fig. 1(b). Here, ξ denotes the localization length, characterizing the spatial extent of the localized state.

Numerical simulations have played a crucial role in advancing the theory of Anderson localization, particularly through finite-size scaling analysis [5]. While extracting true thermodynamic quantities directly from finite-size systems is challenging, scaling behavior offers valuable insights into localization phenomena [8–10]. A prime example is the remarkable success of the single-parameter scaling approach applied to the conductance $g(L)$ of a system with linear size L [7]. This framework established the foundational result that Anderson localization is especially significant in dimensions ≤ 2 [7].

The same spirit is further generalized to the transfer matrix method (TMM) [14,21,22]. TMM is based on the fact that all one-dimensional (1D) systems are localized in the presence of disorder [7]. In TMM, the Schrödinger equation for a quasi-1D system of width M and length L is reformulated as a recursive propagation along the longitudinal direction, as shown in Fig. 1(c). The asymptotic growth of the total transfer matrix over length L defines the finite-width localization length ξ_M, determined from the smallest positive Lyapunov exponent [14,21,22]. Additional details on the TMM can be found in Appendix A 1. Finite-size scaling is then carried out using the dimensionless ratio $\Lambda_M = \xi_M/M$ [14,21–23], analyzed as a function of disorder strength W. As illustrated in Figs. 1(d)–1(e), ξ_M generally decreases with increasing W. However, the scaling of Λ_M with M reveals two distinct behaviors: if Λ_M increases with M, the system flows to an extended (metallic) phase in the thermodynamic limit [see Fig. 1(d)], whereas a decreasing Λ_M with M signals a localized (insulating) phase [see Fig. 1(e)]. We will use this idea repeatedly in our following discussion. In this paper, for clarity we denote the localization length of quasi-1D systems as ξ_M, with M the system width, and omit the subscript for purely 1D systems, writing it simply a ξ.

Besides TMM, a variety of other important approaches have been developed to investigate Anderson localization. These include the coherent potential approximation (CPA) [15,24], typical medium theory (TMT) [16], and its cluster extension, the typical medium dynamical cluster approximation (TMDCA) [17], as well as the localization criterion on the sensitivity to boundary conditions [25], perturbation theory [2,3], the nonlinear σ model [18,26–28], and the self-consistent theory of localization [29]. Numerical and statistical approaches such as exact diagonalization (ED) [30], the inverse participation ratio (IPR) [28,31–33], energy-level statistics [33–36], multifractal analysis [37–39], and entanglement entropy [40–46] have also provided valuable insights, while Wannier function analysis [47–50] offers an alternative perspective on localization phenomena. All these methods lead to a comprehensive understanding of Anderson localization [5].

On the other hand, the density matrix is a powerful formalism in quantum mechanics and quantum statistical mechanics [51]. Mathematically, the density matrix encodes all measurable information about a system, enabling the calculation of probabilities and correlations. In many-body physics and condensed matter theory, the density matrix plays a central role in understanding transport properties, entanglement structure, and quantum statistical mechanics. Its versatility makes it an indispensable tool across fields ranging from quantum information to strongly correlated electron systems [52,53]. It is natural to ask whether the density matrix can also reveal information about localization. As discussed above, the TMM extracts localization through the localization length ξ_M. Thus, the central question we aim to address in this work is how the localization length can be directly obtained from the density matrix.

The paper is organized as follows. In Sec. II, we present the one-particle density matrix approach for noninteracting disorder systems via the modular density matrix. Then, we

benchmark it against the TMM for both the 3D Anderson model (Sec. II A) and the 2D spin-orbit coupled Anderson model (Sec. II B), finding exact agreement in both localization lengths and critical disorder values. Section II C extends the method to a multi-orbital setting and benchmarks it against TMDCA. In Sec. III, we generalize the modular density matrix to interacting systems through the many-body subtraction density matrix, verifying its consistency in the 1D spinless interacting fermion model (Sec. III B). More importantly, in Sec. III C we uncover a correlated metallic tendency in the 2D Anderson-Hubbard model at $n = 4/15$. The summary and outlook are given in Sec. IV.

II. NONINTERACTING SYSTEM

In this section, we focus on the Anderson localization problem in non-interacting systems. To illustrate our approach more clearly, we begin with simple, intuitive examples by considering a one-dimensional chain. An extended state with momentum k can be written as $|\psi_k\rangle = \sum_i e^{ikx_i} c_i^\dagger |\mathrm{vac}\rangle$ while a localized state may be represented as $|\psi_l\rangle = \sum_i e^{-x_i/\xi} c_i^\dagger |\mathrm{vac}\rangle$, where the normalization factors are omitted for simplicity. From these states, the one-particle density matrix can be evaluated through $\rho(x) = \langle\psi|c_0^\dagger c_x|\psi\rangle$ between site 0 and site at x. Then, we have

$$\rho(x) \propto \begin{cases} e^{ikx}, & \text{extended} \\ e^{-x/\xi}, & \text{localized.} \end{cases} \tag{1}$$

Thus, for localized wave functions, the density matrix naturally contains the information about the localization length ξ.

Building on this observation and the scaling philosophy of the TMM, we propose a generalized modular density matrix (MDM) method to extract the localization length in quasi-1D systems. The overall procedure is illustrated in Fig. 2. As an example, we consider the quasi-1D single-orbital Anderson model described by the spinless fermion Hamiltonian

$$H = -t \sum_{\langle (i,\alpha),(j,\beta)\rangle} c_{i,\alpha}^\dagger c_{j,\beta} + \sum_{(i,\alpha)} \epsilon_{i,\alpha} n_{i,\alpha}, \tag{2}$$

where t denotes the nearest-neighbor hopping amplitude and $\epsilon_{i,\alpha}$ is the on-site random potential, uniformly distributed within $[-W, W]$. i and j index slices along the longitudinal direction, and α, β denote internal site index within a slice, as illustrated in Fig. 1(c).

We first describe the computational workflow in the simplest case of a purely 1D chain, where each slice contains a single site (i.e., $\alpha = \beta = 1$). We begin by generating N_s disorder realizations of such 1D chains with length L [Fig. 2(a)]. Each sample is diagonalized to obtain eigenenergies E_n and eigenstates $|\psi_n\rangle$ ($n = 1, 2, \ldots, L$). For each sample, we select the single-particle eigenstate $|\psi_{s,E_F}\rangle$ (s labeling the index of a disorder realization) whose energy is closest to the Fermi level E_F, as illustrated in Fig. 2(b). Since only this eigenstate is needed, Lanczos-based sparse diagonalization [54,55] can be used to efficiently extract it.

For quasi-1D systems with internal degrees of freedom (α, β) within each slice, it follows the same computational procedure to obtain $|\psi_{s,E_F}\rangle$ as illustrated above for the 1D case. From these states, we define the general MDM in the quasi-1D case as

$$\rho^m_{\alpha\beta}(x) := \frac{1}{\mathcal{N}} \sum_{s=1}^{N_s} \sum_i |\langle\psi_{s,E_F}|c_{i,\alpha}^\dagger c_{i+x,\beta}|\psi_{s,E_F}\rangle|, \tag{3}$$

where $\mathcal{N}$ is a normalization factor and $\rho^m_{\alpha\beta}(x)$ denotes the (α, β)-th matrix element of $\rho^m(x)$. The dimension of $\rho^m(x)$ corresponds to the total number of sites per slice. To extract the slowest decaying channel of $\rho^m(x)$, we further define

$$\gamma(x) := \lambda_{\max}[\rho^{m\dagger}(x)\rho^m(x)] \tag{4}$$

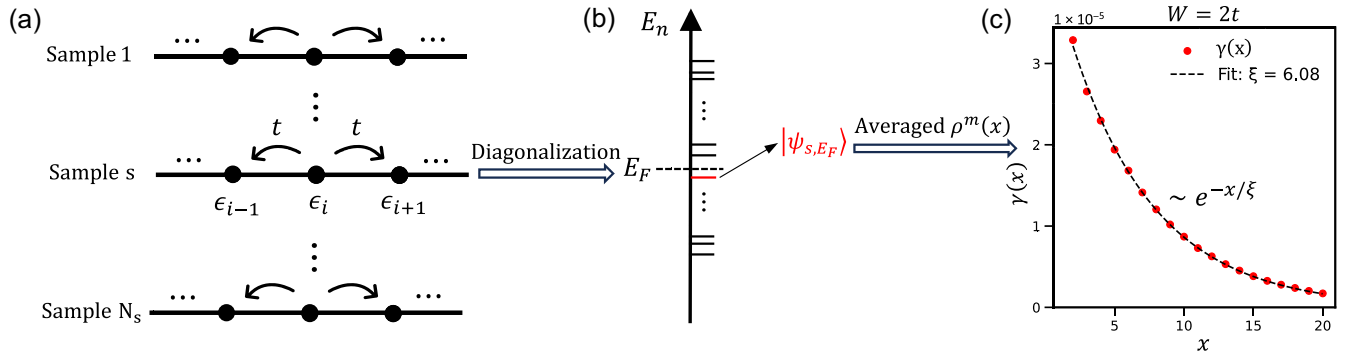

FIG. 2. Computational workflow for extracting the localization length from the MDM in one-dimensional noninteracting systems. (a) Schematic of different disorder samples with hopping energy t and on-site random potential ϵ_i. For each disorder sample, the single-particle eigenstate with the energy level E_n nearest to the Fermi energy E_F is chosen to calculate $\rho^m(x)$, as illustrated in (b). (c) $\gamma(x)$ as a function of x for the systems with disorder strength $W = 2t$, which exhibits exact exponential decay with a localization length $\xi = 6.08$. Panel (c) is calculated by averaging 500 disorder realizations of length $L = 120$ under periodic boundary condition at $E_F = 0$.

where $\lambda_{\max}[\cdot]$ denotes the largest eigenvalue of the Hermitian matrix $\rho^{m\dagger}(x)\rho^{m}(x)$. In the simplest case of a 1D single-orbital chain, the MDM reduces to a scalar with $\gamma(x) = |\rho^{m}(x)|^2$. The symmetrization guarantees that $\gamma(x)$ is real and positive, eliminating ambiguities from complex phases.

Physically, $\gamma(x)$ represents the slowest decaying mode of $\rho^{m}(x)$, directly analogous to the smallest positive Lyapunov exponent in TMM [14,21,22]. A detailed discussion of the connection between the MDM approach and the TMM framework is provided in Appendix A. After averaging over slices and disorder realizations, $\gamma(x)$ exhibits the expected exponential decay, $\gamma(x) = Ae^{-x/\xi}$, from which the localization length ξ can be directly extracted. An example for a 1D noninteracting chain with $W = 2t$ is shown in Fig. 2(c), where ξ is determined to be 6.08. Numerically, all localization lengths ξ for systems with fixed width reported in this work have been verified to be converged with the length of the studied systems, as discussed in the Appendix. B 4.

The term "modular" in MDM highlights that the modulus of the one-particle density matrix is used as the basic building block, while averaging over sites and disorder realizations guarantees the statistical stability. Taking the modulus is crucial because a localized wave function generally consists of an exponential decaying envelope multiplied by a rapidly varying random phase factor, which can be written as $\psi(x) = f(x)e^{-|x-x_0|/\xi}$. Here, $f(x)$ encodes the information of random prefactors. Correspondingly, the density matrix without modulus is $\rho(x_0, x) = \psi^*(x_0)\psi(x) = f^*(x_0)f(x)e^{-|x-x_0|/\xi}$, which also carries the randomly varying factor $f^*(x_0)f(x)$; as a consequence, even after averaging over sites and disorder realizations, the decaying mode still exhibits pronounced oscillations and randomness, thereby obscuring the intrinsic exponentially decaying mode. The modular operation eliminates these random phase fluctuations and therefore exposes a clean decay mode governed by ξ as $e^{-x/\xi}$, yielding a numerically robust estimator of the localization length. A more detailed analysis and explicit comparisons between the results of the modular and nonmodular density matrices are provided in Appendix C 1.

A. MIT in a 3D Anderson model

To benchmark our method, we start to apply the MDM approach to the standard 3D Anderson model. This model is defined on a cubic lattice with nearest-neighbor hopping and on-site random potential, taking the same quasi-1D Hamiltonian form as in Eq. (2). It is well established that the system undergoes a metal-insulator transition (MIT) at a critical disorder strength $W_c \approx 8t \sim 8.5t$ for $E_F = 0$ [23,39,56,57], and also exhibits an energy-dependent mobility edge [58–61].

We first focus on the case $E_F = 0$ by tuning the disorder strength W. As shown in Fig. 3(a), the localization length can be extracted from $\gamma(x)$ and analyzed using finite-size scaling within the MDM framework. Two distinct regimes are clearly observed: for $W < W_c \approx 8.3t$, the ratio ξ_M/M increases with system width M, signaling extended states; whereas for $W > W_c \approx 8.3t$, ξ_M/M decreases with M, indicating localized states. This distinct behavior is the hallmark of MIT. For comparison, we also perform the TMM calculation, shown in Fig. 3(e). Remarkably, the value of localization lengths ξ_M and the critical disorder strength W_c obtained from MDM are in excellent agreement with those from TMM.

Another characteristic feature of the Anderson model is the presence of a mobility edge, which separates extended and localized states depending on energy [58,59]. To capture this, we vary E_F at a fixed disorder strength W. The results from MDM for the 3D Anderson model at $W = 6t$ are shown in Fig. 3(b). Again, two distinct scaling regimes appear: states near the band center (small E_F) remain extended, while those near the band edges (large E_F) become localized. This behavior is also consistent with the TMM results presented in Fig. 3(f).

We can now determine the phase diagram of the 3D Anderson model [23,39,56,57,60,61], as shown in Fig. 3(c). At $W = 0$, the tight-binding band edge lies at $6t$, separating the metallic phase from the fully gapped region. As disorder strength W increases, the band edges broaden as expected [1], forming the upper boundary indicated by the black dotted line in Fig. 3(c). The black dots are obtained from the stabilized values of the largest eigenenergy averaged over 50 disorder realizations on lattices of size L^d with $L = 100$. Between the metallic region and the gapped region lies the Anderson insulating phase, which has a finite density of states at E_F but remains insulating due to localization. The phase boundary separating the metallic and Anderson insulating phases is obtained independently from both MDM and TMM, with the two methods showing nearly identical results. Hence, our method offers a robust and precise characterization of the 3D Anderson model throughout the entire phase space. Additional finite-size scaling results and analysis of the 3D Anderson model, can be found in Appendix B 1. To extract the critical exponents at the metal–insulator transition and further validate the accuracy of the MDM method, we also carry out a detailed data collapse analysis for the 3D Anderson model in Appendix B 3, obtaining results consistent with previous works [23,56,57].

B. MIT in spinful 2D Anderson model with SOC

According to the single-parameter $g(L)$ scaling theory, all states in a two-dimensional (2D) disordered system are localized [7]. This conclusion, however, is contingent on the system belonging to the orthogonal symmetry class [62]. In the presence of spin-orbit coupling (SOC), spin-rotation symmetry is broken while time-reversal symmetry is preserved, which fundamentally alters the system's classification by moving it into the symplectic class [18,28,62–64].

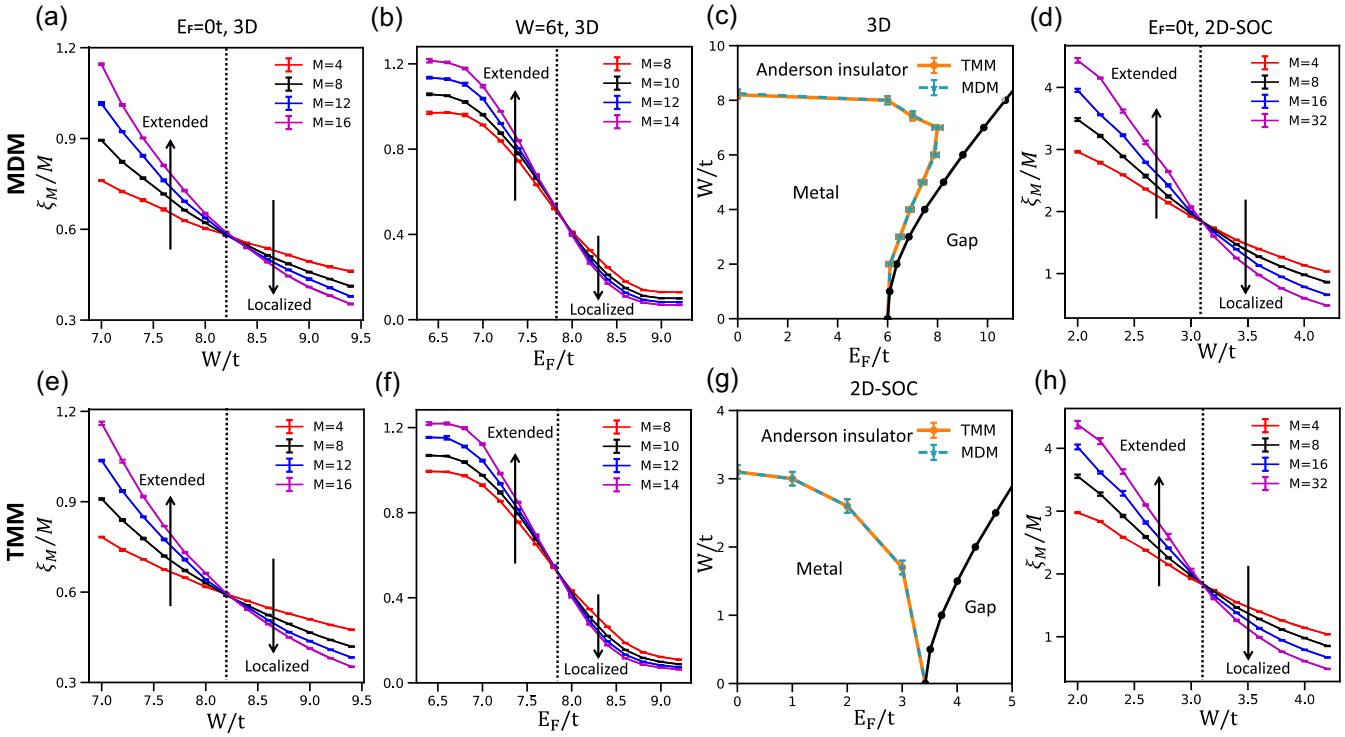

FIG. 3. Comparison of localization length scaling between MDM and TMM. (a)–(b) Finite-size scaling of ξ_M/M obtained from MDM for the 3D Anderson model at $E_F = 0$ as a function of W (a) and at a fixed disorder strength $W = 6t$ as a function of E_F (b). (e)–(f) The corresponding results from the TMM. Black dashed lines mark the metal-insulator transition points. (c),(g) The phase diagrams of the 3D Anderson model and the spinful 2D Anderson model with SOC from both methods, respectively. (d),(h) Finite-size scaling of ξ_M/M for the spinful 2D Anderson model with SOC at $E_F = 0$ from MDM and TMM, respectively. Each ξ_M/M data point from the MDM is obtained by averaging the localization lengths over 5 independent batches of 3000 disorder realizations of size $M^{d-1} \times L$ with $L = 300$ for the 3D Anderson model and $L = 500$ for the 2D Anderson model with SOC (d is the dimension of the considered model), while in TMM each data point is obtained from quasi-1D systems of length $L = 3 \times 10^6$ by averaging over 5 disorder realizations. The error bars are the standard errors of the mean across the 5 independent values. In (c) and (g), the black dotted lines indicate the energy spectral boundaries, determined as stable values of the largest eigenenergy averaged over 50 disorder realizations of size L^d with $L = 100$.

The key physical manifestation of this symmetry change is weak antilocalization (WAL), where destructive quantum interference between time-reversed paths suppresses backscattering [63]. Because this effect counteracts localization, a 2D system in the symplectic class can undergo an Anderson metal-insulator transition, a phenomenon forbidden in the standard orthogonal case.

Given the distinctive localization behavior induced by SOC, we revisit the Anderson metal-insulator transition in a 2D system with SOC using the MDM framework. In particular, we focus on the SU(2) model proposed in Ref. [65], which describes a spinful Anderson system on a square lattice with both random on-site potentials and random SOC. In the quasi-1D system of size $M \times L$, the Hamiltonian of the 2D SU(2) model can be written as

$$H_{\mathrm{SOC}} = -\sum_{\langle (i,\alpha),(j,\beta)\rangle} \sum_{\sigma,\sigma'} t R^{\sigma\sigma'}_{(i,\alpha);(j,\beta)} c^{\dagger}_{i,\alpha,\sigma} c_{j,\beta,\sigma'} + \sum_{(i,\alpha)} \sum_{\sigma} \epsilon_{i,\alpha} n_{i,\alpha,\sigma}. \tag{5}$$

Here, i, j are the slice indices and the α, β are the site indices within a slice following the same convention as that in Eq. (2). The additional ingredient is the spin degree of freedom labeled by $\sigma,\sigma' \in \{\uparrow,\downarrow\}$. Accordingly, in the spinful case, the MDM in Eq. (3) is extended to include the spin indices, such that its elements are written as $\rho^{m}_{\alpha\sigma,\beta\sigma'}(x)$, corresponding to $|\langle \psi_{s,E_F}| c^{\dagger}_{i,\alpha,\sigma} c_{i+x,\beta,\sigma'} |\psi_{s,E_F}\rangle|$ averaged over disorder realizations (s) and slices (i). The on-site disorder $\epsilon_{i,\alpha}$ is uniformly distributed in $[-W, W]$ and the random 2×2 unitary matrices $R^{\sigma\sigma'}_{(i,\alpha);(j,\beta)}$ represent the SOC terms on nearest-neighbor bonds (see Ref. [65] and Appendix B 2 for the definition). This model preserves time-reversal symmetry but breaks spin-rotation symmetry due to SOC, placing the model in the symplectic universality class.

Figure 3(g) shows the phase diagram of the SU(2) model obtained from both MDM and TMM. There are also three different phases: metal, Anderson insulator, and gap phases. Same as the results for the 3D Anderson model presented in the previous subsection, the metal-insulator

phase boundary determined by MDM coincides with that from TMM. We also explore the scaling of ξ_M/M at $E_F = 0$, displayed in Fig. 3(d). For disorder strength below $W_c \approx 3.1t$, the system remains delocalized, while for $W > W_c \approx 3.1t$ it becomes localized. The corresponding TMM results, shown in Fig. 3(h), exhibit the same trend. In contrast, the 2D orthogonal case does not exhibit a metal–insulator transition, as discussed in the Appendix B 2. Together, these findings confirm that the MDM framework provides an accurate and robust description even in systems with spin degree of freedom and complex hopping terms, thereby establishing its applicability to Anderson transitions across different symmetry classes. Additional finite-size scaling results of the 2D Anderson model with SOC can be found in Appendix B 2, and a data collapse analysis can be found in Appendix B 3, where the extracted critical values are consistent with previous works [65,66].

C. MIT in multi-orbital systems

Beyond the single-orbital limit discussed above, realistic materials inevitably involve multi-orbital physics. With several orbitals near the Fermi level, interorbital hybridization and nonlocal disorder effects naturally arise. It is therefore essential to establish that our method can accurately capture the localization transition in such multi-orbital settings. Demonstrating this capability not only validates the robustness of our approach but also opens the path toward its integration with first-principles electronic structure methods, enabling realistic investigations of disorder-driven localization in complex materials. In this section, we benchmark MDM against TMDCA in multi-orbital models. TMDCA [17] is a cluster extension of TMT [16], which generalizes the widely used CPA [15,24] by replacing the arithmetic average of the local density of states (LDOS) in CPA with its geometric average. The resulting average density of states approximates the typical value of the LDOS, denoted as TDOS, which can serve as an order parameter for the Anderson localization transition [37,67–72].

Specifically, we consider a two-orbital Anderson model studied in Ref. [69], defined on a cubic lattice with intra-orbital binary disorder. The Hamiltonian of this two-orbital model (H_{TO}) in the quasi-1D system of length L and width M can be written as

$$H_{TO} = -\sum_{\mu,\nu=1}^{2} \sum_{\langle (i,\alpha),(j,\beta)\rangle} t^{\mu\nu} c^{\dagger}_{i,\alpha,\mu} c_{j,\beta,\nu} + \sum_{\mu=1}^{2} \sum_{(i,\alpha)} \epsilon^{\mu}_{i,\alpha} n_{i,\alpha,\mu}. \tag{6}$$

Here, $\mu,\nu \in \{1,2\}$ denote the orbital degree of freedom, the hopping amplitudes $t^{\mu\nu}$ include both intra-orbital ($\mu = \nu$) and interorbital ($\mu \neq \nu$) terms. The on-site disorder $\epsilon^{\mu}_{i,\alpha}$ acts only within each orbital channel and follows a binary distribution $P(\epsilon^{\mu}_{i,\alpha}) = \frac{1}{2}\delta(\epsilon^{\mu}_{i,\alpha} - W_A) + \frac{1}{2}\delta(\epsilon^{\mu}_{i,\alpha} - W_B)$, so

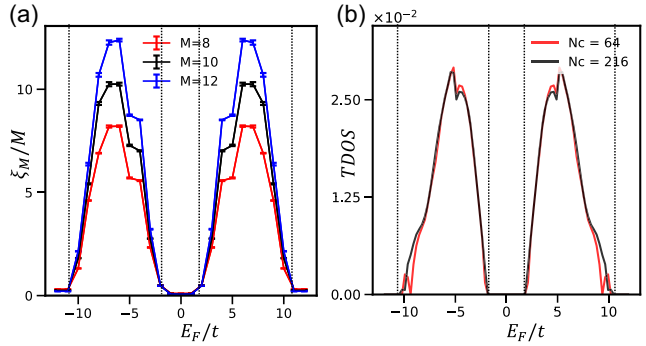

FIG. 4. Comparison of results from MDM and TMDCA for the two-orbital 3D Anderson model at a fix disorder strength of $W = 5t$. (a) Finite-size scaling of ξ_M/M obtained from MDM with system size $M^{d-1} \times L \times 2$ ($L = 300$). Each data point is obtained by averaging the localization lengths over 5 independent batches of 3000 disorder realizations. The error bars are the standard errors of the mean across the 5 batch-averaged values. (b) TDOS obtained from TMDCA with cluster sizes $N_c = 216$ (black) and $N_c = 64$ (red). Model parameters are $t^{11} = t^{22} = t$, $t^{12} = t^{21} = 0.3t$, and $W_A = -W_B = 5t$. Vertical dashed lines in both panels mark the phase boundary between localized and extended states.

that each orbital independently takes the value of random potential as W_A or W_B with equal probability. For the MDM, similar to the case of the spinful Anderson model, the matrix elements of $\rho^m(x)$ for the multi-orbital Anderson model need to carry the additional orbital degree of freedom as $\rho^m_{\alpha\mu,\beta\nu}(x)$, ensuring that both spatial and orbital degrees of freedom are retained.

Compared to the single-orbital Anderson model with a uniform box distribution, this two-orbital model exhibits a distinct phase diagram [69]. The binary distribution of disorder sharpens the separation between extended and localized states, while inter-orbital hopping broadens the effective bandwidth and shifts the mobility edge to higher disorder strengths. As the disorder strength increases, both states near the band center and the band edges begin to localize.

To benchmark our approach, we focus on the scaling of the localization length extracted from MDM at a fixed disorder strength of $W_A = -W_B = 5t$, while scanning the Fermi energy E_F. The scaling results in Fig. 4(a) show that at this disorder strength, the two-orbital model hosts two particle-hole symmetric metallic regions bounded by finite critical energies, separated by a localized phase around the band center. Thus, there are two pairs of phase boundaries, ($\pm E_{Fc1}$, $\pm E_{Fc2}$), separating metallic and insulating states. This behavior is reflected in the scaling of ξ_M/M, which increases with width M in the metallic phase and decreases in the localized phase. The corresponding TMDCA results in Fig. 4(b) shows finite (vanishing) TDOS in the same metallic (localized) regions as that in Fig. 4(a), which serves as the order parameter for the Anderson localization.

The agreement between the two methods is excellent, with nearly identical phase boundaries at $E_{Fc1} \approx \pm 1.8t$ and $E_{Fc2} \approx \pm 10.5t$, as indicated by the vertical dashed lines in Fig. 4. This demonstrates that MDM faithfully reproduces the unique mobility-edge structure of this multi-orbital system. Importantly, it also suggests that the MDM framework can be extended beyond toy models to realistic multi-orbital materials, where orbital complexity plays a crucial role.

Generalizations of localization theory to realistic materials have already been successfully implemented in frameworks such as the TMT [16] and TMDCA [70], both of which can be seamlessly combined with dynamical mean-field theory (DMFT) for strongly correlated systems [73,74]. Similarly, a natural extension of our approach points toward density matrix embedding theory (DMET) [75,76]. Unlike DMFT, which is formulated around the local Green's function, the central object in DMET is the frequency-independent local density matrix. By enforcing a self-consistent match between an impurity cluster and its environment bath, DMET achieves an accurate description of strongly correlated systems directly through the density matrix. This structural similarity suggests that our framework could be seamlessly embedded into DMET, opening a path toward studying localization in realistic multi-orbital and strongly correlated materials. We leave this promising direction for future work.

III. INTERACTION SYSTEM

The theory of Anderson localization in noninteracting systems has been extensively developed over the past sixty years [1,2,5], culminating in a well-established scaling framework. Once electron-electron interactions are included, however, the problem becomes substantially more complex, since interactions can both compete with and enhance disorder effects. Early theoretical progress was made using diagrammatic perturbation theory, which revealed that quantum interference, combined with interactions, leads to nontrivial corrections to conductivity and thermodynamic quantities [3,11–13,19,77]. These approaches laid the groundwork for understanding interaction-induced dephasing, zero-bias anomalies, and Altshuler-Aronov-type corrections [2]. More recently, the study of interacting disordered systems has been revitalized by the study of many-body localization (MBL) [20,78,79], which generalizes Anderson localization to finite energy densities. In this regime, interactions fail to restore ergodicity, leading to localized many-body eigenstates characterized by emergent local integrals of motion. One-particle density matrix has been used to study MBL in previous works [80–82], capturing unique information of many-body localized eigenstates.

Despite these advances, a comprehensive and unified theoretical framework for the interplay between disorder and interactions remains elusive. A central question concerns *whether low-dimensional electronic systems can sustain metallic phases*. The scaling theory of localization predicts the absence of true metallic behavior in two dimensions [7]. However, this long-standing conclusion has been challenged by experiments on 2D electron systems, which provide compelling evidence that an MIT can indeed occur in two dimensions [83–88]. Many attempts have been made to address this issue, including determinant quantum Monte Carlo [89–92], zero-temperature Green function quantum Monte Carlo [93], projector quantum Monte Carlo [94], nonlinear sigma model [95], and Hatree-Fock calculation [96,97]. Here, we aim to approach this problem from the perspective of the density matrix.

However, electron–electron correlations make the diagonalization scheme used in noninteracting systems infeasible, making it impossible to directly obtain the single-particle wave function $|\psi_{E_F}\rangle$ in Eq. (3). Instead, one must work with many-body wave functions. To address this issue, we extend our approach to the interacting case by formulating a many-body version of MDM. Specifically, we introduce a one-particle subtraction density matrix (SDM) $\rho^{\mathrm{sub}}_{(i,\alpha);(j,\beta)}$, defined from the difference between two many-body ground states as

$$\rho^{\mathrm{sub}}_{(i,\alpha);(j,\beta)} = \langle GS_N | c^\dagger_{i,\alpha} c_{j,\beta} | GS_N \rangle - \langle GS_{N-1} | c^\dagger_{i,\alpha} c_{j,\beta} | GS_{N-1} \rangle \tag{7}$$

Where $|GS_N\rangle$, $|GS_{N-1}\rangle$ denote the ground state wave functions with fixed particle numbers N and $N-1$, respectively. The notations i,j label the slice indices along the longitudinal direction, while α, β denote site indices within a slice, following the same convention as in Eq. (3). The diagonal terms of SDM with $(i,\alpha) = (j,\beta)$ have been initially used in quantum chemistry [98] and quasiperiodic 1D systems [99] to capture reactive-ionization hot spots and critical localization, respectively. In our work, we present the use of the off-diagonal terms of the SDM to extract the localization length in interacting many-body systems.

To clarify above definition, we first examine $\rho^{\mathrm{sub}}_{(i,\alpha);(j,\beta)}$ in the noninteracting limit. In this case, the many-body ground states $|GS_N\rangle$ and $|GS_{N-1}\rangle$ are product states of orthogonal single-particle eigenstates $|\psi_n\rangle$ with eigenenergy E_n by

$$|GS_N\rangle = \prod_{n=1}^{N} |\psi_n\rangle = |\psi_{E_F}\rangle \otimes \prod_{n=1}^{N-1} |\psi_n\rangle = |\psi_{E_F}\rangle \otimes |GS_{N-1}\rangle. \tag{8}$$

Using the orthogonality of single-particle eigenstates, one can show that $\rho^{\mathrm{sub}}_{(i,\alpha);(j,\beta)}$ reduces to $\langle \psi_{E_F} | c^\dagger_{i,\alpha} c_{j,\beta} | \psi_{E_F} \rangle$, which is exactly the basic building block of MDM we

used in the noninteracting limit [see Eq. (3)]. A detailed proof of the equivalence between the basic building block of MDM and SDM in the noninteracting limit is provided in Appendix C 2.

We can further go beyond this product state assumption. Suppose we have two normalized ground state wave functions $|GS_N\rangle$ and $|GS_{N-1}\rangle$ connected by a fermionic operator $\hat{\psi}$ as $|GS_N\rangle = \hat{\psi}^\dagger|GS_{N-1}\rangle$. Then, we can prove that $\rho^{\mathrm{sub}}_{(i,\alpha);(j,\beta)}$ just leads to the information of $\hat{\psi}$. More precisely, we can assume that $\hat{\psi}$ has the form $\sum_{i,\alpha} a_{i,\alpha}c_{i,\alpha}$, where the normalization requires $\sum_{i,\alpha}|a_{i,\alpha}|^2 = 1$. Using the anticommutation relations $\{\hat{\psi}, c^\dagger_{i,\alpha}\} = a_{i,\alpha}$ and $\{\hat{\psi}^\dagger, c_{j,\beta}\} = a^*_{j,\beta}$, the SDM defined in Eq. (7) can be rewritten as

$$\begin{aligned}\rho^{\mathrm{sub}}_{(i,\alpha);(j,\beta)} &= \langle \hat{\psi} c^\dagger_{i,\alpha} c_{j,\beta}\hat{\psi}^\dagger\rangle_{N-1} - \langle c^\dagger_{i,\alpha}c_{j,\beta}\rangle_{N-1} \\ &= \langle (a_{i,\alpha} - c^\dagger_{i,\alpha}\hat{\psi})(a^*_{j,\beta} - \hat{\psi}^\dagger c_{j,\beta})\rangle_{N-1} - \langle c^\dagger_{i,\alpha}c_{j,\beta}\rangle_{N-1} \\ &= a_{i,\alpha}a^*_{j,\beta} - a_{i,\alpha}\langle \hat{\psi}^\dagger c_{j,\beta}\rangle_{N-1} - a^*_{j,\beta}\langle c^\dagger_{i,\alpha}\hat{\psi}\rangle_{N-1} \\ &\quad + \langle c^\dagger_{i,\alpha}\hat{\psi}\hat{\psi}^\dagger c_{j,\beta}\rangle_{N-1} - \langle c^\dagger_{i,\alpha}c_{j,\beta}\rangle_{N-1} \\ &= a_{i,\alpha}a^*_{j,\beta}. \end{aligned} \tag{9}$$

Here, $\langle\cdots\rangle_{N-1}$ is a simplified notation of $\langle GS_{N-1}|\cdots|GS_{N-1}\rangle$. The final equality is obtained by using the anticommutation relation $\langle c^\dagger_{i,\alpha}(\hat{\psi}\hat{\psi}^\dagger + \hat{\psi}^\dagger\hat{\psi})c_{j,\beta}\rangle_{N-1} = \langle c^\dagger_{i,\alpha}c_{j,\beta}\rangle_{N-1}$ and $\hat{\psi}|GS_{N-1}\rangle = \hat{\psi}\,\hat{\psi}\,|GS_N\rangle = 0$. Thus, this many-body version of MDM extracts precisely the information connecting $|GS_N\rangle$ and $|GS_{N-1}\rangle$ as $\rho^{\mathrm{sub}}_{(i,\alpha);(j,\beta)} = a_{i,\alpha}a^*_{j,\beta} = \langle\psi|c^\dagger_{i,\alpha}c_{j,\beta}|\psi\rangle$, where $|\psi\rangle = \hat{\psi}^\dagger|0\rangle$.

Consequently, we can define the many-body version of MDM $\rho^m(x)$ in direct analogy with the noninteracting case by averaging the modulus of SDM over sites and disorder samples as

$$\rho^m_{\alpha,\beta}(x) = \frac{1}{\mathcal{N}}\sum_{s=1}^{N_s}\sum_i |\rho^{\mathrm{sub}}_{s,(i,\alpha);(i+x,\beta)}|. \tag{10}$$

Here, the additional index s denotes the disorder realizations. For the noninteracting case, this definition is strictly equivalent to Eq. (3), and directly encodes the localization properties of the single-particle state $|\psi_{E_F}\rangle$. More generally, when the ground states with N and $N-1$ particles, $|GS_N\rangle$ and $|GS_{N-1}\rangle$, are connected by a fermionic operator $\hat{\psi}$, the SDM captures the localization characteristics of $\hat{\psi}$.

It is important to note that in the presence of electron–electron interactions, the simple relation $|GS_N\rangle = \hat{\psi}^\dagger|GS_{N-1}\rangle$ does not hold in general. Nevertheless, for finite-size quasi-1D systems at finite disorder strength, the ground states are always localized except in special cases, and thus we expect to have this localized operator $\hat{\psi}$. While interactions may complicate the precise form of $\hat{\psi}$, the exponential decay of $\rho^m_{\alpha\beta}(x)$ is expected to persist, providing a robust measure of the localization length in strongly disordered interacting systems. More detailed considerations, including extensions of the SDM to spinful systems and higher-order corrections to $\hat{\psi}$, are discussed in the Appendix C 3.

A. Computational workflow

With SDM, the computational workflow for extracting the localization length from the many-body version of MDM is summarized in Fig. 5. Here, we use the spinless fermion model in 1D lattice with interaction and disorder as an example [100,101], which can be written as

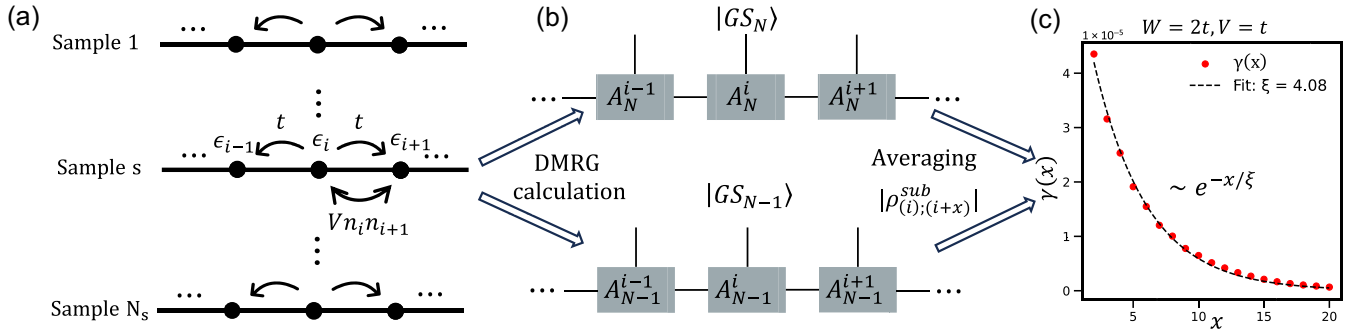

FIG. 5. Computational workflow for extracting the localization length using the many-body extension of MDM approach in spinless 1D interacting systems. (a) Schematic of different disorder samples with hopping energy t, on-site random potential ϵ_i, and nearest-neighbor electron-electron interaction V. For each disorder sample, $|GS_N>$ and $|GS_{N-1}\rangle$ are obtained by performing DMRG calculation, as illustrated in (b). Then the SDM $\rho^{\mathrm{sub}}_{(i);(i+x)}$ can be obtained from the two states according to Eq. (7). A^i_N (A^i_{N-1}) represents the matrix product state of $|GS_N\rangle$ ($|GS_{N-1}\rangle$) at site i. (c) shows $\gamma(x)$ as a function of x for the systems with $W = 2t$ and $V = t$, which exhibits clear exponential decay with a localization length $\xi = 4.08$. (c) is calculated by averaging 500 disorder realizations of length $L = 120$ under open boundary condition at half-filling. In the site averaging for each sample, the 20 sites nearest to each boundary are excluded to minimize open-boundary effects.

$$H_V = -t\sum_{\langle i,j\rangle} c_i^\dagger c_j + V\sum_i n_i n_{i+1} + \sum_i \epsilon_i n_i. \quad (11)$$

Here, t is the nearest-neighbor hopping amplitude, V denotes the strength of nearest-neighbor interaction ($V > 0$ for repulsion and $V < 0$ for attraction), and the on-site random potentials ϵ_i are uniformly distributed within $[-W, W]$ as in noninteracting case [Eq. (2)].

We begin by generating N_s independent disorder realizations of the model in Eq. (11), as illustrated in Fig. 5(a). For each disorder realization, we employ the density matrix renormalization group (DMRG) method [52], as implemented in ITENSOR package [102,103], to compute two ground states $|GS_N\rangle$ and $|GS_{N-1}\rangle$ under open boundary condition (OBC), as illustrated in Fig. 5(b). The DMRG calculations for the spinless 1D model are performed with 330 steps of sweep and the number of kept states is increased gradually to 400, ensuring the convergence and the truncation error $\epsilon < 10^{-10}$. From these two states, we can calculate the SDM $\rho^{\text{sub}}_{(i,\alpha);(j,\beta)}$ ($\alpha = \beta = 1$ in spinless 1D chains) according to Eq. (7). We then construct the many-body version of MDM $\rho^m(x)$ by averaging the modulus of the SDM over sites and disorder samples as in Eq. (10). After symmetrization, the largest eigenvalue of $\rho^m(x)\rho^{m\dagger}(x)$ defines $\gamma(x)$, following the same procedure in Eq. (4). In the regime of sufficiently strong disorder, we find that $\gamma(x)$ still exhibits clear exponential decay even in the presence of electron-electron interactions. Figure 5(c) shows a representative example of disorder strength $W = 2t$ and repulsive interaction $V = t$, where $\gamma(x)$ is well described by $e^{-x/\xi}$ with $\xi = 4.08$. This result demonstrates that the many-body MDM precisely captures the localization information encoded in the operator $\hat{\psi}$ connecting $|GS_N\rangle$ and $|GS_{N-1}\rangle$. Further computational details of DMRG and benchmarks for individual samples with ED in the noninteracting case can be found in Appendix E 1.

B. 1D spinless interaction model

In one-dimensional correlated electron systems, it has long been proposed that the interplay between attractive interactions and Anderson localization can stabilize a delocalized phase [104–111]. For example, a delocalization transition occurs when the Luttinger parameter satisfies $K > 3/2$ in a spinless model within the bosonization framework [104]. Physically, this arises because attractive interactions enhance superconducting quantum fluctuations, which compete with disorder and can ultimately drive delocalization transition [104]. This prediction has been extensively tested through numerical studies using DMRG and related methods [100,101,112–114].

To establish the validity of our method, we investigate how the interaction strength V affects the localization properties in the spinless 1D interacting lattice model at half-filling using our many-body extension of the MDM approach. At relatively weak disorder ($W \sim t$), previous numerical calculations [100,101,112–114] have shown that while repulsive interactions ($V > 0$) enhance localization compared to the noninteracting case, attractive interactions ($V < 0$) can induce nontrivial extended states in 1D, as illustrated in Fig. 6(a). To verify the accuracy of our DMRG calculation in the MDM approach, we first benchmark against the $V = 0$ case, where the model reduces to the noninteracting Hamiltonian and the MDM can be obtained using both DMRG and noninteracting ED. Figure 6(b) shows the results of $V = 0$ and $W = 1$, averaged over the same 500 disorder realizations in DMRG and ED, where DMRG and noninteracting ED yield identical $\gamma(x)$, confirming the reliability of our DMRG calculations.

However, the weak W complicates both the $\gamma(x)$ and the fitting procedure. It is worth noting that in the clean limit ($W = V = 0$) of a 1D nearest-neighbor chain, $\gamma(x)$ can be computed exactly and follows an oscillatory

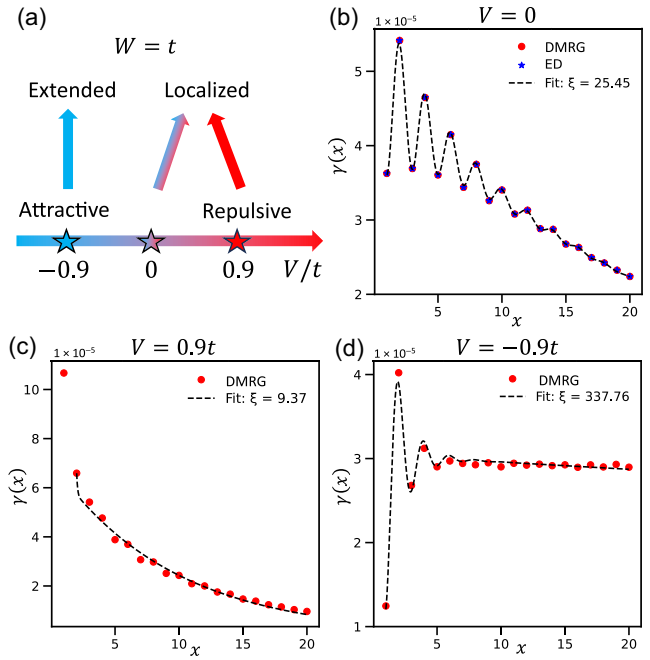

FIG. 6. Results for the 1D spinless interacting chain with finite on-site disorder strength $W = t$ at half-filling. (a) Schematic phase diagram showing that for finite disorder strength ($W = t$), both the noninteracting case ($V = 0$) and repulsive interactions ($V > 0$) correspond to localized states, while at specific attractive interaction strengths ($V < 0$) an extended state emerges. (b)–(d) Display $\gamma(x)$ and their fitting results [using Eq. (12)] for $V = 0t$, $0.9t$, and $-0.9t$ The extracted parameters are $\xi = 25.45, \xi_O = 4.00$ for $V = 0$; $\xi = 9.37, \xi_O \to 0$ for $V = 0.9t$; and $\xi = 337.76, \xi_O = 1.32$ for $V = -0.9t$. Each panel among (b)–(d) is obtained by averaging over 500 disorder realizations of length $L = 120$ under OBC. In the site averaging for each sample, the 20 sites nearest to each boundary are excluded to minimize open-boundary effects. panel (b) is calculated using both ED and DMRG, while panel (c) and (d) are calculated by DMRG.

form determined by the Fermi momentum k_F as $\gamma(x) \sim [1 + \cos(2k_F x)]$. As disorder increases, $\gamma(x)$ crosses over to a purely exponential decay, $\gamma(x) \sim e^{-x/\xi}$. In the intermediate regime of weak disorder, however, the decay is better captured using an exponential decay accompanied by a damped oscillation as

$$\gamma(x) = A \cdot e^{-x/\xi} + B \cdot \cos(2k_F x) e^{-x/\xi_O}, \tag{12}$$

where B is the oscillation amplitude and ξ_O is the oscillation decay length. The fitting result shown in Fig. 6(b) for $W = t$ and $V = 0$ yields $\xi = 25.45$ and $\xi_O = 4.00$, demonstrating that this fitting functional form accurately captures the decay behavior of $\gamma(x)$ in the weak-disorder regime.

Building on the noninteracting benchmark results presented above, we now examine the effects of interactions. For repulsive interaction ($V > 0$), Fig. 6(c) shows the result for $V = 0.9t$ and $W = t$, where $\gamma(x)$ follows clear exponential decay with $\xi = 9.37$ and $\xi_O \to 0$, significantly shorter than the noninteracting value ($\xi = 25.45$ and $\xi_O = 4.00$) at the same disorder strength. This confirms that repulsive interactions enhance localization and also suppress oscillation. We note that the $\gamma(x)$ point at $x = 1$ deviates from the exponential decay trend. We conjecture that this is due to the special form of the nearest-neighbor repulsion, which disfavors double occupation of adjacent sites; thus, we exclude it from the fitting and use the data from $x \geq 2$.

Interestingly, for attractive interactions ($V < 0$), we observe clear evidence of delocalization. As shown in Fig. 6(d), for $V = -0.9t$ and $W = t$, the extracted localization length diverges to $\xi = 337.76$ (with $\xi_O = 1.32$), which is larger than the system size indicating an extended state. In this regime, $\gamma(x)$ remains well captured by the fitting form in Eq. (12), approaching a constant at large x. This result is in full agreement with previous numerical studies [100], which reported the same extended state under identical parameters. Altogether, these findings validate our theoretical analysis and demonstrate that the MDM framework, when combined with the DMRG algorithm, reliably extends to interacting systems and faithfully captures localization-delocalization behavior under both repulsive and attractive interactions. Nevertheless, an exact determination of the transition point in 1D remains challenging within our current approach and will be left for future investigation.

C. 2D Anderson-Hubbard model

With the validity of our method established, we now address the central question of this section: whether metallic phases can exist in two dimensions under the combination of electron correlations and disorder. While previous quantum Monte Carlo studies have hinted at delocalization tendencies, the fermionic sign problem and the analytic continuation are still challenges in quantum Monte Carlo calculations [89–92]. On the other hand, our approach relies only on the ground-state wave function and quasi-1D scaling analysis. Ground states can be obtained with high accuracy, and the quasi-1D geometry is naturally compatible with DMRG simulations, making our method both more reliable and more efficient for tackling this problem.

To address this issue, we apply the many-body MDM approach to the Anderson-Hubbard model on a quasi-1D bar, which is described by the following Hamiltonian

$$H_U = -t \sum_{\langle (i,\alpha),(j,\beta)\rangle} \sum_{\sigma} c^{\dagger}_{i,\alpha,\sigma} c_{j,\beta,\sigma} + U \sum_{(i,\alpha)} n_{i,\alpha,\uparrow} n_{i,\alpha,\downarrow} + \sum_{(i,\alpha),\sigma} \epsilon_{i,\alpha} n_{i,\alpha,\sigma}. \tag{13}$$

Here, i, j and α, β follow the notation introduced earlier, $\sigma \in \{\uparrow, \downarrow\}$ denotes the spin index and $\epsilon_{i,\alpha}$ are uniformly distributed in $[-W, W]$.

It is well known that the Hubbard model hosts a remarkably rich phase diagram with numerous competing orders, most prominently Mott physics at half-filling. In this work, our focus is on the correlated disordered metallic regime. To avoid interference from other ordered phases, we consider an electron filling of $n = 4/15$, which is far away from half-filling. At this density, we expect the $U \to \infty$ limit corresponds to a correlated metal without other competing orders. The problem then reduces to the competition between a correlated metallic state and an Anderson insulator, providing a natural setting to investigate the delocalizing role of Hubbard interactions and the potential existence of a metallic state in disordered 2D systems.

We define the SDM for the Anderson-Hubbard model using the two ground states $|GS_N\rangle$ and $|GS_{N-1}\rangle$ as $\rho^{\mathrm{sub}}_{(i,\alpha);(j,\beta)} = \sum_{\sigma} (\langle c^{\dagger}_{i,\alpha,\sigma} c_{j,\beta,\sigma}\rangle_N - \langle c^{\dagger}_{i,\alpha,\sigma} c_{j,\beta,\sigma}\rangle_{N-1})$. Since the system preserves time-reversal symmetry, the SDM remains the same whether $|GS_N\rangle$ and $|GS_{N-1}\rangle$ differ by a spin-up or a spin-down fermion. Because DMRG calculations remain computationally demanding for $M \geq 4$, our finite-U calculation to extract the localization lengths is restricted to bars of width $M < 4$, which represents the practical computational limit of our study. For $M = 2$, we perform 165 steps of sweep with the number of kept states increasing gradually to 2500, ensuring a truncation error $\epsilon \leq 10^{-8}$; for $M = 3$, 195 steps of sweep are carried out with the number of kept states increasing gradually to 4000, achieving $\epsilon \leq 10^{-6}$. Further computational details and single-sample benchmarks with ED in the noninteracting case ($U = 0$) are presented in Appendix E 1. For comparison, the localization lengths at $U = 0$ are calculated by ED of the noninteracting Hamiltonians in the quasi-1D bars of widths up to $M = 4$ under OBC. These system sizes are

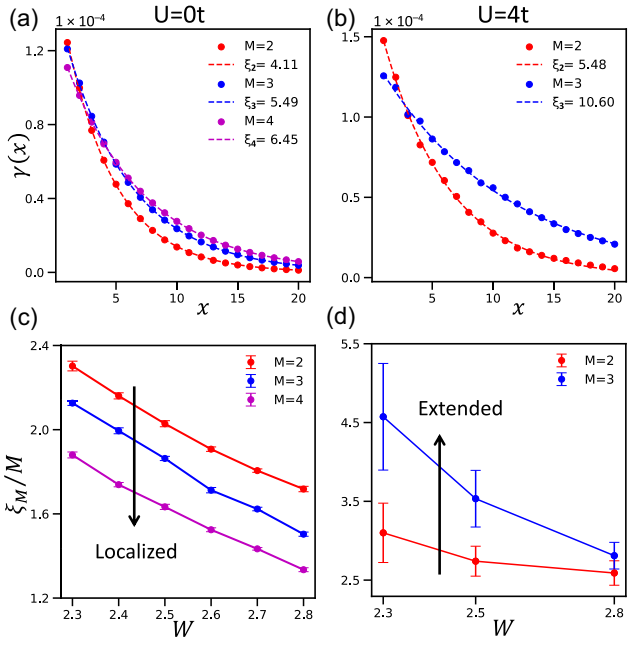

FIG. 7. Results of $\gamma(x)$ and finite-size scaling of ξ_M/M for the quasi-1D Anderson-Hubbard model. (a) The $\gamma(x)$ and exponential fitting results for $M = 2, 3, 4$ in the noninteracting case with $U = 0$ and $W = 2.5t$, which is calculated by ED. (c) The corresponding finite-size scaling of ξ_M/M for $W = 2.3t$–$2.8t$. (b) The $\gamma(x)$ and exponential fitting results for $M = 2, 3$ with $U = 4t$ and $W = 2.5t$, which is calculated by DMRG; (d) the corresponding finite-size scaling of ξ_M/M for $W = 2.3t$–$2.8t$. All disorder realizations are on systems of size $M \times L$ with $L = 60$ under OBC, and in the site averaging for each sample, the 10 sites nearest to each boundary are excluded to minimize open-boundary effects. In (c), data points are obtained by averaging the localization lengths from 10 independent batches of 2000 disorder realizations, with error bars indicating the standard errors of the mean estimated from the 10 independent values. In (d), each point is averaged over 100 realizations, and error bars are standard errors of the mean obtained from five subsets of 20 samples.

already sufficient to capture the finite-size scaling characteristics that distinguish metallic from insulating behavior, as discussed below.

We first examine the noninteracting case with $U = 0$. Within the considered disorder range $W \in [2.3t, 2.8t]$, $\gamma(x)$ exhibits robust exponential decay, $\gamma(x) \sim e^{-x/\xi_M}$, from which the localization lengths ξ_M can be precisely extracted, as shown in Fig. 7(a) for the representative results at disorder strength $W = 2.5t$. The corresponding finite-size scaling of ξ_M/M is presented in Fig. 7(c), which displays clear localized-state scaling behavior as expected. Specifically, for a fixed width M, ξ_M/M decreases as W increases; and for a fixed disorder strength W, ξ_M/M decreases with increasing M, confirming the absence of metallic scaling in the noninteracting case [7].

We then turn to the interacting case with $U = 4$. Remarkably, even in the presence of strong Hubbard interactions, $\gamma(x)$ retains a clean exponential decay form, as shown in Fig. 7(b) for the representative results at disorder strength $W = 2.5t$. Additional numerical results of $\gamma(x)$ and the corresponding exponential fits at other disorder strengths can be found in Appendix E 2. Moreover, for the same disorder strength W and width M, the localization length at $U = 4t$ is significantly larger than that at $U = 0t$, with the enhancement becoming more pronounced as M increases. For example, we have $\xi_2(U = 4t)/\xi_2(U = 0t) \approx 1.33$ while $\xi_3(U = 4t)/\xi_3(U = 0t) \approx 1.93$ at disorder strength $W = 2.5t$. This directly impacts the finite-size scaling of ξ_M/M in Fig. 7(d), where ξ_M still decreases with increasing W; but for fixed W, ξ_M now increases with system width M. Such scaling behavior provides strong evidence for a two-dimensional metallic tendency.

Because of the large computational cost of the Anderson-Hubbard model, our DMRG calculations are currently limited to relatively narrow quasi-1D systems of width $M = 2$ and $M = 3$, so the scaling results can only establish a metallic tendency within the accessible sizes. Nevertheless, we propose that an interaction-induced 2D correlated metallic state can, in principle, emerge. The underlying reason can be understood in the Anderson-Hubbard model. In the noninteracting limit $U = 0$, time-reversal symmetry enforces $\epsilon_{i,\uparrow} = \epsilon_{i,\downarrow} = \epsilon_i$, so that both spin species share the same disorder landscape and a disorder-selected low-energy site is doubly occupied by two particles with opposite spins. When the Hubbard interaction is introduced, however, the term $Un_{i,\uparrow}n_{i,\downarrow}$ imposes an energetic cost on such double occupancy, thereby giving rise to a delocalizing tendency compared to the noninteracting case. To capture the same interaction-induced delocalization effect with much lower computational cost, we construct a modified spinless interacting model and obtain metallic scaling at a finite interaction strength, which provides additional numerical support for a correlated two-dimensional metallic phase. A detailed discussion of the interaction-induced delocalization effect, the modified spinless model construction, and the corresponding finite-size scaling results are presented in Appendix D.

These results demonstrate that interaction-disorder competition can indeed induce a correlated metallic tendency, in contrast to the localized behavior of the noninteracting case. These findings provide direct numerical evidence that Hubbard interactions can play a delocalizing role in disordered 2D systems, establishing a new route to metallicity beyond the conventional Anderson paradigms.

IV. SUMMARY AND OUTLOOK

In this work, we develop a general framework for extracting localization lengths in disordered quantum systems employing the density matrix. By reformulating localization in terms of the modulus of the one-particle

density matrix, our method (MDM) provides a direct and statistically robust way to determine localization lengths in quasi-1D geometries. Benchmarking against the standard transfer matrix method, we show that MDM faithfully reproduces the metal-insulator transition in the 3D Anderson model, captures the energy-dependent mobility edge, and remains consistent across different universality classes, including the 2D spin-orbit coupled case. We further demonstrated that MDM can be readily applied to multi-orbital Anderson systems by benchmarking it against TMDCA for a two-orbital model. These results establish MDM as a reliable and computationally efficient alternative to TMM.

We then generalize the framework to interacting systems through the many-body subtraction density matrix. Using DMRG calculations, we demonstrated that this extension captures localization physics in disordered 1D spinless fermion chains with nearest-neighbor interactions, and reproduces the emergence of extended states at specific attractive interaction strength, consistent with previous numerical studies. Finally, we apply the method to the 2D Anderson-Hubbard model at $n = 4/15$ filling, showing that Hubbard interactions can enhance delocalization and exhibit a metallic tendency with accessible sizes at finite disorder strength in two dimensions. Together, these results establish the MDM framework as a versatile and powerful tool for exploring Anderson localization and its interplay with electronic correlations.

Looking ahead, several promising directions emerge from this work. First, integrating the MDM framework into broader computational approaches, such as density matrix embedding theory and density functional theory, could open powerful routes for investigating localization in realistic materials. Second, the method can be extended to other interacting systems and low-dimensional metal-insulator transitions, including low-density electron gases. Third, the MDM formalism can be naturally combined with other tensor-network algorithms [115,116] (e.g., projected entangled pair states), enabling studies of larger systems and providing new insights into entanglement and localization in many-body settings. Taken together, our study demonstrates that the density matrix framework offers both conceptual simplicity and computational versatility, opening a new perspective on Anderson localization and its extensions to interacting and correlated systems.

ACKNOWLEDGMENTS

We thank Jiale Huang for the useful discussion and help in DMRG. We acknowledge the support by the National Key R&D Program of China (Grants No. 2022YFA1403800 and No. 2022YFA1405400), the National Natural Science Foundation of China (No. NSFC-12274279, No. NSFC-12188101, No. NSFC-12274290, and No. NSFC-12494594), the Chinese Academy of Sciences Project for Young Scientists in Basic Research (2022YSBR-048) and the New Cornerstone Investigator Program. H. W. also acknowledges support from the New Cornerstone Science Foundation through the XPLORER PRIZE.

DATA AVAILABILITY

The data that support the findings of this article are openly available [117].

APPENDIX A: COMPARATIVE FRAMEWORKS FOR LOCALIZATION LENGTH—TRANSFER MATRIX AND MODULAR DENSITY MATRIX

In this section, we provide a systematic analysis and comparison of our MDM approach with TMM, in order to clarify the connections and differences in how the localization length is defined in these two methods. We first review the standard TMM, and then compare it with our newly introduced MDM approach. The analysis highlights both the formal connections and the key differences. We further demonstrate mathematically the equivalence of the localization lengths obtained from the TMM and the MDM approach, which is consistent with our numerical results. For clarity, we denote ξ_{TM} as the localization length obtained from the TMM, and ξ_{MDM} as that from the MDM approach in this section.

1. Transfer matrix method

We first provide a detailed description of TMM [14,21,22] and give the definition of the localization length in this method. Consider a quasi-1D system of width M and length L, the Schrödinger equation for the quasi-1D system can be written as

$$H_i\phi_i + V_{i,i+1}\phi_{i+1} + V_{i,i-1}\phi_{i-1} = E\phi_i. \tag{A1}$$

Here, H_i denotes the block of Hamiltonian matrix elements for the ith slice, $V_{i,i+1}$ represents the block of Hamiltonian matrix elements corresponding to the hopping terms between the ith and $(i+1)$-th slices, and ϕ_i is the component of the eigen-wave function $|\psi_E>$ with eigenenergy E on the ith slice, which can be expressed as $\phi_i = |i\rangle\langle i|\psi_E\rangle$. Based on Eq. (A1), we then define the single transfer matrix $T_i(E)$ between adjacent slices as

$$\begin{pmatrix} \phi_{i+1} \\ \phi_i \end{pmatrix} = T_i(E)\begin{pmatrix} \phi_i \\ \phi_{i-1} \end{pmatrix},$$
$$T_i(E) = \begin{pmatrix} V_{i,i+1}^{-1}(E - H_i) & -V_{i,i+1}^{-1}V_{i,i-1} \\ I_{M^{d-1}\times M^{d-1}} & 0_{M^{d-1}\times M^{d-1}} \end{pmatrix}. \tag{A2}$$

For a system with length L, the total transfer matrix $S_L(E)$ is given by the ordered product of the single transfer matrices $T_i(E)$, which reads

$$S_L(E) = T_L(E)T_{L-1}(E)\cdots T_1(E). \tag{A3}$$

According to the Furstenberg-Kesten law of large numbers [118] and Oseledec's multiplicative ergodic theorem [119] for random matrix products, the localization length is defined in terms of the smallest positive Lyapunov exponent as

$$\xi_{\mathrm{TM}} = \frac{1}{\gamma_1}, \qquad \gamma_1 = \lim_{L\to\infty}\frac{1}{2L} ln(||S_L^{\dagger}(E)S_L(E)||). \tag{A4}$$

The Lyapunov exponent can be obtained stably through iterative QR or SVD decompositions [22]. A detailed analysis of the statistical stability of the localization length ξ_{TM} with increasing length L will be presented later, here we first provide its definition within the TMM framework.

2. Relation between TMM and MDM

The definitions of the localization length from MDM and TMM introduced above can be placed on a common footing by analyzing them from the perspective of single-particle wave functions and their associated density matrices. To clarify the relationships between the localization lengths defined from these two methods, we focus on the 1D case. The conclusions drawn from this analysis also hold for quasi-1D systems by simply adding the internal degrees of freedom within a slice.

In the TMM framework, according to Eq. (A2) and Eq. (A3), the eigenwave function component at the xth site propagated from the reference 0th site can be written as

$$\Phi_x = S_x(E)\Phi_0, \qquad \Phi_x = \begin{pmatrix}\phi_{x+1}\\ \phi_x\end{pmatrix}, \tag{A5}$$

where ϕ_x is the component of the eigenwave function $|\psi_E\rangle$ with eigenenergy E at the xth site, which can be expressed as $\phi_x = \langle x|\psi_E\rangle = \psi_E(x)$ [follow the same convention as in Eq. (A1)]. Then the Euclidean norm of $S_x(E)\Phi_0$ can be expressed in the form of ψ_E as

$$\begin{aligned}||S_x\Phi_0|| = ||\Phi_x|| &= \sqrt{|\psi_E(x)|^2 + |\psi_E(x+1)|^2}\\ &\approx \sqrt{2}\cdot|\psi_E(x)|.\end{aligned} \tag{A6}$$

Combining this with the prerequisite that the wave function component at the reference 0th site is set to unity in TMM, $|\psi_E(0)| = 1$, the Euclidean norm can be rewritten as follow

$$||S_x\Phi_0|| \approx \sqrt{2}\cdot|\psi_E(x)|\cdot|\psi_E(0)| \propto |\langle\psi_E|c_0^{\dagger}c_x|\psi_E\rangle|. \tag{A7}$$

This is precisely the 1D form of the basic building block of the MDM in Eq. (3) in the main text, demonstrating the direct correspondence between the TMM and the MDM.

Up to this point, from the perspective of the eigenwave function and the MDM, we have established that the total transfer-matrix quantity $||S_x(E)||$ is directly correlated with the basic building block of the MDM [Eq. (3)]. Nevertheless, the MDM definition of localization length focuses on the same building block $|\langle\psi_E|c_0^{\dagger}c_x|\psi_E\rangle|$ but employs a different averaging scheme. Instead of taking the limit of $x\to\infty$, one considers the averaged quantity $\sum_i|\langle\psi_E|c_i^{\dagger}c_{i+x}|\psi_E\rangle|$, which collects contributions from all sites separated by distance x. The slowest decaying mode $\gamma(x)$ in the MDM is then fitted to $e^{-x/\xi_{\mathrm{MDM}}}$ to obtain the localization length ξ_{MDM}. This is the core difference between the MDM and TMM framework.

3. The equivalence and statistical stability of ξ_{TM} and ξ_{MDM}

Based on the two definitions of the localization length introduced above, we now provide a mathematical demonstration of their numerical stability after statistical averaging, as well as their equivalence in the localized regime.

We first demonstrate the numerical stability of the localization length ξ_{TM} obtained from the TMM. For convenience, we denote the logarithm of the product transfer matrix norm as $U_x(E) \coloneqq \ln(\|S_x(E)\Phi_0\|)$. The Furstenberg-Kesten law of large numbers [118] and Oseledec's theorem [119] then imply

$$\lim_{x\to\infty}\frac{U_x}{x}\to\gamma_1, \qquad \xi_{\mathrm{TM}} = \frac{1}{\gamma_1}. \tag{A8}$$

Here, γ_1 is the largest positive Lyapunov exponent of $S_x(E)$, which is also named as the first Lyapunov cumulant, representing the mean value of U_x/x.

Beyond the mean value, the central limit theorem for random matrix products [119–121] yields a Gaussian distribution of U_x with finite x, which is

$$\frac{U_x-\gamma_1 x}{\sqrt{x}} \sim \mathcal{G}(0,\gamma_2). \tag{A9}$$

Here, $\mathcal{G}(\mu,\sigma^2)$ denotes the Gaussian distribution with the mean value μ and variance σ^2. γ_2 is named as the second Lyapunov cumulant, representing the variance of $(U_x-\gamma_1 x)/\sqrt{x}$. Equivalently, Eq. (A9) can be rewritten as the distribution of U_x/x with finite x, which reads

$$\frac{U_x}{x}\sim\mathcal{G}\left(\gamma_1,\frac{\gamma_2}{x}\right) \tag{A10}$$

Therefore, as $x\to\infty$, Eq. (A10) reduces to Eq. (A8) with $(\gamma_2/x)\to 0$, yielding a stable localization length $(U_x/x) = (1/\gamma_1) = \xi_{\mathrm{TM}}$.

Nevertheless, in the MDM framework we consider $\rho^m(x)$ at finite x, and thus the variance γ_2 cannot be neglected. After statistical averaging, however, a stable exponential decay can still be obtained in the localized regime. The exponentially decaying mode $\gamma(x)$ [defined in Eq. (4)] extracted from the MDM satisfies

$\gamma(x) = |\rho^m(x)|^2 \propto \langle |\langle \psi_E | c_0^\dagger c_x | \psi_E \rangle| \rangle^2 \propto \langle e^{-U_x} \rangle^2$. According to Eq. (A10), one has $U_x \sim \mathcal{G}(\gamma_1 x, \gamma_2 x)$. Therefore, averaging over samples and sites in Eq. (3) is equivalent to evaluating $\langle e^{-U_x} \rangle^2$ analytically, which can be derived from Gaussian integration as

$$\begin{aligned}\gamma(x) &= |\rho^m(x)|^2 \propto \langle e^{-U_x} \rangle^2 \\ &= \left(\int_{-\infty}^{+\infty} dU_x e^{-U_x} \frac{1}{\sqrt{2\pi\gamma_2 x}} e^{-\frac{(U_x - \gamma_1 x)^2}{2\gamma_2 x}} \right)^2 \\ &= A \cdot e^{-(2\gamma_1 - \gamma_2)x}. \end{aligned} \tag{A11}$$

Here A is a constant coefficients obtained from integration, and the asymptotic decay of MDM is determined by both γ_1 and γ_2 in general.

Notably, previous studies [121] have established that, for 1D and quasi-1D systems in the localized regime with finite variance, short-range disorder, the mean value γ_1, and the variance γ_2 of the logarithmic wave function amplitude are equal, so that

$$\gamma_1 = \gamma_2. \tag{A12}$$

This identity is a hallmark of single-parameter scaling in the localized regime and underlies the log-normal distribution of transmission. The noninteracting systems considered in our work all lie in the localized regime with finite-variance short-range disorder, where single-parameter scaling applies and Eq. (A12) is satisfied. Therefore, the localization length defined via the MDM is theoretically identical to that obtained from the TMM, satisfying

$$\xi_{\mathrm{MDM}} = \xi_{\mathrm{TM}} = \frac{1}{\gamma_1}. \tag{A13}$$

This analytical result is fully consistent with our numerical calculations in Fig. 3 and Appendix B.

APPENDIX B: SUPPLEMENTARY RESULTS OF NONINTERACTING SYSTEMS

In this section, we provide supplementary details and results for the models discussed in the main text, including the single-orbital 3D Anderson model and the spinful 2D Anderson model with random SOC. For the 2D case, we further compare the scaling behavior of the Anderson model with and without SOC. This comparison clearly demonstrates that, in the absence of SOC, all states remain localized for any finite disorder, whereas the presence of SOC places the system in the symplectic universality class, allowing the emergence of a metallic phase at finite disorder and thereby leading to a finite critical disorder strength W_c for metal-insulator transition. To obtain the critical exponents of the metal-insulator transition, we also perform data collapse analysis for the 3D Anderson model and the 2D Anderson model with SOC. Furthermore, we also test the finite-size effect along the longitudinal direction by varying the system length L and guarantee that the conclusions drawn from scaling ξ_M/M are free from finite-size effect of longitudinal system length. All results presented in this section confirm that the localization length extracted from the MDM quantitatively reproduces that from the TMM. These additional results further establish the accuracy and general applicability of the MDM framework to Anderson localization across different dimensions and symmetry classes.

1. 3D Anderson model

The single-orbital 3D Anderson model on a quasi-1D cubic lattice has been defined in the main text [Eq. (2)]. The nearest-neighbor hopping is set to $t = 1$ as the energy unit, and on-site random potentials ϵ_i are uniformly distributed within $[-W, W]$. Figure 8 compares the localization lengths obtained from the MDM and TMM at different fixed Fermi energies E_F as a function of disorder strength W. As E_F deviates from the band center, the critical disorder strength W_c decreases slowly. The transition point W_c separates two regimes: in the metallic phase, ξ_M/M increases with M at fixed W, whereas in the Anderson insulating phase, ξ_M/M decreases with M. Figure 9 presents the complementary analysis at fixed W as a function of E_F. Here, the mobility edge separating extended and localized states is clearly visible. With increasing W, the critical Fermi energy E_{F_c} shifts upward, reflecting the characteristic mobility-edge structure of the 3D Anderson model. In both Figs. 8 and 9, the normalized localization length ξ_M/M and the MIT critical point W_c (E_{F_c}) extracted from the MDM agree precisely with those obtained from the TMM, thereby demonstrating the validity and accuracy of the MDM approach across the entire phase space of the 3D Anderson model.

2. Spinful 2D Anderson model with SOC

The spinful 2D Anderson model with SOC [65] on a quasi-1D square lattice has been defined in the main text [Eq. (5)]. In this model, both the on-site potentials and the nearest-neighbor SOC terms are random. The on-site disorder ϵ_i is uniformly distributed in the interval $[-W, W]$, the nearest-neighbor hopping incorporates random spin rotations described by an SU(2) matrix $R_{(i,\alpha);(j,\beta)}$ acting on the spin space, which is written as

$$\begin{aligned} &R_{(i,\alpha);(j,\beta)} \\ &= \begin{pmatrix} e^{ia_{(i,\alpha);(j,\beta)}} \cos b_{(i,\alpha);(j,\beta)} & e^{ic_{(i,\alpha);(j,\beta)}} \sin b_{(i,\alpha);(j,\beta)} \\ -e^{-ic_{(i,\alpha);(j,\beta)}} \sin b_{(i,\alpha);(j,\beta)} & e^{-ia_{(i,\alpha);(j,\beta)}} \cos b_{(i,\alpha);(j,\beta)} \end{pmatrix}. \end{aligned} \tag{B1}$$

Here, i and j index slices along the longitudinal direction of the quasi-1D bar, and α, β denote internal site degree of freedom within a slice. $a_{(i,\alpha);(j,\beta)}$ and $c_{(i,\alpha);(j,\beta)}$ are

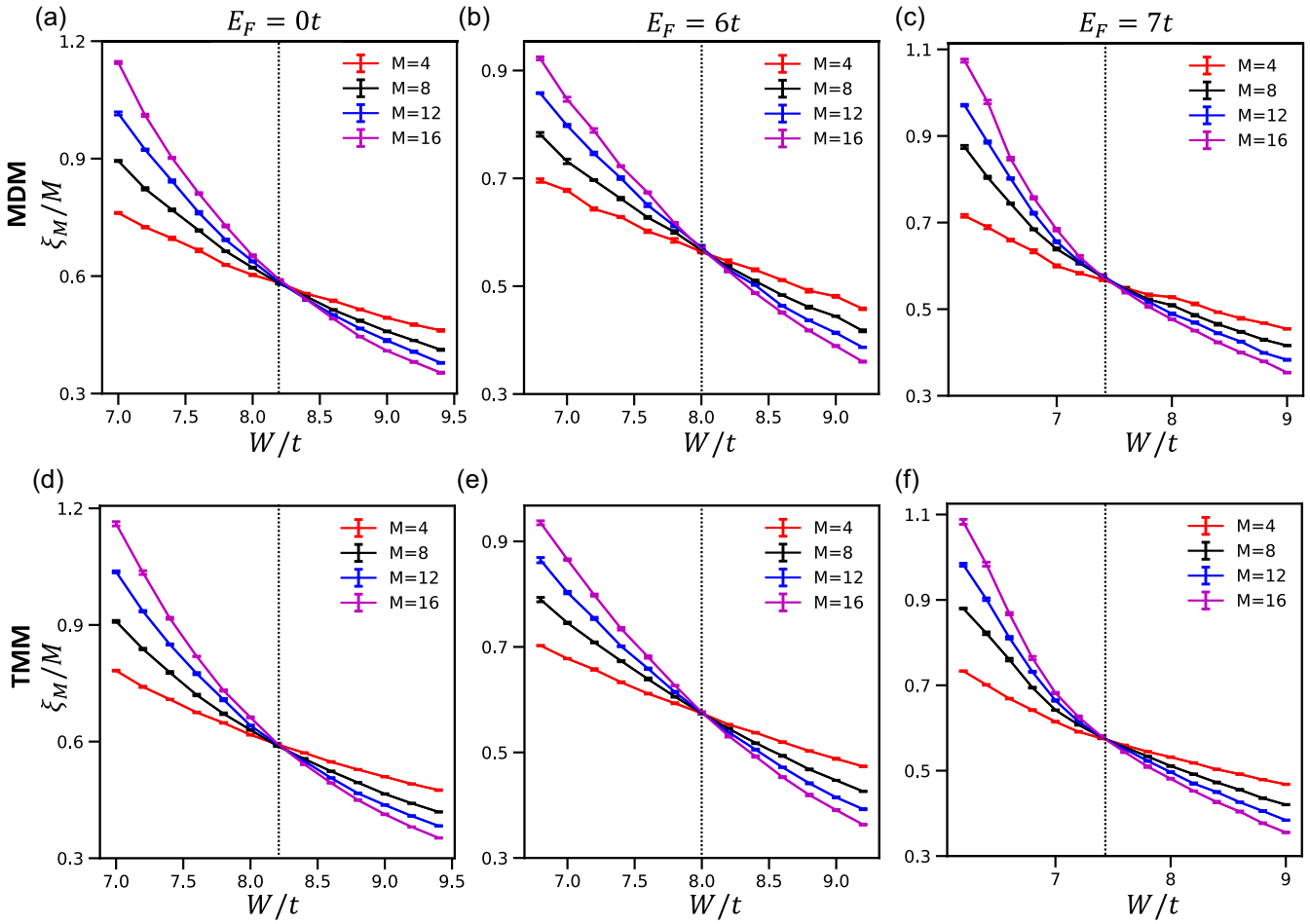

FIG. 8. Comparison of localization length scaling between MDM and TMM for the 3D Anderson model. The plots show ξ_M/M as a function of disorder strength W at fixed Fermi energies $E_F = 0$, 6, 7 for different quasi-1D widths M. (a)–(c) MDM results, and (d)–(f) corresponding TMM results. The critical disorder strengths are $W_c \approx 8.3$, 8.0, 7.4 for $E_F = 0$, 6, 7, respectively. Each ξ_M/M data point from the MDM is obtained by averaging the localization lengths over 5 independent batches of 3000 disorder realizations of size $M^2 \times L$ with $L = 300$, while in the TMM each data is obtained from quasi-1D systems of length $L = 3 \times 10^6$ by averaging 5 disorder realizations. The error bars are the standard errors of the mean across the 5 independent values.

uniformly distributed in $[0, 2\pi)$, while $b_{(i,\alpha);(j,\beta)}$ are distributed with probability density $P(b)db = \sin(2b)db$ for $0 \le b \le 2\pi$. These distributions ensure that $R_{(i,\alpha);(j,\beta)}$ is uniformly distributed with respect to the Haar measure on SU(2) [65]. Hopping matrices on different bonds are statistically independent.

Supplementary localization scaling results from MDM and TMM are shown in Fig. 10. These plots display the scaling of ξ_M/M at fixed Fermi energies as a function of disorder strength W. As the Fermi energy deviates from $E_F = 0$, the MIT critical point W_c gradually decreases. For each system width M, the normalized localization length ξ_M/M decreases monotonically with increasing disorder. The critical point W_c separates the metallic phase, where ξ_M/M increases with M, from the Anderson insulating phase, where ξ_M/M decreases with M.

To highlight the role of symmetry, we also compute the scaling behavior of the 2D Anderson model without SOC [taking the same Hamiltonian form as Eq. (2)], which belongs to the orthogonal class. As shown in Fig. 11, both MDM and TMM confirm that in this case all states remain localized for finite disorder, with no metallic phase [62]. In contrast, with SOC the system belongs to the symplectic class and supports a finite-disorder metallic phase [18,28,62–64]. In both cases (with and without SOC in two dimensions), the localization lengths ξ_M/M obtained from MDM are in quantitative agreement with those from TMM. For the SU(2) model with SOC the critical disorder strengths W_c extracted from two methods also precisely coincide. These results demonstrate the accuracy and reliability of the MDM approach across different universality classes.

3. Data collapse

To obtain the critical information and further validate the accuracy of the MDM method, we perform a detailed finite-

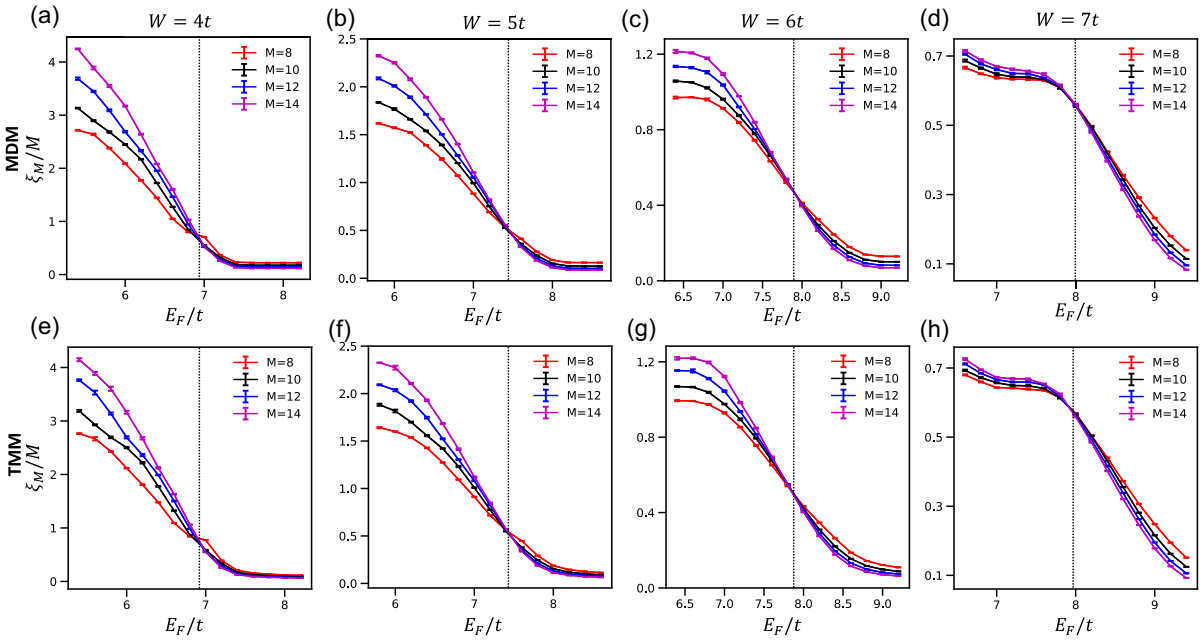

FIG. 9. Comparison of localization length scaling between MDM and TMM for the 3D Anderson model. The plots show ξ_M/M as a function of Fermi energy E_F at fixed disorder strengths $W = 4, 5, 6, 7$ for different quasi-1D widths M. (a)–(d) MDM results, and (e)–(h) corresponding TMM results. The critical Fermi energies are $E_{F_c} \approx 6.9, 7.4, 7.9, 8.0$ for $W = 4, 5, 6, 7$, respectively. Each ξ_M/M data point from the MDM is obtained by averaging the localization lengths over 5 independent batches of 3000 disorder realizations of size $M^2 \times L$ with $L = 300$, while in the TMM each data is obtained from quasi-1D systems of length $L = 3 \times 10^6$ by averaging 5 disorder realizations. The error bars are the standard errors of the mean across the 5 independent values.

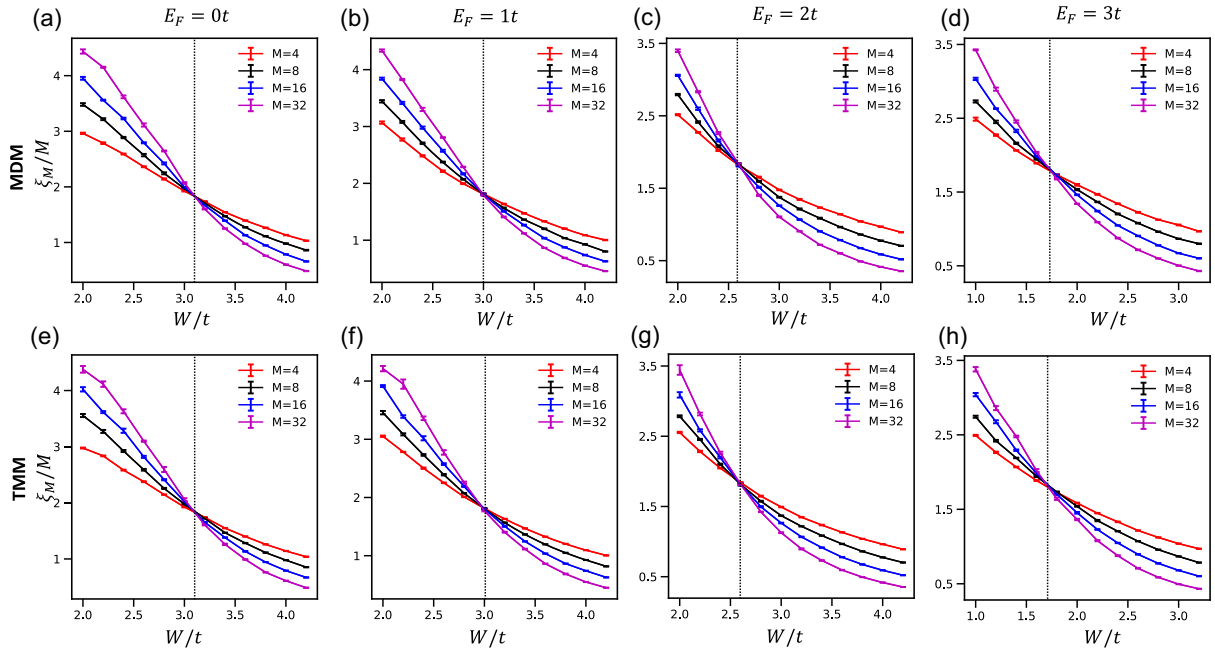

FIG. 10. Comparison of localization length scaling between MDM and TMM for the spinful 2D Anderson model with SOC. The plots show ξ_M/M as a function of disorder strength W at fixed Fermi energies $E_F = 0, 1, 2, 3$ for different quasi-1D width M. (a)–(d) present MDM results, and (e)–(h) show the corresponding TMM results. The critical disorder strengths are $W_c \approx 3.1, 3.0, 2.6, 1.7$ for $E_F = 0, 1, 2, 3$, respectively. Each ξ_M/M data point from the MDM is obtained by averaging the localization lengths over 5 independent batches of 3000 disorder realizations of size $M \times L$ with $L = 500$, while in the TMM each data point is obtained from quasi-1D systems of length $L = 3 \times 10^6$ by averaging 5 disorder realizations. The error bars are the standard errors of the mean across the 5 independent values.

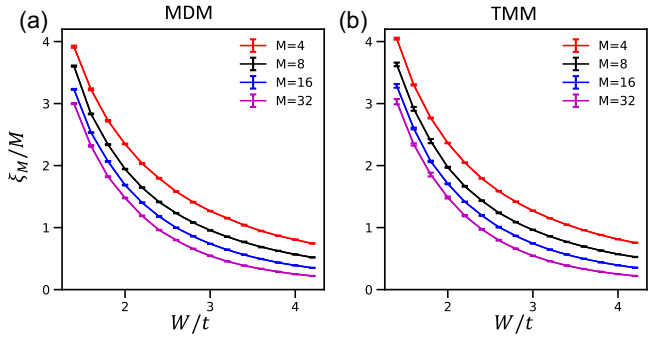

FIG. 11. Comparison of localization length scaling between MDM and TMM for the 2D Anderson model without SOC. The plots show ξ_M/M as a function of disorder strength W at fixed Fermi energy $E_F = 0$ for different quasi-1D width M. (a) MDM result, and (b) corresponding TMM result. Each ξ_M/M data point from the MDM is obtained by averaging the localization lengths over 5 independent batches of 3000 disorder realizations of size $M \times L$ with $L = 500$, while in the TMM each data point is obtained from quasi-1D systems of length $L = 3 \times 10^6$ by averaging three disorder realizations. The error bars are the standard errors of the mean across the 5 independent values.

size scaling analysis and the corresponding data collapse study for the 2D Anderson model with SOC [Figs. 12(a) and 12(b)] and the 3D Anderson model [Figs. 12(c) and 12(d)] at $E_F = 0$ in the vicinity of the metal-insulator transition by following the standard one-parameter scaling theory.

For the data collapse, ξ_M/M is shown as a function of the rescaled variable $x = \ln[M/|(W - W_c)^{-\nu}]$. The resulting data collapses are presented in Fig. 12(b) for the 2D Anderson model with SOC and Fig. 12(d) for the 3D Anderson model, where the critical exponent ν are obtained by fitting to a smooth scaling function $f(x) = [\Lambda_c/(1 + ae^{bx})]$, where ν is contained in x. Combing with the finite-size scaling results in Figs. 12(a) and 12(c), we obtain $\nu = 2.73 \pm 0.02$ and $W_c = 3.09 \pm 0.03$ for the 2D Anderson model with SOC, and $\nu = 1.58 \pm 0.02$ and $W_c = 8.25 \pm 0.03$ for the 3D Anderson model. Above values are fully consistent with the previous works (Refs. [65,66] for the 2D Anderson model with SOC and Refs. [23,56,57] for the 3D Anderson model).

These data collapse results provide additional and more robust support for the accurate identification of the metal-insulator transition using the MDM method.

4. Finite-size effect along the longitudinal direction

In this part, we test the finite-size effect along the longitudinal direction by varying the system length L. In brief, weak disorder is associated with a large intrinsic localization length, which demands larger system sizes to reach convergence. In contrast, strong disorder produces much shorter localization lengths, so the results converge much more rapidly. For all results presented in this paper, we have carefully checked and confirmed their convergence.

Specifically, we compute $\xi(L)$ for a sequence of longitudinal lengths L under various disorder strengths W, and define a finite-size diagnostic

$$\Delta\xi(L_1, L_2) = |\xi(L_1) - \xi(L_2)|, \qquad L_1 < L_2, \qquad \text{(B2)}$$

which directly measures the stability of the extracted localization length with respect to system size. When $\Delta\xi(L_1, L_2)$ becomes sufficiently small or approaches zero, we regard $\xi(L_2)$ as a converged localization length.

As a first example, we examine the finite-size effect in the noninteracting 1D Anderson chain [Eq. (2) in the main text] at half filling with periodic boundary conditions. Figure 13(a) shows that in the weak-disorder regime the extracted localization length $\xi(L)$ depends strongly on the system length L: at $W \simeq 1$, $\xi(L)$ from $L = 60$ and $L = 90$ differs markedly, indicating that $L < 90$ is insufficient

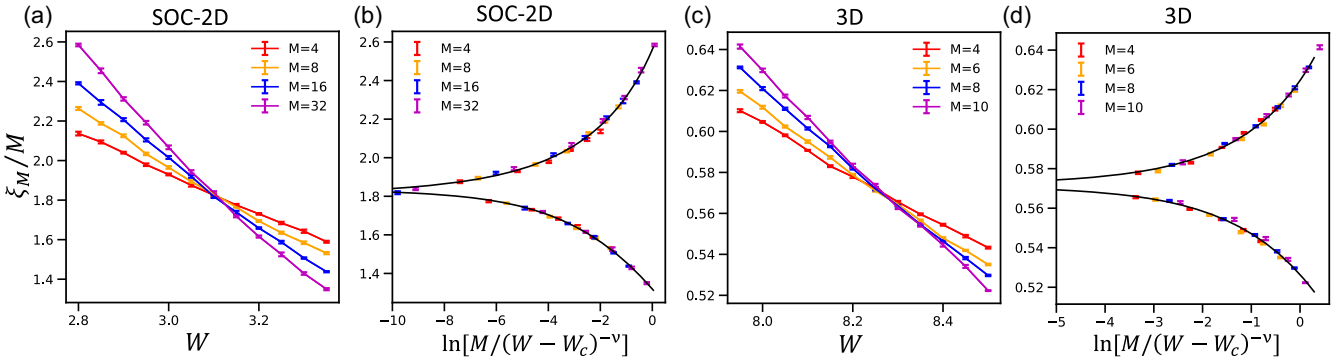

FIG. 12. Finite-size scaling and the corresponding data collapse across the metal-insulator transition point for the 2D Anderson model with SOC (a)–(b) and 3D Anderson model (c)–(d) at $E_F = 0$. Each data point of ξ_M/M is computed for a strip of size $M^{d-1} \times L$ [$L = 500$ for (a)–(b) and $L = 300$ for (c)–(d)] by averaging the localization lengths over 10 independent batches of 2000 disorder realizations from MDM, and the error bar is the standard error of the mean across the 10 batch-averaged values. The fitting functions used in (b) and (d) are $f(x) = \Lambda_c/(1 + a \cdot e^{bx})$. The critical values in (b) are $\nu = 2.73 \pm 0.02$ and $W_c = 3.09 \pm 0.03$, and those in (d) are $\nu = 1.58 \pm 0.02$ and $W_c = 8.25 \pm 0.03$.

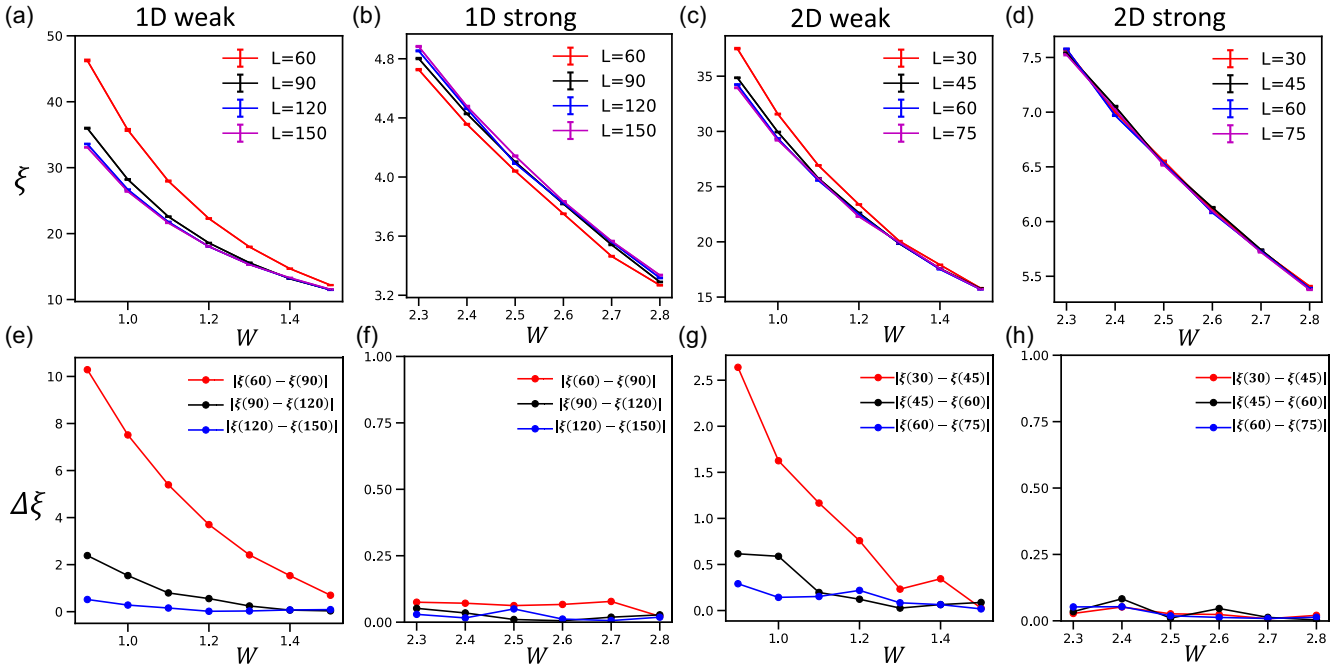

FIG. 13. (a),(b) The localization lengths $\xi(L)$ computed using the MDM method for a noninteracting 1D Anderson chain at half filling under periodic boundary condition, plotted as functions of disorder strength W for several system lengths $L = 60, 90, 120, 150$. (c),(d) The $\xi(L)$ for a quasi-1D system with width $M = 4$ at filling $n = 4/15$ under open boundary condition for several system lengths $L = 30, 45, 60, 75$. All the data in (a)–(d) are calculated by averaging the localization lengths over 10 independent batches of 2000 disorder realization, with error bars indicating standard errors of the mean estimated from the 10 independent subsets. (e)–(h) are the finite-size diagnostic $\Delta\xi(L_1, L_2) = |\xi(L_1) - \xi(L_2)|$ evaluated for the localization length $\xi(L)$ obtained from different system lengths in (a)–(d).

because the intrinsic localization length is very large and requires much longer chains to converge. The curves start to converge for $L \approx 120$–150, suggesting that $L \geq 120$ is needed to suppress finite-size effects. This is quantified in Fig. 13(e): $\Delta\xi(60, 90)$ exceeds 10 at weak disorder and decreases with increasing W, whereas $\Delta\xi(120, 150)$ stays below 0.5 over the entire range, demonstrating that $L \gtrsim 120$ yields reliable ξ. By contrast, in the strong-disorder regime the localization lengths from $L = 60, 90, 120, 150$ differ only slightly and rapidly converge, as seen in Fig. 13(b), consistent with a much smaller intrinsic ξ. Correspondingly, Fig. 13(f) shows $\Delta\xi(L_1, L_2) < 0.1$ in all cases, confirming that $L = 90$ already provides a stable localization length at strong disorder.

As a second example, we consider a quasi-1D noninteracting system with width $M = 4$ at filling $n = 4/15$ under open boundary conditions. Figure 13(c) shows that finite-size effects in the weak-disorder regime are much weaker than in the half-filled 1D case: $\xi(L)$ from $L = 30$, 45, 60, 75 converges rapidly and is essentially saturated by $L = 60$. This is corroborated by the finite-size diagnostic in Fig. 13(g), where $\Delta\xi(30, 45)$ decreases quickly with increasing W, while $\Delta\xi(45, 60)$ and $\Delta\xi(60, 75)$ remain close to zero throughout. In the strong-disorder regime, the localization lengths extracted from all system lengths are nearly identical, with the $\xi(L)$–W curves almost perfectly overlapping in Fig. 13(d); correspondingly, Fig. 13(h) shows $\Delta\xi(L_1, L_2) \approx 0$ even for $L_1 = 30$ and $L_2 = 45$, indicating that $L = 45$ already yields converged ξ for $W \geq 2.3$. These results further confirm that the quasi-1D system sizes used in the main text (Fig. 7) lie safely in the regime where finite-size effects are negligible for the extracted localization lengths.

Taken together, these two representative examples illustrate a clear trend: weak disorder corresponds to a large intrinsic localization length and therefore requires larger system sizes to ensure convergence, while strong disorder leads to much smaller localization lengths, allowing a rapid convergence with respect to L. Across all parameter regimes used in the main text, the values of ξ_M entering the quasi-1D scaling analysis were extracted at system sizes where $\Delta\xi(L_1, L_2)$ is negligibly small. This guarantees that the conclusions drawn from scaling ξ_M/M are free from finite-size effect of longitudinal system length L.

APPENDIX C: PHYSICAL MEANING OF MODULAR DENSITY MATRIX AND SUBTRACTION DENSITY MATRIX

1. Why *modular* is important?

In this part, we provide a more detailed explanation of why the *modular* construction is essential for the extraction

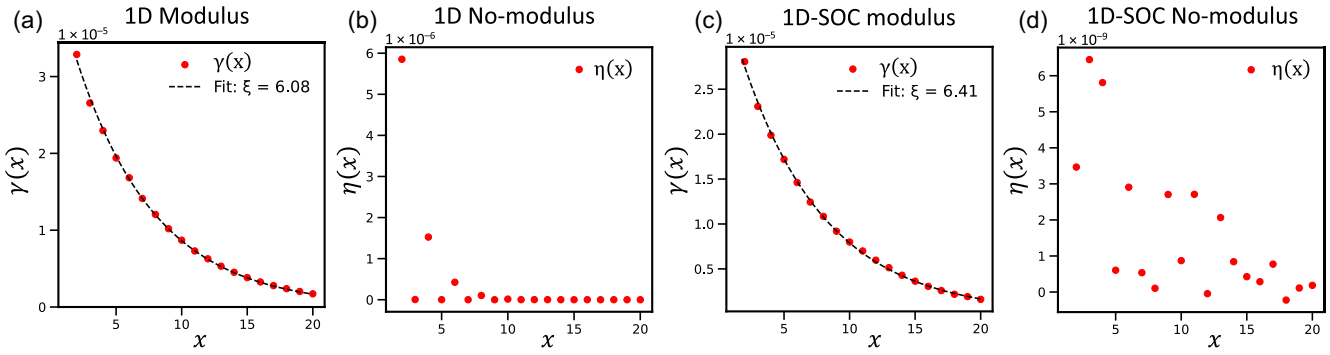

FIG. 14. (a),(b) $\gamma(x)$ and $\eta(x)$ as a function of x for the systems with disorder strength $W = 2t$ in the 1D chain [Eq. (2)] in the main text with quasi-1D width $M = 1$, respectively. (c),(d) $\gamma(x)$ and $\eta(x)$ as a function of x for the systems with disorder strength $W = 2t$ in the 1D SOC chain [Eq. (5)] with quasi-1D width $M = 1$. All above panels are calculated by averaging 500 disorder realizations of length $L = 120$ under periodic boundary condition at $E_F = 0$.

of the localization length compared to the ordinary (nonmodular) density matrix.

In general, the asymptotic form of a localized wave function can be decomposed into two components: an exponentially decaying envelope, $e^{-x/\xi}$, and an oscillatory or random phase factor $f(x)$ as

$$\psi(x) = f(x)e^{-|x-x_0|/\xi}. \tag{C1}$$

The motivation for employing the modular density matrix is precisely to eliminate the influence of the $f(x)$ component. The function $f(x)$ typically contains complicated oscillations and phase structures. In particular, when Hamiltonian and $f(x)$ are complex, wave functions obtained from numerical diagonalization are subject to gauge-fixing ambiguities. Since the primary objective of our method is to extract the localization length ξ associated with the envelope, it is essential to remove the contribution from $f(x)$. And the ξ from the modular density matrix can exactly match with transfer matrix method. This point can be illustrated by the following examples.

Mathematically, the corresponding one-particle density matrix element between a reference site at x_0 and a site at x is

$$\begin{aligned}\rho(x_0, x) &= \langle\psi|c^\dagger_{x_0}c_x|\psi\rangle = \psi^*(x_0)\psi(x) \\ &= f^*(x_0)f(x)e^{-|x-x_0|/\xi}.\end{aligned} \tag{C2}$$

For a given disorder realization this object has an exponentially decaying envelope set by ξ, but the prefactor $f^*(0)f(x)$ carries the rapidly oscillating sign or random phase structure of the localized state. Upon averaging over positions and disorder realizations, these short-scale phase fluctuations distort the averaged amplitude as

$$\langle\rho(x_0, x)\rangle = \langle f^*(x_0)f(x)\rangle e^{-|x-x_0|/\xi}. \tag{C3}$$

Here, $\langle f^*(0)f(x)\rangle$ in general remains an oscillatory or random function of x, rather than a smooth quantity that cleanly tracks the exponential envelope. As a result, the averaged $\rho(0, x)$ no longer exhibits a simple exponential decay and becomes a poor quantitative probe of localization. By contrast, the modular density matrix explicitly removes these random phase fluctuations and oscillations, thereby isolating a clean decaying mode $e^{-|x-x_0|/\xi}$ that directly reflects the localization information, which provides a numerically robust measure for extracting the localization length ξ.

To substantiate the above discussion, we compare the modular and nonmodular construction of density matrices in two explicit noninteracting models: one is 1D systems with nearest-neighbor real hopping and random on-site potential, and another is 1D systems with nearest-neighbor random spin-orbit-coupling hoppings (complex hoppings) and random on-site potential.

In parallel with the definition of MDM in Eq. (3) and Eq. (4) in the main text, we define averaged nonmodular density matrix $\bar{\rho}_{\alpha\beta}(x)$ as

$$\bar{\rho}_{\alpha\beta}(x) := \frac{1}{\mathcal{N}}\sum_{s=1}^{N_s}\sum_i \langle\psi_{s,E_F}|c^\dagger_{i,\alpha}c_{i+x,\beta}|\psi_{s,E_F}\rangle. \tag{C4}$$

Here, i and j index slices along the longitudinal direction, and α, β denote internal site and spin index within a slice, following the same convention in Eq. (3). And the slowest decaying channel of $\bar{\rho}(x)$ is defined as

$$\eta(x) := \lambda_{\max}[\bar{\rho}^\dagger(x)\bar{\rho}(x)], \tag{C5}$$

which follows the same procedure for $\gamma(x)$ and $\rho^m(x)$ in Eq. (4).

As a first example, we consider a 1D noninteracting Anderson chain with nearest-neighbor hopping t and on-site random potential of strength ϵ_n [Eq. (2)] with quasi-1D width $M = 1$; in this case the single-particle Hamiltonian is a real symmetric matrix. Figure 14(a) shows $\gamma(x)$ at disorder strength $W = 2t$, obtained from the modular density matrix defined in Eqs. (3)–(4). The result exhibits a perfect exponential decay as a function of x, from which we extract a localization length $\xi \approx 6.08$. By contrast, Fig. 14(b) displays $\eta(x)$ for the same model and disorder strength,

computed from the nonmodular density matrix $\bar{\rho}(x)$ defined above. $\eta(x)$ shows pronounced oscillations superimposed on a rapidly decaying signal, rather than a smooth single-exponential law, and does not provide a clean or robust way to determine the localization length. This is because the oscillation of the local prefactor $f(x)$ in $\psi(x)$ is retained in $\bar{\rho}(x)$, which makes $\eta(x)$ oscillate as a function of distance and suppressed the intrinsic decaying mode.

The situation becomes even more severe for $\bar{\rho}(x)$ and $\eta(x)$ in the presence of complex matrix elements in the Hamiltonian. As a second example, we consider a 1D chain with nearest-neighbor random SOC hoppings $R_{i,j}^{\sigma,\sigma'}$ and on-site random potential ϵ_n [Eq. (5)]. In this case the single-particle Hamiltonian is a complex Hermitian matrix, and each component of the eigenstate can still be written as $\psi(x) = f(x)e^{-|x-x_0|/\xi}$. However, the local prefactor $f(x)$ now carries an additional complex phase $e^{i\theta(x)}$ that fluctuates randomly along the system. This phase randomness is due to the $U(1)$ gauge freedom at each site. Figure 14(c) shows $\gamma(x)$ for this 1D-SOC model at disorder strength $W = 2t$. Because of the modulus in the definition of MDM, $\gamma(x)$ still exhibits a clear exponential decay as a function of x with localization length $\xi = 6.41$, demonstrating that the modular construction remains robust for the complex Hamiltonian. In stark contrast, Fig. 14(d) displays $\eta(x)$ obtained from the nonmodular density matrix $\bar{\rho}(x)$ for the same SOC model and parameters. Here the phase factor $f(x)$ in $\psi(x)$ enters $\bar{\rho}(x)$ through $\langle f^*(0)f(x)\rangle \sim \langle e^{i[\theta(x)-\theta(0)]}\rangle$, which behaves as an completely random function of x. As a result, $\eta(x)$ shows highly irregular, noiselike fluctuations without a discernible exponential envelope even after averaging over positions and disorder realizations.

In conclusion, above two examples show that modular and nonmodular density matrices behave qualitatively differently: the modular density matrix filters out sign oscillation and random phase fluctuations, and produces a clean exponential decay that yields the localization length, whereas the nonmodular one is overwhelmed by those oscillations and random phase fluctuations, and fails to give a reliable decay law.

2. Equivalence of the MDM and SDM in the noninteracting limit

In this part, we prove that SDM is equal to the basic building block of the MDM in the noninteracting limit. Specifically, when $|GS_N>$ and $|GS_{N-1}\rangle$ are product states and connected by a single-orbital eigenstate $|\psi_{E_F}\rangle$ at the Fermi level as $|GS_N\rangle = |\psi_{E_F}\rangle \otimes |GS_{N-1}\rangle = |\psi_{E_F}\rangle \otimes \prod_{i=1}^{N-1}|\psi_n\rangle$, the following relation is satisfied

$$\langle GS_N|c_i^\dagger c_j|GS_N\rangle - \langle GS_{N-1}|c_i^\dagger c_j|GS_{N-1}\rangle = \langle \psi_{E_F}|c_i^\dagger c_j|\psi_{E_F}\rangle. \tag{C6}$$

We denote nth single-particle eigenstate as $|\psi_n\rangle = \psi_n^\dagger|0\rangle$. Its expansion in the real-space orbital basis reads

$$\psi_n = \sum_i a_{n,i}c_i. \tag{C7}$$

Here, $c_i^\dagger|0\rangle = |i\rangle$ labels the orthonormal real-space orbitals. The amplitudes $a_{n,i}$ form a unitary matrix, such that

$$\sum_i a_{m,i}a_{n,i}^* = \delta_{mn}, \qquad \sum_n a_{n,i}a_{n,j}^* = \delta_{ij}. \tag{C8}$$

Using the unitarity of the coefficients $a_{n,i}$, we invert Eq. (C7) to $c_i^\dagger = \sum_n a_{n,i}\psi_n^\dagger$ and $c_i = \sum_n a_{n,i}^*\psi_n$.

For a noninteracting system, a M-particle ground state is a Slater determinant obtained by occupying M-single-particle eigenstates as $|GS_M\rangle = \prod_{n=1}^M \psi_n^\dagger|0\rangle$. Under this product state, the one-particle density matrix $\rho_{i,j}^{(M)}$ has the following expression

$$\begin{aligned}\rho_{i,j}^{(M)} &\equiv \langle GS_M|c_i^\dagger c_j|GS_M\rangle = \sum_{n,m} a_{n,i}a_{m,j}^*\langle GS_M|\psi_n^\dagger\psi_m|GS_M\rangle \\ &= \sum_{n,m} a_{n,i}a_{m,j}^*\delta_{n,m}n_n^M,\end{aligned} \tag{C9}$$

where $n_n^{(M)} = 1$ if the orbital n is occupied in $|GS_M\rangle$ and $n_n^{(M)} = 0$ if the orbital n is unoccupied. Plugging this into Eq. (C9) yields

$$\rho_{ij}^{(M)} = \sum_n a_{n,i}a_{n,j}^* = \sum_{n=1}^M a_{n,i}a_{n,j}^*. \tag{C10}$$

Hence, the one-particle density matrix element is the sum of projectors $a_{n,i}a_{n,j}^*$ onto all occupied single-particle orbitals. Plugging Eq. (C10) into SDM, one can obtain

$$\begin{aligned}\langle GS_N|c_i^\dagger c_j|GS_N\rangle - \langle GS_{N-1}|c_i^\dagger c_j|GS_{N-1}\rangle &= \rho_{ij}^{(N)} - \rho_{ij}^{(N-1)} \\ &= a_{E_F,i}a_{E_F,j}^* \\ &= \langle \psi_{E_F}|c_i^\dagger c_j|\psi_{E_F}\rangle,\end{aligned} \tag{C11}$$

which completes the proof of Eq. (C6) and demonstrates that, in the noninteracting limit, SDM is equal to the basic building block of MDM.

3. Higher-order terms in SDM for interacting systems

In the main text, we have discussed the relation of SDM to the operator $\hat{\psi}$ connecting $|GS_N\rangle$ and $|GS_{N-1}\rangle$. In this section, we want to have a general discussion on SDM. Here, we focus on the spinful version of SDM without losing generality, defined as

$$\rho^{\mathrm{sub}}_{(i,\alpha);(j,\beta)} = \sum_{\sigma=\uparrow,\downarrow} \left(\langle GS_N|c^\dagger_{i,\alpha,\sigma}c_{j,\beta,\sigma}|GS_N\rangle - \langle GS_{N-1}|c^\dagger_{i,\alpha,\sigma}c_{j,\beta,\sigma}|GS_{N-1}\rangle\right) \tag{C12}$$

where i, j index slices along the longitudinal direction of the quasi-1D bar, and α, β label the site degree of freedom within each slice [see Fig. 1(c)]. The states $|GS_N\rangle$ and $|GS_{N-1}\rangle$ are the many-body ground states with fixed particle numbers N and $N-1$, respectively.

In the special case where $|GS_N\rangle = |\psi_{E_F}\rangle \otimes |GS_{N-1}\rangle$, corresponding to the noninteracting limit, the orthogonality of wave functions leads to the exact relation $\rho^{\mathrm{sub}}_{(i,\alpha);(j,\beta)} = \sum_\sigma \langle\psi_{E_F}|c^\dagger_{i,\alpha,\sigma}c_{j,\beta,\sigma}|\psi_{E_F}\rangle$, which reduces to the same form as the basic building block of MDM in the noninteracting case.

Beyond this simple product-state assumption, we consider the more general case where $|GS_N\rangle$ and $|GS_{N-1}\rangle$ are connected by an operator $\hat{\psi}$ such that $|GS_N\rangle = \hat{\psi}^\dagger|GS_{N-1}\rangle$. In the main text, we have already discussed the case $\hat{\psi}$ that comes from the linear combination of $c_{i\sigma}$. For the Hubbard model or other interacting systems, $\hat{\psi}$ can also contain high-order terms, such as $c_{i,\alpha,\sigma}n_{i,\alpha,\bar{\sigma}}$. Therefore, we consider a more general form of the excitation operator,

$$\hat{\psi} = \sum_{i,\alpha,\sigma} a^{(0)}_{i,\alpha,\sigma}c_{i,\alpha,\sigma} + a^{(1)}_{i,\alpha,\sigma}c_{i,\alpha,\sigma}n_{i,\alpha,\bar{\sigma}} + \cdots = \sum_n \hat{\psi}^{(n)}. \tag{C13}$$

Here, $a^{(0)}_{i,\alpha,\sigma}$ represents the amplitude of a bare fermionic excitation, while $a^{(1)}_{i,\alpha,\sigma}$ captures the contribution of a density-projected excitation involving the opposite spin $\bar{\sigma}$. $\hat{\psi}^{(n)}$ denotes the nth order component of $\hat{\psi}$, e.g., $\hat{\psi}^{(0)} = \sum a^{(0)}_{i,\alpha,\sigma}c_{i,\alpha,\sigma}$ and $\hat{\psi}^{(1)} = \sum a^{(1)}_{i,\alpha,\sigma}c_{i,\alpha,\sigma}n_{i,\alpha,\bar{\sigma}}$. Higher-order terms $\hat{\psi}^{(n)}$ $(n \geq 2)$ may further encode multiparticle correlations in strongly interacting systems.

Based on the expansion of the excitation operator $\hat{\psi}$ introduced above, the SDM can be correspondingly expanded as

$$\rho^{\mathrm{sub}}_{(i,\alpha);(j,\beta)} = \sum_{n,m} \rho^{\mathrm{sub},(n,m)}_{(i,\alpha);(j,\beta)} - \sum_\sigma \langle GS_{N-1}|c^\dagger_{i,\alpha,\sigma}c_{j,\beta,\sigma}|GS_{N-1}\rangle, \tag{C14}$$

where the superscript (n,m) denotes the (n,m)th order contribution associated with the corresponding term in $\hat{\psi}$. Explicitly, the (n,m)-th order component of SDM is given by

$$\rho^{\mathrm{sub},(n,m)}_{(i,\alpha);(j,\beta)} = \sum_\sigma \langle GS_{N-1}|\hat{\psi}^{(n)}c^\dagger_{i,\alpha,\sigma}c_{j,\beta,\sigma}\hat{\psi}^{(m)\dagger}|GS_{N-1}\rangle. \tag{C15}$$

Despite that the operator $\hat{\psi}$ may contain higher-order terms that lead to complicated algebraic relations, we postulate an effective fermion operator ansatz: without specifying the explicit form of higher-order corrections, we assume that the overall operator satisfies the canonical anticommutation relation $\{\hat{\psi}, \hat{\psi}^\dagger\} = 1$. As a consistency check, we evaluate its expectation value in the many-body ground state $|GS_{N-1}\rangle$ as $\langle GS_{N-1}|\{\hat{\psi}, \hat{\psi}^\dagger\}|GS_{N-1}\rangle = \langle GS_N|GS_N\rangle + \langle GS_N|\hat{\psi}^\dagger\hat{\psi}^\dagger\hat{\psi}\,\hat{\psi}\,|GS_N\rangle = 1 + 0 = 0$, which suggests that the effective normalization is approximately preserved within the low-energy subspace relevant for our construction. This provides a tentative theoretical justification for employing $\hat{\psi}$ as an effective fermionic excitation operator in the interacting case.

Using the anticommutation relation of $\hat{\psi}$, Eq. (C14) can be rewritten as

$$\begin{aligned}
\rho^{\mathrm{sub}}_{(i,\alpha);(j,\beta)} &= \sum_{n,m}\langle(\{\hat{\psi}^{(n)}, c^\dagger_{i,\alpha,\sigma}\} - c^\dagger_{i,\alpha,\sigma}\hat{\psi}^{(n)})(\{c_{j,\beta,\sigma}, \hat{\psi}^{(m)\dagger}\} - \hat{\psi}^{(m)\dagger}c_{j,\beta,\sigma})\rangle_{N-1} - \langle c^\dagger_{i,\alpha,\sigma}c_{j,\beta,\sigma}\rangle_{N-1} \\
&= \sum_{n,m}\sum_\sigma(\langle\{\hat{\psi}^{(n)}, c^\dagger_{i,\alpha,\sigma}\}\{c_{j,\beta,\sigma}, \hat{\psi}^{(m)\dagger}\}\rangle_{N-1} - \langle\{\hat{\psi}^{(n)}, c^\dagger_{i,\alpha,\sigma}\}\hat{\psi}^{(m)\dagger}c_{j,\beta,\sigma}\rangle_{N-1} - \langle c^\dagger_{i,\alpha,\sigma}\hat{\psi}^{(n)}\{c_{j,\beta,\sigma}, \hat{\psi}^{(m)\dagger}\}\rangle_{N-1}) \\
&\quad + \sum_\sigma\langle c^\dagger_{i,\alpha,\sigma}(\hat{\psi}\hat{\psi}^\dagger - 1)c_{j,\beta,\sigma}\rangle_{N-1} \\
&= \sum_{n,m}\sum_\sigma(\langle\{\hat{\psi}^{(n)}, c^\dagger_{i,\alpha,\sigma}\}\{c_{j,\beta,\sigma}, \hat{\psi}^{(m)\dagger}\}\rangle_{N-1} - \langle\{\hat{\psi}^{(n)}, c^\dagger_{i,\alpha,\sigma}\}\hat{\psi}^{(m)\dagger}c_{j,\beta,\sigma}\rangle_{N-1} - \langle c^\dagger_{i,\alpha,\sigma}\hat{\psi}^{(n)}\{c_{j,\beta,\sigma}, \hat{\psi}^{(m)\dagger}\}\rangle_{N-1}) \\
&\quad + \sum_\sigma\langle c^\dagger_{i,\alpha,\sigma}\hat{\psi}^\dagger\hat{\psi}c_{j,\beta,\sigma}\rangle_{N-1} \\
&\equiv \sum_{n,m}\chi^{\mathrm{sub},(n,m)}_{(i,\alpha);(j,\beta)} + \sum_\sigma\langle c^\dagger_{i,\alpha,\sigma}\hat{\psi}^\dagger\hat{\psi}c_{j,\beta,\sigma}\rangle_{N-1}.
\end{aligned} \tag{C16}$$

Here, we use $\chi^{\mathrm{sub},(n,m)}_{(i,\alpha);(j,\beta)}$ to denote above long expressions, and $\langle\cdots\rangle_{N-1}$ is the simplified notation of $\langle GS_{N-1}|\cdots|GS_{N-1}\rangle$. Despite the complexity of these expression, we can further simplify it as follows:

(i) First, for the case $n=m=0$, corresponding to the contribution of the bare fermionic excitation operator to the SDM, according to the anticommutation relations of $\hat{\psi}^{(0)}$ as follow

$$\{\hat{\psi}^{(0)}, c^{\dagger}_{i,\alpha,\sigma}\} = a^{(0)}_{i,\alpha,\sigma} \quad \{\hat{\psi}^{(0)\dagger}, c_{j,\beta,\sigma}\} = a^{(0)*}_{j,\beta,\sigma} \tag{C17}$$

one can obtain

$$\chi^{\mathrm{sub},(0,0)}_{(i,\alpha);(j,\beta)} = \sum_{\sigma}(a^{(0)}_{i,\alpha,\sigma}a^{(0)}_{j,\beta,\sigma} - a^{(0)}_{i,\alpha,\sigma}\langle\hat{\psi}^{(0)\dagger}c_{j,\beta,\sigma}\rangle_{N-1} - a^{(0)*}_{j,\beta,\sigma}\langle c^{\dagger}_{i,\alpha,\sigma}\hat{\psi}^{(0)}\rangle_{N-1}). \tag{C18}$$

Here, $\sum_{\sigma} a^{(0)}_{i,\alpha,\sigma}a^{(0)}_{j,\beta,\sigma} = \sum_{\sigma}\langle\psi^{(0)}|c^{\dagger}_{i,\alpha,\sigma}c_{j,\beta,\sigma}|\psi^{(0)}\rangle$ encode the localization properties of $\hat{\psi}^{(0)}$, which follows the same expression as in Eq. (9) in the main text, with the additional spin summation in the spinful system.

(ii) Second, for the case $n=0$, $m=1$ and $n=1$, $m=0$, corresponding to the cross terms arising from the bare fermionic excitation operator and the 1st order density-projected fermionic excitation operator, according to the anticommutation relation of $\hat{\psi}^{(0)}$ in Eq. (C17) and $\hat{\psi}^{(1)}$ as follow

$$\{\hat{\psi}^{(1)}, c^{\dagger}_{i,\alpha,\sigma}\} = a^{(1)}_{i,\alpha,\sigma}n_{i,\alpha,\bar{\sigma}} - a^{(1)}_{i,\alpha,\bar{\sigma}}S^{\sigma,\bar{\sigma}}_{i,\alpha}, \tag{C19}$$

$$\{\hat{\psi}^{(1)\dagger}, c_{j,\beta,\sigma}\} = a^{(1)}_{j,\beta,\sigma}n_{j,\beta,\bar{\sigma}} - a^{(1)}_{j,\beta,\bar{\sigma}}S^{\bar{\sigma},\sigma}_{j,\beta}, \tag{C20}$$

one can obtain

$$\chi^{\mathrm{sub},(0,1)}_{(i,\alpha);(j,\beta)} = \sum_{\sigma}(a^{(0)}_{i,\alpha,\sigma}a^{(1)}_{j,\beta,\sigma}\langle n_{j,\beta,\bar{\sigma}}\rangle_{N-1} - a^{(0)}_{i,\alpha,\sigma}\langle\hat{\psi}^{(1)\dagger}c_{j,\beta,\sigma}\rangle_{N-1} - a^{(1)*}_{j,\beta,\sigma}\langle c^{\dagger}_{i,\alpha,\sigma}\hat{\psi}^{(0)}n_{j,\beta,\bar{\sigma}}\rangle_{N-1} + a^{(1)*}_{j,\beta,\bar{\sigma}}\langle c^{\dagger}_{i,\alpha,\sigma}\hat{\psi}^{(0)}S^{\bar{\sigma},\sigma}_{j,\beta}\rangle_{N-1}). \tag{C21}$$

$$\chi^{\mathrm{sub},(1,0)}_{(i,\alpha);(j,\beta)} = \sum_{\sigma}(a^{(1)}_{i,\alpha,\sigma}a^{(0)}_{j,\beta,\sigma}\langle n_{i,\alpha,\bar{\sigma}}\rangle_{N-1} - a^{(0)*}_{j,\beta,\sigma}\langle c^{\dagger}_{i,\alpha,\sigma}\hat{\psi}^{(1)}\rangle_{N-1} - a^{(1)}_{i,\alpha,\sigma}\langle n_{i,\alpha,\bar{\sigma}}\psi^{(0)\dagger}c_{j,\beta,\sigma}\rangle_{N-1} + a^{(1)}_{i,\alpha,\bar{\sigma}}\langle S^{\sigma,\bar{\sigma}}_{i,\alpha}\hat{\psi}^{(0)\dagger}c_{j,\beta,\sigma}\rangle_{N-1}). \tag{C22}$$

Here, we use the notation $S^{\sigma,\bar{\sigma}}_{i,\alpha} \equiv c^{\dagger}_{i,\alpha,\sigma}c_{i,\beta,\bar{\sigma}}$, so that $S^{\uparrow,\downarrow}_{i,\alpha} = S^{\dagger}_{i,\alpha}$ is the spin creation operator and $S^{\downarrow,\uparrow}_{i,\alpha} = S_{i,\alpha}$ is the spin annihilation operator at (i,α). The relations in Eq. (C21) and Eq. (C22) hold by invoking the total spin conservation of the ground state $|GS_{N-1}\rangle$, so that $\langle S^{\sigma,\bar{\sigma}}_{i,\alpha}\rangle_{N-1} = \langle S^{\bar{\sigma},\sigma}_{j,\beta}\rangle_{N-1} = 0$. Moreover, since we have the relation $\sum_n \hat{\psi}^{(n)}|GS_{N-1}\rangle = \hat{\psi}|GS_{N-1}\rangle = \hat{\psi}\,\hat{\psi}\,|GS_N\rangle = 0$, the last two terms in Eq. (C18) and the second term in Eq. (C21) and Eq. (C22) can be neglected as a whole when summed over $\chi^{\mathrm{sub},(n,m)}_{(i,\alpha);(j,\beta)}$ for all n and m.

(iii) Third, for the case $n=m=1$, corresponding to the contribution of the 1st order density-projected fermionic excitation operator to the SDM, according to the anticommutation relations in Eq. (C19) and Eq. (C20), one can obtain

$$\begin{aligned}\chi^{\mathrm{sub},(1,1)}_{(i,\alpha);(j,\beta)} = \sum_{\sigma}[&a^{(1)}_{i,\alpha,\sigma}a^{(1)}_{j,\beta,\sigma}\langle n_{i,\alpha,\bar{\sigma}}n_{j,\beta,\bar{\sigma}}\rangle_{N-1} - a^{(1)}_{i,\alpha,\sigma}a^{(1)}_{j,\beta,\bar{\sigma}}\langle n_{i,\alpha,\bar{\sigma}}S^{\bar{\sigma},\sigma}_{j,\beta}\rangle_{N-1} - a^{(1)}_{i,\alpha,\bar{\sigma}}a^{(1)}_{j,\beta,\sigma}\langle S^{\sigma,\bar{\sigma}}_{i,\alpha}n_{j,\beta,\bar{\sigma}}\rangle_{N-1}\\ &+ a^{(1)}_{i,\alpha,\bar{\sigma}}a^{(1)}_{j,\beta,\bar{\sigma}}\langle S^{\sigma,\bar{\sigma}}_{i,\alpha}S^{\bar{\sigma},\sigma}_{j,\beta}\rangle_{N-1} - a^{(1)}_{i,\alpha,\sigma}\langle n_{i,\alpha,\bar{\sigma}}\hat{\psi}^{(1)\dagger}c_{j,\beta,\sigma}\rangle_{N-1} + a^{(1)}_{i,\alpha,\bar{\sigma}}\langle S^{\sigma,\bar{\sigma}}_{i,\alpha}\hat{\psi}^{(1)\dagger}c_{j,\beta,\sigma}\rangle_{N-1}\\ &- a^{(1)}_{j,\beta,\sigma}\langle c^{\dagger}_{i,\alpha,\sigma}\hat{\psi}^{(1)}n_{j,\beta,\bar{\sigma}}\rangle_{N-1} + a^{(1)}_{j,\beta,\bar{\sigma}}\langle c^{\dagger}_{i,\alpha,\sigma}\hat{\psi}^{(1)}S^{\bar{\sigma},\sigma}_{j,\beta}\rangle_{N-1}].\end{aligned} \tag{C23}$$

This expression can be further simplified by invoking the total spin-number conservation condition of $|GS_{N-1}>$ such that $\langle n_{i,\alpha,\bar{\sigma}}S^{\bar{\sigma},\sigma}_{j,\beta}\rangle_{N-1} = \langle S^{\sigma,\bar{\sigma}}_{i,\alpha}n_{j,\beta,\bar{\sigma}}\rangle_{N-1} = 0$.

Taking all above equalities into consideration, one can obtain the overall form of $\rho^{\mathrm{sub}}_{(i,\alpha);(j,\beta)}$ as follow

$$\begin{aligned}\rho^{\mathrm{sub}}_{(i,\alpha);(j,\beta)} = \sum_{\sigma}[&a^{(0)}_{i,\alpha,\sigma}a^{(0)}_{j,\beta,\sigma} + a^{(0)}_{i,\alpha,\sigma}a^{(1)}_{j,\beta,\sigma}\langle n_{j,\beta,\bar{\sigma}}\rangle_{N-1} + a^{(1)}_{i,\alpha,\sigma}a^{(0)}_{j,\beta,\sigma}\langle n_{i,\alpha,\bar{\sigma}}\rangle_{N-1} + a^{(1)}_{i,\alpha,\sigma}a^{(1)}_{j,\beta,\sigma}\langle n_{i,\alpha,\bar{\sigma}}n_{j,\beta,\bar{\sigma}}\rangle_{N-1}\\ &+ a^{(1)}_{i,\alpha,\bar{\sigma}}a^{(1)}_{j,\beta,\bar{\sigma}}\langle S^{\sigma,\bar{\sigma}}_{i,\alpha}S^{\bar{\sigma},\sigma}_{j,\beta}\rangle_{N-1} + a^{(1)}_{i,\alpha,\bar{\sigma}}\langle S^{\sigma,\bar{\sigma}}_{i,\alpha}\hat{\psi}^{\dagger}c_{j,\beta,\sigma}\rangle_{N-1} + a^{(1)}_{j,\beta,\bar{\sigma}}\langle c^{\dagger}_{i,\alpha,\sigma}\hat{\psi}S^{\bar{\sigma},\sigma}_{j,\beta}\rangle_{N-1}\\ &- a^{(1)}_{i,\alpha,\sigma}\langle n_{i,\alpha,\bar{\sigma}}\hat{\psi}^{\dagger}c_{j,\beta,\sigma}\rangle_{N-1} - a^{(1)}_{j,\beta,\sigma}\langle c^{\dagger}_{i,\alpha,\sigma}\hat{\psi}n_{j,\beta,\bar{\sigma}}\rangle_{N-1} + \langle c^{\dagger}_{i,\alpha,\sigma}\hat{\psi}^{\dagger}\hat{\psi}c_{j,\beta,\sigma}\rangle_{N-1} + \cdots].\end{aligned} \tag{C24}$$

The second and third lines of this expression can be further expanded order by order and simplified using the following commutation relations:

$$[\hat{\psi}, n_{j,\beta,\bar{\sigma}}] = a^{(0)}_{j,\beta,\bar{\sigma}}c_{j,\beta,\bar{\sigma}} + a^{(1)}_{j,\beta,\bar{\sigma}}c_{j,\beta,\bar{\sigma}}n_{j,\beta,\sigma} + \cdots \tag{C25}$$

$$[n_{i,\alpha,\bar{\sigma}}, \hat{\psi}^{\dagger}] = a^{(0)*}_{i,\alpha,\bar{\sigma}}c^{\dagger}_{i,\alpha,\bar{\sigma}} + a^{(1)*}_{i,\alpha,\bar{\sigma}}c^{\dagger}_{i,\alpha,\bar{\sigma}}n_{i,\alpha,\sigma} + \cdots \tag{C26}$$

$$[\hat{\psi}, S^{\bar{\sigma},\sigma}_{j,\beta}] = a^{(0)}_{j,\beta,\bar{\sigma}}c_{j,\beta,\sigma} + a^{(1)}_{j,\beta,\bar{\sigma}}c_{j,\beta,\sigma}n_{j,\beta,\bar{\sigma}} + \cdots \tag{C27}$$

$$[S^{\sigma,\bar{\sigma}}_{i,\alpha}, \hat{\psi}^{\dagger}] = a^{(0)*}_{i,\alpha,\bar{\sigma}}c^{\dagger}_{i,\alpha,\sigma} + a^{(1)*}_{i,\alpha,\bar{\sigma}}c^{\dagger}_{i,\alpha,\sigma}n_{i,\alpha,\bar{\sigma}} + \cdots \tag{C28}$$

$$\{\hat{\psi}, c_{j,\beta,\sigma}\} = -a^{(1)}_{j,\beta,\bar{\sigma}}c_{j,\beta,\bar{\sigma}}c_{j,\beta,\sigma} + \cdots \tag{C29}$$

$$\{c^{\dagger}_{i,\alpha,\sigma}, \hat{\psi}^{\dagger}\} = -a^{(1)*}_{i,\alpha,\bar{\sigma}}c^{\dagger}_{i,\alpha,\sigma}c^{\dagger}_{i,\alpha,\bar{\sigma}} + \cdots \tag{C30}$$

Combining this with the fact that $\hat{\psi}|GS_{N-1}\rangle = \hat{\psi}\,\hat{\psi}\,|GS_N\rangle = 0$ and the total spin quantum number conservation, Eq. (C24) can be rewritten in its final, order-by-order simplified form as

$$\begin{aligned}\rho^{\mathrm{sub}}_{(i,\alpha);(j,\beta)} = \sum_{\sigma}[&a^{(0)}_{i,\alpha,\sigma}a^{(0)}_{j,\beta,\sigma} + a^{(0)}_{i,\alpha,\sigma}a^{(1)}_{j,\beta,\sigma}\langle n_{j,\beta,\bar{\sigma}}\rangle_{N-1} + a^{(1)}_{i,\alpha,\sigma}a^{(0)}_{j,\beta,\sigma}\langle n_{i,\alpha,\bar{\sigma}}\rangle_{N-1} + a^{(1)}_{i,\alpha,\sigma}a^{(1)}_{j,\beta,\sigma}\langle n_{i,\alpha,\bar{\sigma}}n_{j,\beta,\bar{\sigma}}\rangle_{N-1}\\ &+ a^{(1)}_{i,\alpha,\bar{\sigma}}a^{(1)}_{j,\beta,\bar{\sigma}}\langle S^{\sigma,\bar{\sigma}}_{i,\alpha}S^{\bar{\sigma},\sigma}_{j,\beta}\rangle_{N-1} + (a^{(1)}_{i,\alpha,\bar{\sigma}}a^{(0)*}_{i,\alpha,\bar{\sigma}} + a^{(1)}_{j,\beta,\bar{\sigma}}a^{(0)*}_{j,\beta,\bar{\sigma}})\langle c^{\dagger}_{i,\alpha,\sigma}c_{j,\beta,\sigma}\rangle_{N-1} + |a^{(1)}_{i,\alpha,\bar{\sigma}}|^2\langle c^{\dagger}_{i,\alpha,\sigma}n_{i,\alpha,\bar{\sigma}}c_{j,\beta,\sigma}\rangle_{N-1}\\ &+ |a^{(1)}_{j,\beta,\bar{\sigma}}|^2\langle c^{\dagger}_{i,\alpha,\sigma}n_{j,\beta,\bar{\sigma}}c_{j,\beta,\sigma}\rangle_{N-1} + a^{(1)*}_{i,\alpha,\bar{\sigma}}a^{(1)*}_{j,\beta,\bar{\sigma}}\langle c^{\dagger}_{i,\alpha,\sigma}c^{\dagger}_{i,\alpha,\bar{\sigma}}c_{j,\beta,\bar{\sigma}}c_{j,\beta,\sigma}\rangle_{N-1} + \cdots]\end{aligned} \tag{C31}$$

In summary, the zeroth-order contribution $\rho^{\mathrm{sub},(0)}$ corresponds directly to the MDM of the bare single-particle excitation $\psi^{(0)}$, fully consistent with the spinless case. Nevertheless, additional corrections arise from the projected fermionic excitation $\psi^{(1)}$, involving density average $\langle n_{i,\alpha,\bar{\sigma}}\rangle_{N-1}$, density-density correlators $\langle n_{i,\alpha,\bar{\sigma}}n_{j,\beta,\bar{\sigma}}\rangle_{N-1}$ and spin-spin correlators $\langle S^{\sigma,\bar{\sigma}}_{i,\alpha}S^{\bar{\sigma},\sigma}_{j,\beta}\rangle_{N-1}$. We expect density-density and spin-spin correlations in systems without magnetic or charge order to decay rapidly with oscillations and thus be strongly suppressed at large separations x, while the density average contributes a subleading, exponentially decaying modification $(a^{(0)}_{i,\alpha,\sigma}a^{(1)}_{j,\beta,\sigma}\langle n_{j,\beta,\bar{\sigma}}\rangle_{N-1} + a^{(1)}_{i,\alpha,\sigma}a^{(0)}_{j,\beta,\sigma}\langle n_{i,\alpha,\bar{\sigma}}\rangle_{N-1})$ at finite x. For the terms in the second and third lines, involving the structures of single-particle correlators $\langle c^{\dagger}_{i,\alpha,\sigma}c_{j,\beta,\sigma}\rangle_{N-1}$, density-projected single-particle correlators $\langle c^{\dagger}_{i,\alpha,\sigma}n_{i,\alpha,\bar{\sigma}}c_{j,\beta,\sigma}\rangle_{N-1}$ and pair-pair correlators $\langle c^{\dagger}_{i,\alpha,\sigma}c^{\dagger}_{i,\alpha,\bar{\sigma}}c_{j,\beta,\bar{\sigma}}c_{j,\beta,\sigma}\rangle_{N-1}$. We argue that these contributions are small: for weak interactions (small U), the coefficients $|a^{(1)}_{i,\alpha,\sigma}|$ are negligible, while for strong interactions (large U) the double occupancy is strongly suppressed. Combining with the fact that single-particle correlators and pair-pair correlators also decay rapidly with oscillatory behavior, the expectation values of the terms in the second and third lines are driven toward zero. Taken together, we expect that $\rho^{\mathrm{sub},(0)}$ still provides the main contribution to the SDM, retaining its clean exponential decay even at finite interaction U in the Anderson–Hubbard model, as shown in Figs. 7(b) and 23. In more general situations, we cannot prove this feature is always true. However, as we discussed in the main text, we expect the ground states to be always localized for finite-size quasi-1D systems at finite disorder strength except in special cases. If there exists one $\hat{\psi}$, SDM still provides important information about $\hat{\psi}$.

APPENDIX D: MODIFIED SPINLESS INTERACTING MODEL FOR A 2D METALLIC STATE

In order to further elucidate the interaction-induced delocalization mechanism and to provide additional evidence for the existence of a 2D correlated metallic phase, we construct a modified spinless interacting model with selected nearest-neighbor bonds. This model significantly reduces the computational complexity while capturing the essential delocalization physics of the Anderson-Hubbard model. Owing to its numerical tractability, we are able to perform finite-size scaling analyses with quasi-1D widths from $M = 2$ to $M = 5$. At finite interaction strengths $V = 2.5t$ and filling $n = 5/15$, we obtain a clear metallic scaling behavior, which further supports our expectation that the competition between electron-electron interactions and disorder can stabilize a two-dimensional metallic phase.

1. Reason for interaction-induced delocalization

Before introducing the modified spinless interacting model, we want to provide the delocalization reason of the Hubbard interaction U in the Anderson-Hubbard model [Eq. (13)], as schematically illustrated in Fig. 15(a). Specifically, in the noninteracting limit $U = 0$, the disorder potential is spin independent $\epsilon_{i,\uparrow} = \epsilon_{i,\downarrow} = \epsilon_i$, so that both spin species share the same disorder landscape and a disorder-selected low-energy site (site i in Fig. 15) is doubly occupied by two particles with opposite spins. However, as the Hubbard interaction U is turned on, double occupancy at one site becomes energetically costly due to the term $Un_{i\uparrow}n_{i\downarrow}$, which forces the two electrons to separate spatially. This interaction-induced suppression of simultaneous double occupancy at disorder-selected sites weakens the effective localization effect by disorder and produces a delocalizing tendency compared to the noninteracting case.

To emulate the delocalization mechanism of the Anderson-Hubbard model in a numerically tractable setting, we introduce a modified spinless interacting model with selected bonds. The delocalization mechanism originates from these selected bonds, as schematically illustrated in Fig. 15(b). In this construction, we select a set of mutually independent nearest-neighbor bonds, each consisting of two adjacent sites, and the index i in Fig. 15(b) labels the bond rather than site. The two adjacent sites (labeled as 1,2) within each bond correspond to the two spin degrees of freedom at each site in the Anderson-Hubbard model. In analogy with the Anderson-Hubbard model, the two adjacent sites within each bond share the same disorder potential ϵ_i, and the nearest-neighbor repulsive interaction V appears only between the two adjacent sites belonging to the same bond, which reads $Vn_{i1}n_{i2}$. In the noninteracting limit ($V = 0$), two spinless electrons tend to be localized in the same bond, which leads to the double occupancy at the disorder-selected low-energy bonds. However, A finite nearest-neighbor repulsion V within each bond penalizes such double occupancy, thereby enforcing spatial separation of electrons and generating a direct competition between interaction and disorder. Therefore, this modified spinless interacting model with selected bonds captures the same delocalization mechanism as that in the Anderson-Hubbard model.

2. Model construction and finite-size scaling results

Based on the above discussion of the interaction-disorder competition and the associated delocalization mechanism, we now introduce in detail the modified spinless interacting model with selected bonds and present the corresponding finite-size scaling results. The Hamiltonian of the modified spinless interacting model is given by

$$H = -t \sum_{\langle (i,a);(j,b)\rangle} c^{\dagger}_{i,a} c_{j,b} + \sum_{i\in\mathcal{B}} \epsilon_i (n_{i,1} + n_{i,2}) + V \sum_{i\in\mathcal{B}} n_{i,1} n_{i,2}. \tag{D1}$$

Here, the indices i, j label the nearest-neighbor bonds, and $a, b \in \{1, 2\}$ label the two adjacent sites within each bond. Each index tuple (i, a) corresponds to a lattice site in the

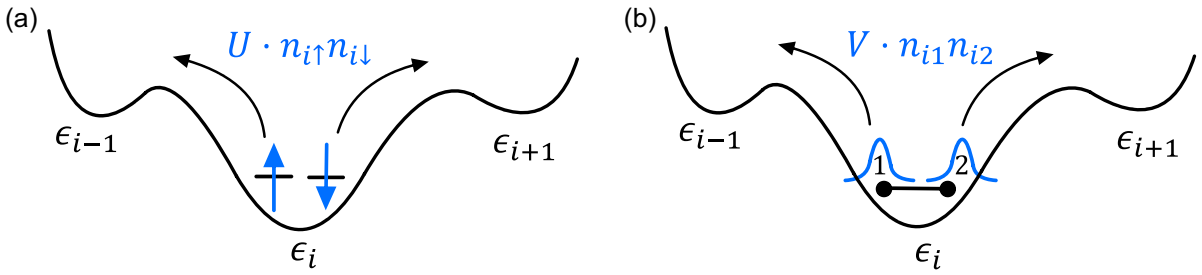

FIG. 15. Schematic diagrams of the interaction-disorder competition mechanism in (a) the Anderson-Hubbard model and (b) the modified spinless model with selected bonds. The indices $i - 1$, i and $i + 1$ in (a) or (b) label the sites or bonds with local random potentials ϵ_{i-1}, ϵ_i, and ϵ_{i+1}. Different spins on a site in (a) and different sites within a bond in (b) share the same random potential. In (a), the on-site Hubbard interaction $Un_{i\uparrow}n_{i\downarrow}$ (blue) penalizes the double occupancy with different spins at site i, thereby promoting a delocalizing tendency. In (b), the interaction acts only within a selected nearest-neighbor bond connecting sites 1 and 2 via $Vn_{i1}n_{i2}$ (blue) to penalize the double occupancy in a bond, providing a similar interaction-induced delocalizing tendency that competes with disorder.

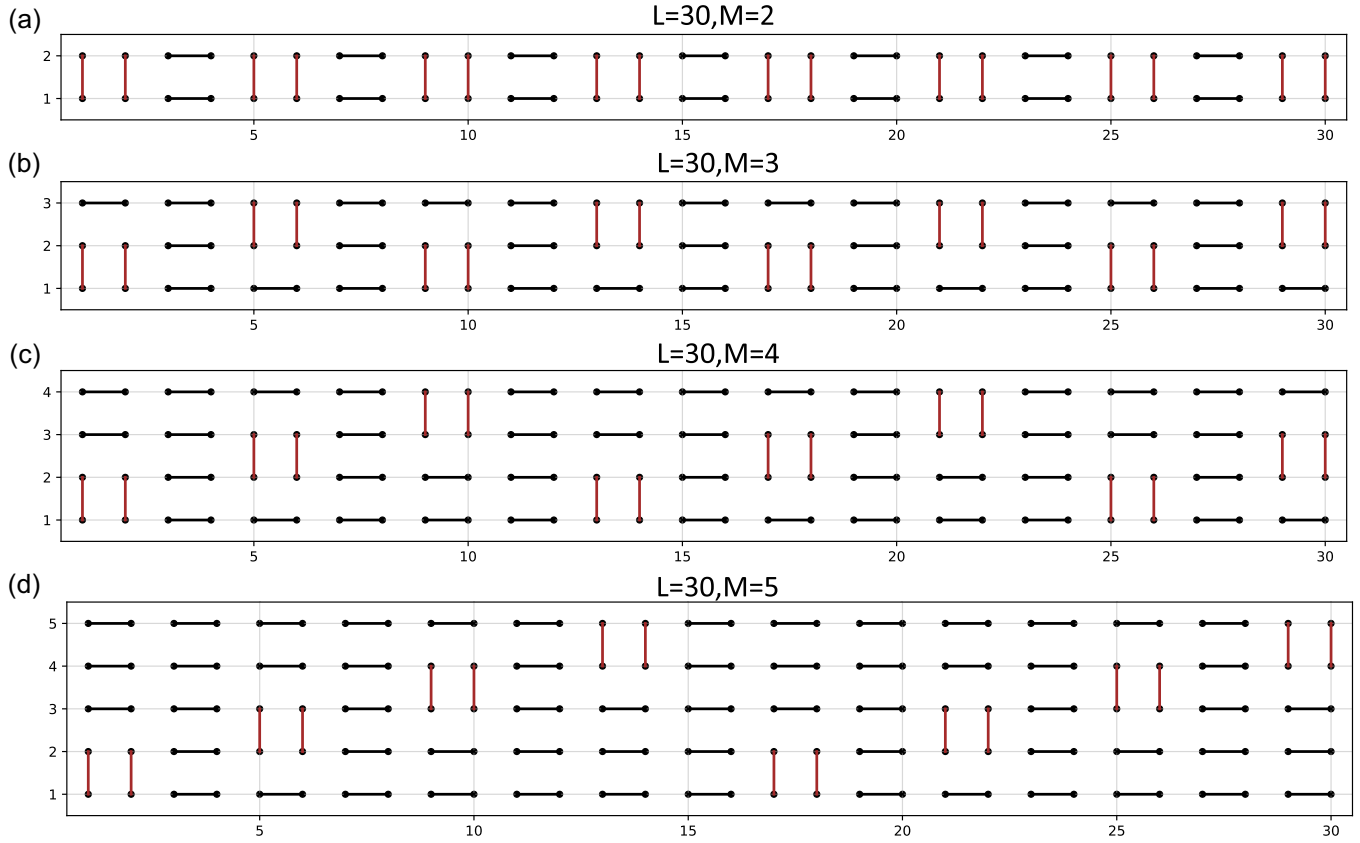

FIG. 16. Bond configurations of the modified spinless interacting model used in our quasi-1D calculations for longitudinal length $L = 30$ and transverse widths (a) $M = 2$, (b) $M = 3$, (c) $M = 4$, and (d) $M = 5$, with open boundary conditions. The longitudinal bonds (black solid lines) and transverse bonds (brown solid lines) connect nearest-neighbor sites. The hopping term t acts between all nearest-neighbor sites, while the repulsive interaction V acts only within each bond (i.e., between the two sites connected by the same solid segment). In addition, each two sites within a bond share the same random on-site potential.

quasi-1D geometry, and $\mathcal{B}$ denotes the set of all selected bonds. The bond configurations of the quasi-1D systems with different widths are shown in Fig. 16, and will be discussed in detail later. In this model, hopping terms t exist between all nearest-neighbor sites, while the nearest-neighbor repulsive interaction V acts only between the two nearest-neighbor sites belonging to the same bond. And the two sites within each bond share the same random potential ϵ_i, where ϵ_i satisfies a binary distribution taking values $\{-W, W\}$ with equal probability in our calculations.

We consider quasi-1D systems of size $M \times L$, with a fixed longitudinal length $L = 30$ and transverse widths $M = 2$–5. The bond configurations for different widths are shown in Figs. 16(a)–16(d). In these constructions, the majority of the bonds are oriented along the longitudinal direction, with a small number of transverse bonds regularly interspersed.

The inclusion of transverse bonds is motivated by finite-size considerations. Because of computational constraints, the longitudinal length is limited to $L = 30$, and we aim to extract localization lengths that remain well below $L/2$ in order to avoid finite-size effects. Compared to longitudinal bonds, transverse bonds generate a weaker delocalizing effect along the longitudinal direction, thereby preventing the localization length from becoming excessively large. Therefore, introducing a small number of transverse bonds allows us to control the magnitude of the localization length while preserving the essential interaction-disorder competition encoded in the bond construction. This choice enables a transverse finite-size scaling analysis that is essentially unaffected by finite-size effects along the longitudinal direction.

In this modified spinless interacting model, we consider an electron filling $n = 5/15$ which is away from half-filling to avoid other competing orders. We first examine the noninteracting case with $V = 0$. Using the MDM framework, we extract the decaying modes $\gamma(x)$ for each disorder strength W and quasi-1D width M. Within the considered disorder range $W \in [1.8t, 2.0t]$, $\gamma(x)$ all exhibit robust exponential decay as $\gamma(x) \sim e^{-x/\xi_M}$, as shown in Fig. 17(a) for the representative results at disorder strength $W = 1.9t$. The corresponding finite-size scaling analysis of ξ_M/M is shown in Fig. 17(c), which reveal a clear localized scaling behavior. Specifically, for a fixed width M, ξ_M/M decreases as W increases; and for a fixed disorder strength W, ξ_M/M decreases with increasing M, confirming the absence of metallic scaling in the noninteracting case.

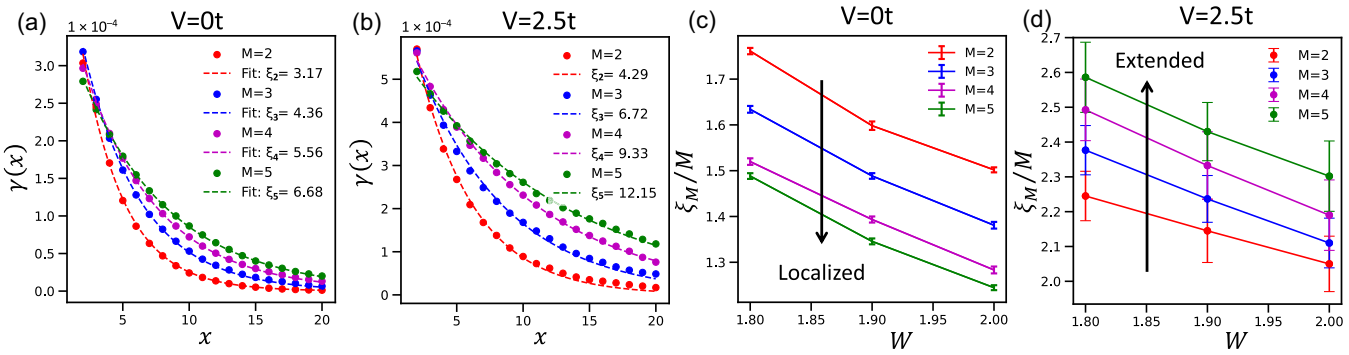

FIG. 17. Results of $\gamma(x)$ and finite-size scaling of ξ_M/M for the quasi-1D modified spinless interacting model with selected bonds. (a) The $\gamma(x)$ and exponential fitting results for $M = 2, 3, 4, 5$ in the noninteracting case with $V = 0$ and $W = 1.9t$, which is calculated by ED. (c) The corresponding finite-size scaling of ξ_M/M for $W = 1.8t$–$2.0t$. (b) The $\gamma(x)$ and exponential fitting results for $M = 2, 3, 4, 5$ with $V = 2.5t$ and $W = 1.9t$, which is calculated by DMRG; (d) is the corresponding finite-size scaling of ξ_M/M for $W1.8t$–$2.0t$. All disorder realizations are on systems of size $M \times L$ with $L = 30$ under OBC and at filling $n = 5/15$, and the bond configurations are shown in Fig. 16. In the site averaging for each sample, the 3 sites nearest to each boundary are excluded to minimize open-boundary effects. In (c), data points are disorder averages over 5 independent batches of 2000 disorder realizations, and error bars are the standard errors of the mean across the 5 batch-averaged values. In (d), each point is averaged over 200 realizations, and error bars are standard errors of the mean obtained from 10 subsets of 20 samples.

We then move on to the interacting case with $V = 2.5t$. Using the SDM framework, we extract the decaying modes for each disorder strength W and quasi-1D width M through DMRG calculation. Further computational details and single-sample benchmarks with ED in the noninteracting case ($V = 0$) are presented in Appendix E 1. The representative results of $\gamma(x)$ at disorder strength $W = 1.9t$ are shown in Fig. 17(b), which retain robust exponential decaying even in the presence of strong repulsive interaction $V = 2.5t$. Additional numerical results of $\gamma(x)$ and the corresponding exponential fits at other disorder strengths can be found in Appendix E 3. Moreover, comparing Fig. 17(b) with Fig. 17(a), we found that the localization length ξ_M at $V = 2.5t$ are all significantly larger than that at $V = 0t$, with the enhancement becoming more pronounced as M increases. For example, we have $\xi_2(V = 2.5t)/\xi_2(V = 2.5t) \approx 1.35$, $\xi_3(V = 2.5t)/\xi_3(V = 0t) \approx 1.54$, $\xi_4(V = 2.5t)/\xi_4(V = 0t) \approx 1.68$, and $\xi_5(V = 2.5t)/\xi_5(V = 0t) \approx 1.82$ at disorder strength $W = 1.9t$. This directly impacts the finite-size scaling of ξ_M/M in Fig. 17(d), where ξ_M still decreases with increasing W for a fixed quasi-1D width M; but for a fixed W, ξ_M now increases with system width M. Such scaling behavior reveals a 2D metallic phase.

All above interaction-induced delocalization effects and finite-size scaling analysis in the modified spinless interacting model are fully consistent with that in the Anderson-Hubbard model discussed in the main text. Both models supports that the essential competition between electron-electron interactions and disorder leads to a delocalization effect. Taken together, these results provide strong evidence that interaction-disorder competition can give rise to a metallic phase in two dimensions.

APPENDIX E: DETAILS OF DMRG CALCULATIONS FOR INTERACTING SYSTEMS

In this section we provide additional details regarding the numerical implementation of our method in interacting disordered systems. We first describe the DMRG parameters used in the calculations of the spinless 1D interacting model [Eq. (11)] and the Anderson-Hubbard model [Eq. (13)] in quasi-1D system with width $M = 2, 3$, together with benchmark comparisons to ED at $V = 0$ ($U = 0$) for randomly selected disorder samples. We also present supplementary results for the quasi-1D Anderson–Hubbard model, including $\gamma(x)$ obtained at different disorder strengths W and interaction strengths U. These results complement the discussion in the main text and further confirm the accuracy and robustness of the many-body MDM approach.

1. DMRG parameters and benchmarks

In this work, numerical calculations for interacting systems are performed using the DMRG method [52], as implemented in the ITENSOR package [102,103]. We first describe the DMRG setup used for the spinless 1D interacting model with on-site disorder. In our calculation, we consider the systems of size $L = 120$ at half-filling in the spinless case. We exploited particle-number conservation, restricting the system to particle numbers $N = 60$ and $N = 59$ in order to compute the two corresponding ground states $|GS_N\rangle$ and $|GS_{N-1}\rangle$. The number of kept states is sequentially increased following the array [30, 50, 100, 200, 400], in combination with finite-lattice sweeps given by [80, 80, 80, 80, 10]. From the two ground states obtained in this way, the SDM is evaluated following Eq. (7), and the interacting version of the MDM is then constructed

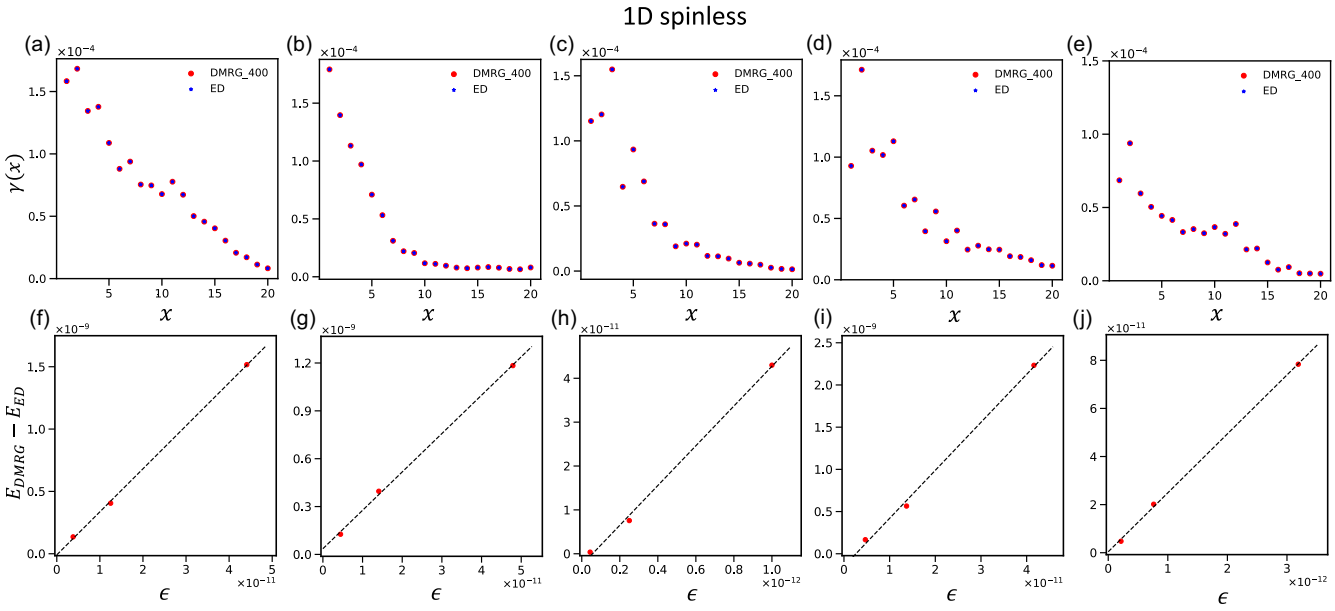

FIG. 18. Benchmarks results between DMRG and ED for the spinless 1D model with on-site disorder [Eq. (11)] of size $L = 120$ at $U = 0$, $W = 2t$ and half-filling under OBC. (a)–(e) $\gamma(x)$ as a function of x for five randomly chosen disorder samples. Red dots are DMRG results with the number of kept states gradually increased up to 400, while blue dots are ED results. (f)–(j) The scaling of the ground-state energy difference $E_{\mathrm{DMRG}} - E_{\mathrm{ED}}$ for $|GS_N\rangle$ with truncation error ϵ for the corresponding samples. When performing the site average, the 20 sites closest to each boundary are excluded to minimize open-boundary effects.

according to Eq. (10). After symmetrization, the slowest-decaying mode $\gamma(x)$ is extracted from the MDM.

In the case of $V = 0$, the MDM obtained from DMRG agrees extremely well with that from ED of the noninteracting Hamiltonian. To benchmark the DMRG results against ED at the single-sample level, the SDM is averaged over lattice sites only, without averaging over disorder realizations. Five disorder realizations are randomly chosen for comparison. Figures 18(a)–18(e) display $\gamma(x)$ obtained from both DMRG (red dots) and noninteracting ED (blue dots), showing excellent agreement. Figures 18(f)–18(j) further present the scaling of the ground-state energy difference $\Delta E = E_{\mathrm{DMRG}} - E_{\mathrm{ED}}$ for $|GS_N\rangle$ between DMRG and ED as a function of truncation error ϵ. All five samples reach $\epsilon < 10^{-10}$ with $\Delta E < 10^{-8}$. These results demonstrate that our DMRG setup converges to the correct ground states in this model and validate the reliability of the calculations employed in the interacting case.

We next introduce the DMRG setup for the quasi-1D Anderson-Hubbard model and present benchmark comparisons with noninteracting ED at $U = 0$ for five randomly chosen disorder realizations. For the $M = 2$ system, we consider system with size 2×60 at filling $n = 4/15$, enforcing both particle-number and spin conservation with $N_\uparrow = 32$, $N_\downarrow = 32$ for $|GS_N\rangle$, and $N_\uparrow = 31$, $N_\downarrow = 32$ for $|GS_{N-1}\rangle$. The number of kept states is increased sequentially following the array [50, 100, 200, 400, 800, 1000, 1500, 2000, 2500] with finite-lattice sweeps [25, 25, 25, 25, 25, 25, 5, 5, 5]. Five randomly chosen disorder samples are computed by both DMRG and noninteracting ED at $U = 0$. Figures 19(a)–19(e) show $\gamma(x)$ obtained from the two methods, exhibiting perfect agreement. Figures 19(f)–19(j) further display the scaling of the ground-state energy difference $\Delta E = E_{\mathrm{DMRG}} - E_{\mathrm{ED}}$ with truncation error ϵ, which exhibits an almost linear relation with intercepts close to zero. The final truncation error for all samples is below 10^{-8}.

For the $M = 3$ system of size 3×60 at the same filling $n = 4/15$, we perform calculations with $N_\uparrow = 48$, $N_\downarrow = 48$ for $|GS_N\rangle$ and $N_\uparrow = 47$, $N_\downarrow = 48$ for $|GS_{N-1}\rangle$. Here the number of kept states is increased following the array [50, 100, 200, 400, 800, 1000, 1500, 2000, 2500, 3000, 4000] with finite-lattice sweeps [25, 25, 25, 25, 25, 25, 15, 15, 5, 5, 5]. Again, five disorder realizations are randomly chosen for comparison between DMRG and noninteracting ED at $U = 0$. The $\gamma(x)$ results in Figs. 20(a)–20(e) show excellent agreement between the two methods, while the energy differences ΔE scale linearly with truncation error ϵ and extrapolate to zero, with final truncation errors below 10^{-6}, as shown in Fig. 20. These benchmarks confirm that our DMRG setup for the quasi-1D systems of width $M = 2$ and $M = 3$ yields well-converged ground states and provides reliable results for subsequent MDM analysis.

We finally introduce the DMRG setup for the quasi-1D modified spinless interacting model with selected bonds [Eq. (D1)] and present benchmark comparisons with noninteracting ED at $U = 0$ for five randomly chosen disorder realizations. All calculations are based on the quasi-1D systems of size $M \times L$ with $L = 30$ and $M = 2, 3, 4, 5$ with OBC and the bond configurations in Fig. 16 at filling

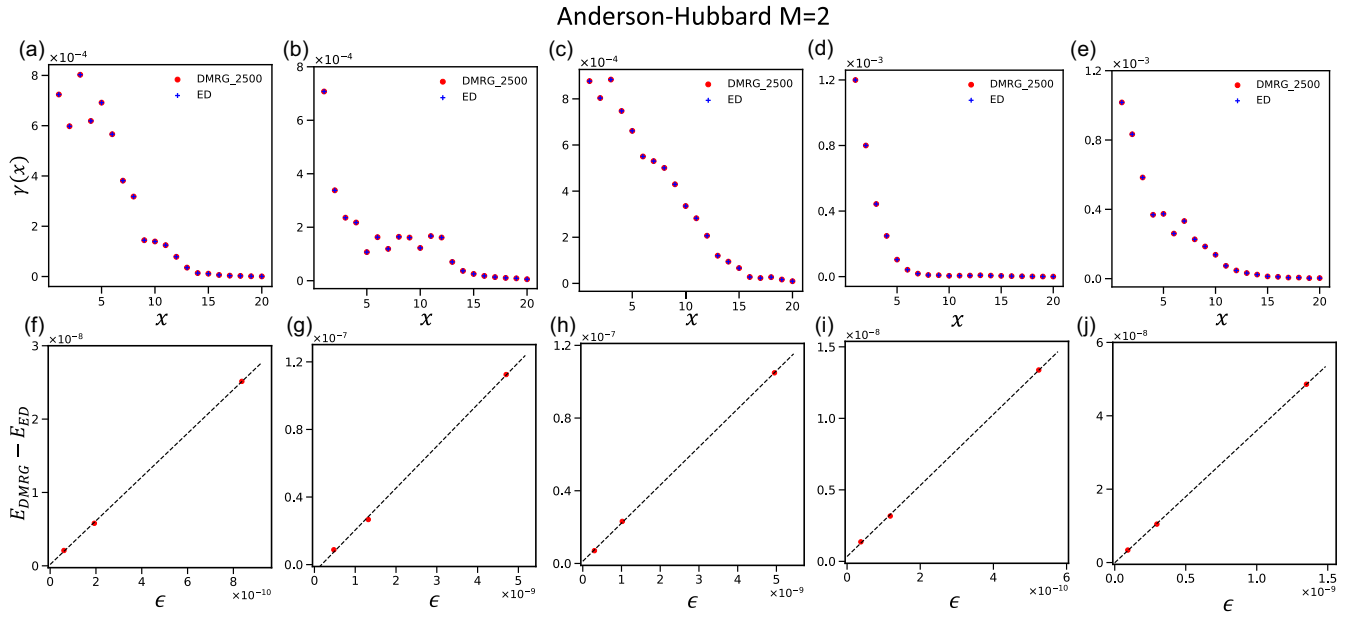

FIG. 19. Benchmarks for the quasi-1D Anderson–Hubbard [Eq. (13)] model of size 2×60 at $U = 0$, $W = 2.5t$ and filling $n = 4/15$ under OBC. (a)–(e) show $\gamma(x)$ as a function of x for five randomly chosen disorder samples. Red dots are DMRG results with the number of kept states gradually increased up to 2500, while blue dots are ED results. (f)–(j) The scaling of the ground-state energy difference $E_{\mathrm{DMRG}} - E_{\mathrm{ED}}$ for $|GS_N\rangle$ with truncation error ϵ for the corresponding samples. When performing the site average, the 10 sites closest to each boundary are excluded to minimize open-boundary effects.

$n = 5/15$. For the $M = 2$, 3, 4, 5 system, we enforce both particle-number and spin conservation with $N = 20$, 30, 40, 50 for $|GS_N\rangle$, and $N = 19$, 29, 39, 49 for $|GS_{N-1}\rangle$, respectively. The number of kept states is increased sequentially following the array [20, 20, 30, 30, 50, 50, 100] with finite-lattice sweeps [25, 25, 25, 25, 25, 10] for $M = 2$, [20, 20, 30, 30, 50, 50, 100, 200, 300, 400] with finite-lattice sweeps [25, 25, 25, 25, 25, 25, 15, 15, 5, 5] for $M = 3$, [20, 20, 30, 30, 50, 50, 100, 200, 300, 400, 600, 800] with finite-lattice sweeps [35, 35, 35, 35, 35, 35, 15,

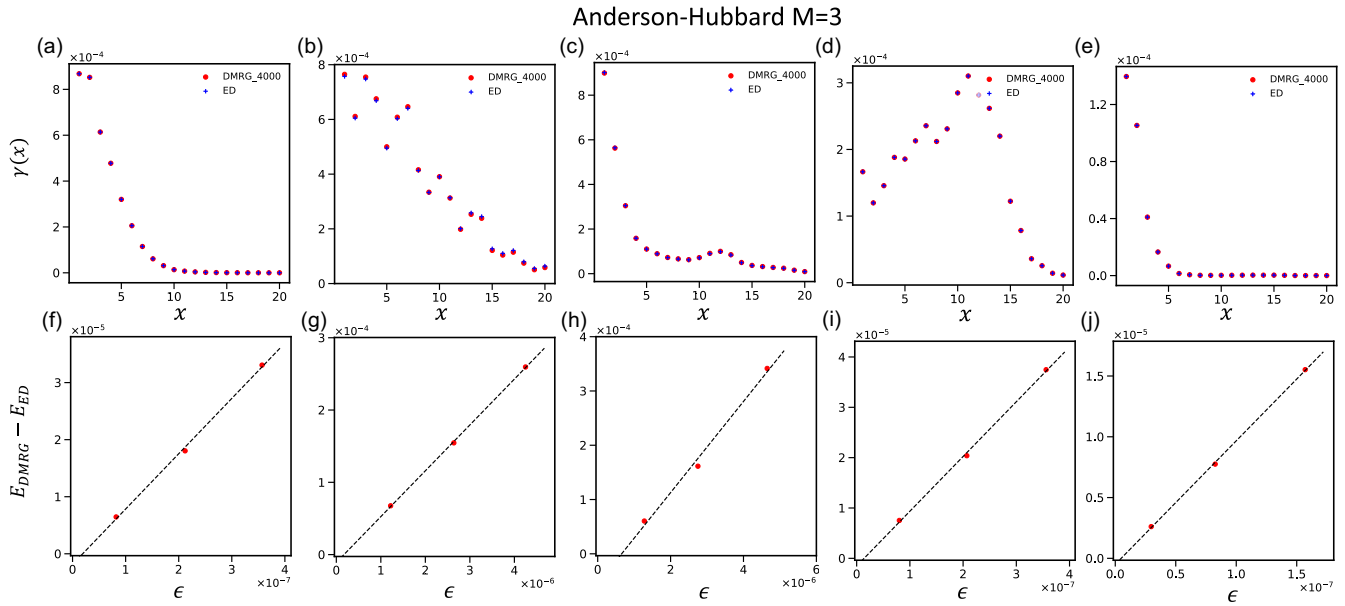

FIG. 20. Benchmarks for the quasi-1D Anderson-Hubbard [Eq. (13)] model of size 3×60 at $U = 0$, $W = 2.5t$ and filling $n = 4/15$ under OBC. (a)–(e) $\gamma(x)$ as a function of x for five randomly chosen disorder samples. Red dots are DMRG results with the number of kept states gradually increased up to 4000, while blue dots are ED results. (f)–(j) The scaling of the ground-state energy difference $E_{\mathrm{DMRG}} - E_{\mathrm{ED}}$ for $|GS_N\rangle$ with truncation error ϵ for the corresponding samples. When performing the site average, the 10 sites closest to each boundary are excluded to minimize open-boundary effects.

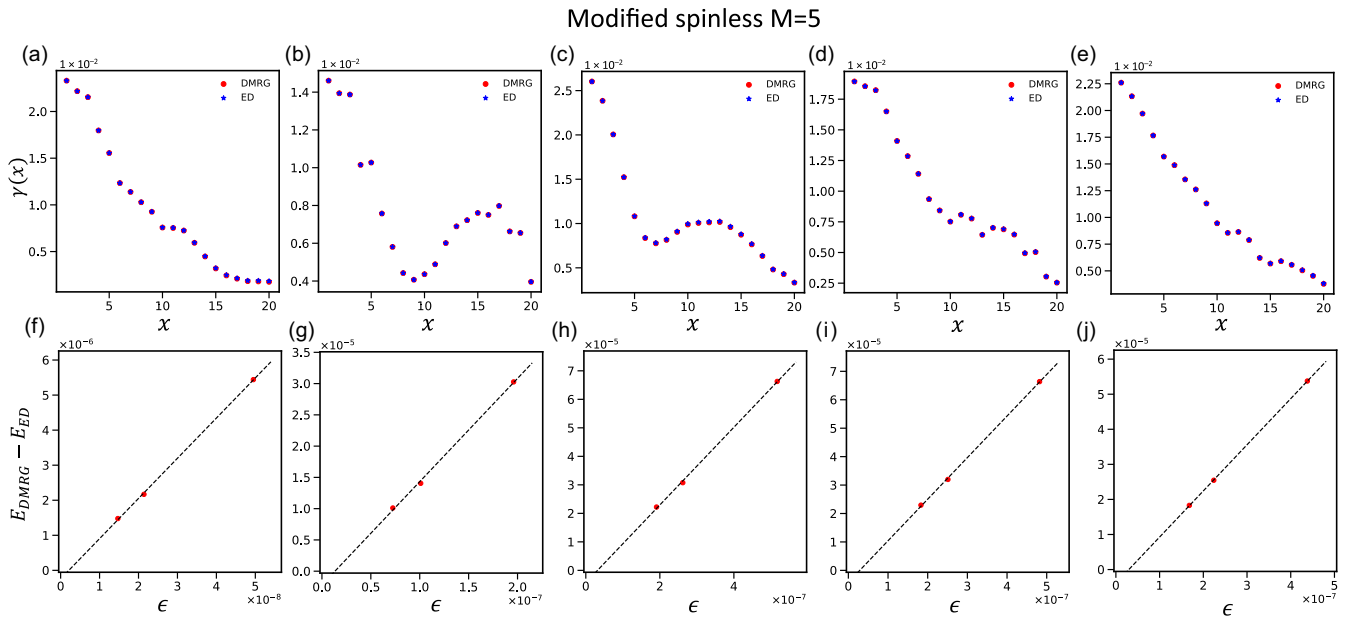

FIG. 21. Benchmarks for the quasi-1D modified spinless interacting model with selected bonds [Eq. (D1)] of size 5×30 at $V = 0$, $W = 2.0t$, and filling $n = 5/15$ under OBC. (a)–(e) $\gamma(x)$ as a function of x for five randomly chosen disorder samples. Red dots are DMRG results with the number of kept states gradually increased up to 1650, while blue dots are ED results. (f)–(j) The scaling of the ground-state energy difference $E_{\mathrm{DMRG}} - E_{\mathrm{ED}}$ for $|GS_N>$ with truncation error ϵ for the corresponding samples. When performing the site average, the 3 sites closest to each boundary are excluded to minimize open-boundary effects.

15, 15, 5, 5, 5] for $M = 4$, and [20, 20, 30, 30, 50, 50, 100, 200, 300, 400, 600, 800, 1000, 1200, 1500, 1650] with finite-lattice sweeps [50, 50, 50, 50, 50, 50,35,35,35, 15,15,15,3,3,3,2] for $M = 5$, respectively. Five randomly chosen disorder samples for the $M = 5$ quasi-1D systems are computed by both DMRG and noninteracting ED at $U = 0$, as shown in Fig. 21. Figures 21(a)–21(e) show $\gamma(x)$ obtained from the two methods, exhibiting perfect agreement. Figures 21(f)–21(j) further display the scaling of the ground-state energy difference $\Delta E = E_{\mathrm{DMRG}} - E_{\mathrm{ED}}$ with truncation error ϵ, which exhibits an almost linear relation with intercepts close to zero. The final truncation error for all samples is below 10^{-7}.

2. Supplementary results for the Anderson-Hubbard model

In this part, we present additional results for the quasi-1D Anderson-Hubbard model, focusing on the $\gamma(x)$ results corresponding to the finite-size scaling data corresponding

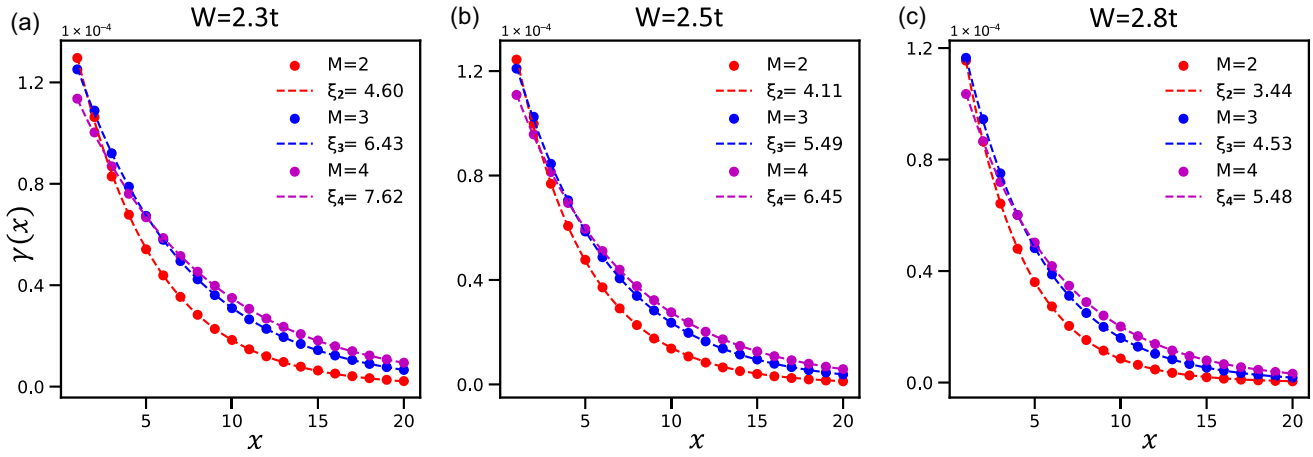

FIG. 22. Results of $\gamma(x)$ for the quasi-1D Anderson-Hubbard model at $U = 0t$ and filling $n = 4/15$. (a)–(c) The $\gamma(x)$ together with exponential fits results for $M = 2, 3, 4$ in the noninteracting case with disorder strengths $W = 2.3t, 2.5t, 2.8t$, respectively. These results are calculated by ED of noninteracting Hamiltonian. All disorder realizations are on systems of size $M \times L$ with $L = 60$ under OBC, and in the site averaging for each sample, the 10 sites nearest to each boundary are excluded to minimize open-boundary effects. Each curve is calculated by averaging 8000 disorder realizations.

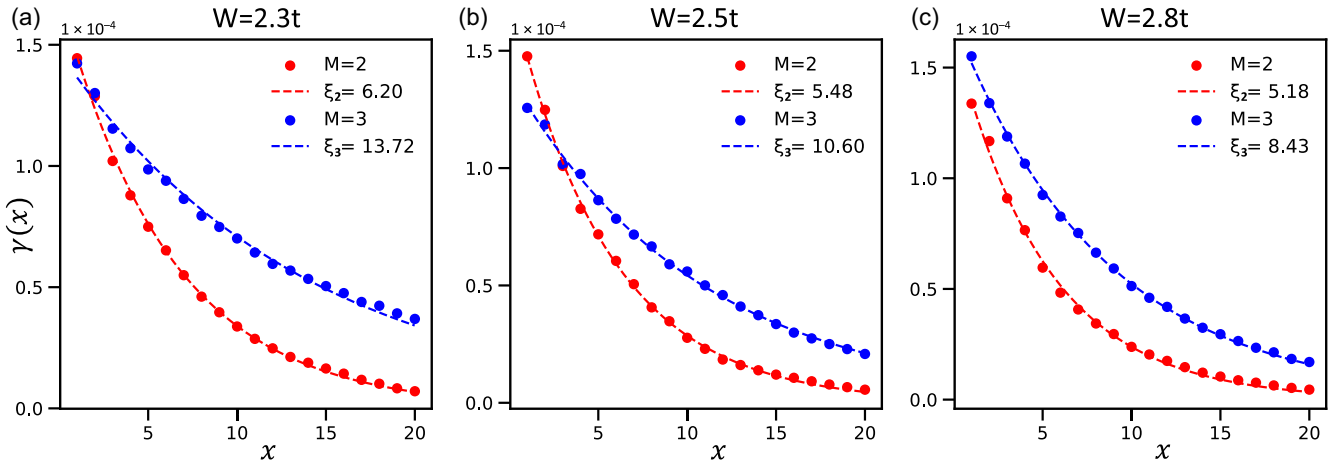

FIG. 23. Results of $\gamma(x)$ for the quasi-1D Anderson-Hubbard model at $U = 4t$ and filling $n = 4/15$. (a)–(c) show the $\gamma(x)$ together with exponential fits results for $M = 2, 3, 4$ with disorder strengths $W = 2.3t, 2.5t, 2.8t$, respectively. These results are calculated by DMRG. All disorder realizations are on systems of size $M \times L$ with $L = 60$ under OBC, and in the site averaging for each sample, the 10 sites nearest to each boundary are excluded to minimize open-boundary effects. Each curve is calculated by averaging 100 disorder realizations.

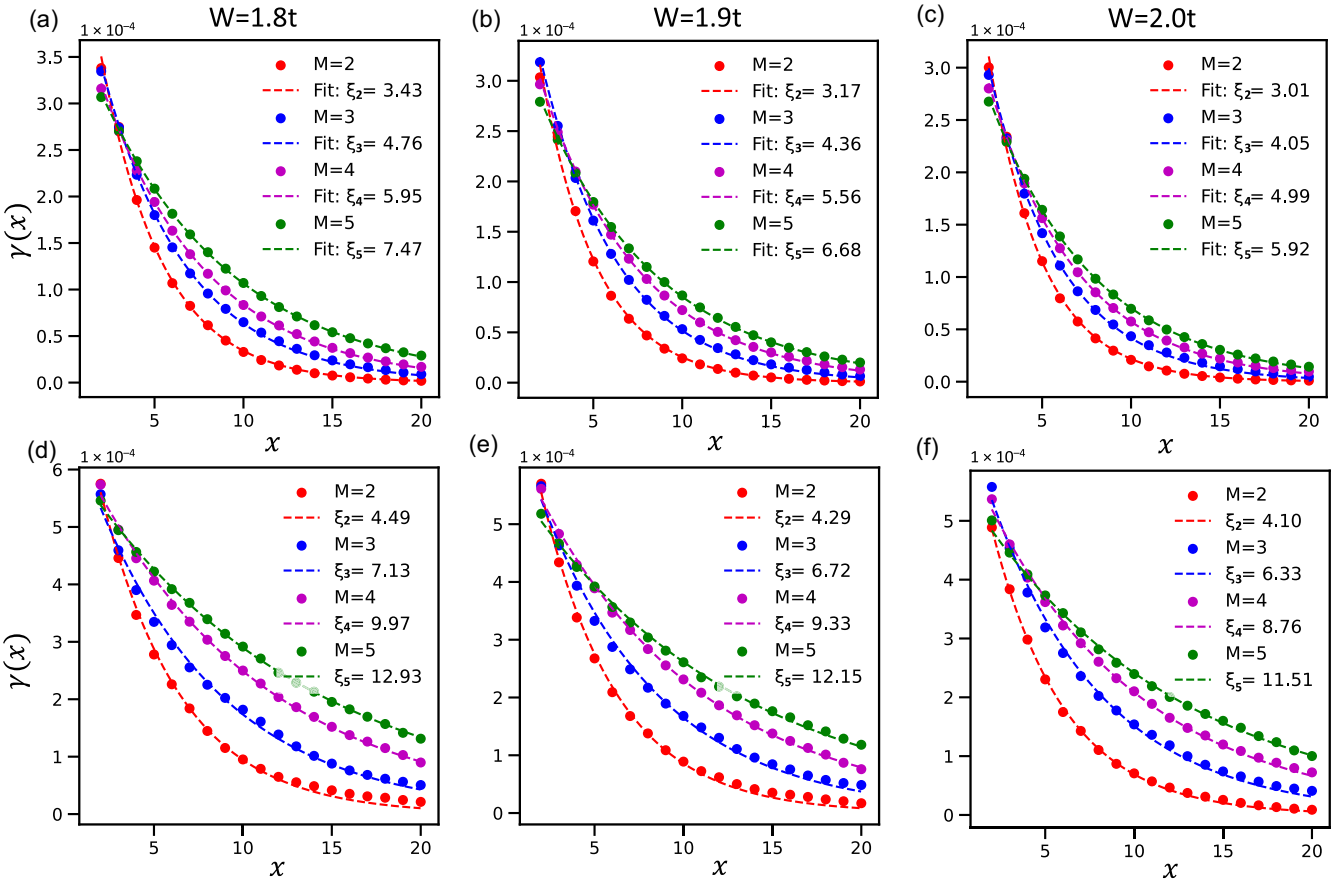

FIG. 24. Results of $\gamma(x)$ for the quasi-1D modified spinless interacting model with selected bonds. (a)–(c) The $\gamma(x)$ together with exponential fits results for $M = 2, 3, 4, 5$ in the noninteracting case with disorder strengths $W = 1.8t, 1.9t, 2.0t$ and interaction strength $V = 0t$, respectively. These results are calculated by ED of noninteracting Hamiltonian. Each curve is calculated by averaging 2000 disorder realizations. (d)–(e) show the $\gamma(x)$ together with exponential fits results for $M = 2, 3, 4, 5$ with disorder strengths $W = 1.8t, 1.9t, 2.0t$ and interaction strength $V = 2.5t$, respectively. These results are calculated by DMRG. Each curve is calculated by averaging 200 disorder realizations. In the site averaging for each sample, the 3 sites nearest to each boundary are excluded to minimize open-boundary effects. All disorder realizations are on systems of size $M \times L$ with $L = 30$ under OBC at filling $n = 5/15$, and the bond configurations are shown in Fig. 16.

to the finite-size scaling shown in Figs. 7(c) and 7(d). For the noninteracting case ($U = 0$), Fig. 22 shows $\gamma(x)$ at disorder strengths $W = 2.3t, 2.5t, 2.8t$ for bars of width $M = 2, 3, 4$. In all cases, $\gamma(x)$ exhibits a clear exponential decay, $\gamma(x) \sim e^{-x/\xi_M}$, from which localization lengths ξ_M can be directly extracted. Remarkably, even in the presence of strong Hubbard interactions, $\gamma(x)$ retains a simple exponential form, as shown in Fig. 23 for $M = 2$, 3 at $U = 4t$ and the same disorder strengths. Moreover, for fixed M and W, the localization length at $U = 4t$ is significantly enhanced compared to the $U = 0$ case, demonstrating the delocalizing effect of Hubbard interactions in disordered systems. This enhancement increases with M, ultimately leading to the emergence of a correlated metallic state at finite U and W.

3. Supplementary results for the modified spinless interacting model

In this part, we present additional results for the quasi-1D modified spinless interacting model with selected bonds, focusing on the $\gamma(x)$ results corresponding to the finite-size scaling data corresponding to the finite-size scaling shown in Figs. 17(c) and 17(d). For the noninteracting case ($V = 0$), Figs. 24(a)–24(c) shows $\gamma(x)$ at disorder strengths $W = 1.8t, 1.9t, 2.0t$ for bars of width $M = 2, 3, 4, 5$. In all cases, $\gamma(x)$ exhibits a clear exponential decay, $\gamma(x) \sim e^{-x/\xi_M}$, from which localization lengths ξ_M can be directly extracted. Remarkably, even in the presence of strong Hubbard interactions, $\gamma(x)$ retains a simple exponential form, as shown in Figs. 24(d)–24(f) for $M = 2, 3, 4, 5$ at $V = 2.5t$ and the same disorder strengths. Moreover, for fixed M and W, the localization length at $V = 2.5t$ is significantly enhanced compared to the $U = 0$ case, demonstrating the delocalizing effect of repulsive nearest-neighbor interactions V. This enhancement increases with M, ultimately leading to the emergence of a correlated metallic state at finite U and W. These trends are fully consistent with the physical picture of interaction-disorder competition in the Anderson-Hubbard model discussed in the main text.

[1] D. J. Thouless, *Electrons in disordered systems and the theory of localization*, Phys. Rep. **13**, 93 (1974).

[2] Patrick A. Lee and T. V. Ramakrishnan, *Disordered electronic systems*, Rev. Mod. Phys. **57**, 287 (1985).

[3] B. L. Altshuler and A. G. Aronov, *Electron-Electron Interactions in Disordered Systems*, edited by A. L. Efros and M. Pollak (North Holland, Amsterdam, 1985), Vol. 1, p. 155.

[4] B. Kramer and A. MacKinnon, *Localization: Theory and experiment*, Rep. Prog. Phys. **56**, 1469 (1993).

[5] Elihu Abrahams, *50 years of Anderson Localization* (World Scientific, Singapore, 2010).

[6] P. W. Anderson, *Absence of diffusion in certain random lattices*, Phys. Rev. **109**, 1492 (1958).

[7] E. Abrahams, P. W. Anderson, D. C. Licciardello, and T. V. Ramakrishnan, *Scaling theory of localization: Absence of quantum diffusion in two dimensions*, Phys. Rev. Lett. **42**, 673 (1979).

[8] D. C. Licciardello and D. J. Thouless, *Constancy of minimum metallic conductivity in two dimensions*, Phys. Rev. Lett. **35**, 1475 (1975).

[9] Franz J. Wegner, *Electrons in disordered systems. scaling near the mobility edge*, Z. Phys. B Condens. Matter **25**, 327 (1976).

[10] H. G. Schuster, *On a relation between the mobility edge problem and an isotropicxy model*, Z. Phys. B Condens. Matter **31**, 99 (1978).

[11] B. L. Altshuler and A. G. Aronov, *Zero bias anomaly in tunnel resistance and electron-electron interaction*, Solid State Commun. **30**, 115 (1979).

[12] Boris L. Altshuler and Andrey Aronov, *Contribution to the theory of disordered metals in strongly doped semiconductors*, J. Exp. Theor. Phys. (1979), https://www.semanticscholar.org/paper/Contribution-to-the-theory-of-disordered-metals-in-Altshuler-Aronov/86ee0dfe43c40cc19e904348c6858f0d88c632a4.

[13] B. L. Altshuler, A. G. Aronov, and P. A. Lee, *Interaction effects in disordered Fermi systems in two dimensions*, Phys. Rev. Lett. **44**, 1288 (1980).

[14] A. MacKinnon and B. Kramer, *One-parameter scaling of localization length and conductance in disordered systems*, Phys. Rev. Lett. **47**, 1546 (1981).

[15] Paul Soven, *Coherent-potential model of substitutional disordered alloys*, Phys. Rev. **156**, 809 (1967).

[16] V. Dobrosavljević, A. A. Pastor, and B. K. Nikolić, *Typical medium theory of Anderson localization: A local order parameter approach to strong-disorder effects*, Europhys. Lett. **62**, 76 (2003).

[17] Hanna Terletska, Yi Zhang, Ka-Ming Tam, Tom Berlijn, Liviu Chioncel, N. S. Vidhyadhiraja, and Mark Jarrell, *Systematic quantum cluster typical medium method for the study of localization in strongly disordered electronic systems*, Appl. Sci. **8**, 2401 (2018).

[18] Konstantin Efetov, *Supersymmetry in Disorder and Chaos* (Cambridge University Press, Cambridge, England, 1999).

[19] A. M. Finkel'shtein, *Influence of Coulomb interaction on the properties of disordered metals*, Sov. J. Exp. Theor. Phys. **57**, 97 (1983), https://ui.adsabs.harvard.edu/abs/1983JETP...57...97F/abstract.

[20] Dmitry A. Abanin, Ehud Altman, Immanuel Bloch, and Maksym Serbyn, *Colloquium: Many-body localization, thermalization, and entanglement*, Rev. Mod. Phys. **91**, 021001 (2019).

[21] A. MacKinnon and B. Kramer, *The scaling theory of electrons in disordered solids: Additional numerical results*, Z. Phys. B Condens. Matter **53**, 1 (1983).

[22] J. L. Pichard and G. Sarma, *Finite size scaling approach to Anderson localisation*, J. Phys. C **14**, L127 (1981).

[23] A. MacKinnon, *Critical exponents for the metal-insulator transition*, J. Phys. Condens. Matter **6**, 2511 (1994).

[24] B. Velický, S. Kirkpatrick, and H. Ehrenreich, *Single-site approximations in the electronic theory of simple binary alloys*, Phys. Rev. **175**, 747 (1968).

[25] J. T. Edwards and D. J. Thouless, *Numerical studies of localization in disordered systems*, J. Phys. C **5**, 807 (1972).
[26] K. B. Efetov, A. I. Larkin, and D. E. Kheml'Nitskiĭ, *Interaction of diffusion modes in the theory of localization*, Sov. J. Exp. Theor. Phys. **52**, 568 (1980), https://ui.adsabs.harvard.edu/abs/1980JETP...52..568E/abstract.
[27] Franz Wegner, *The mobility edge problem: Continuous symmetry and a conjecture*, Z. Phys. B Condens. Matter **35**, 207 (1979).
[28] Ferdinand Evers and Alexander D. Mirlin, *Anderson transitions*, Rev. Mod. Phys. **80**, 1355 (2008).
[29] D. Vollhardt and P. Wölfle, *Anderson localization in $d < 2$ dimensions: A self-consistent diagrammatic theory*, Phys. Rev. Lett. **45**, 842 (1980).
[30] Olaf Schenk, Matthias Bollhöfer, and Rudolf A. Römer, *On large-scale diagonalization techniques for the Anderson model of localization*, SIAM J. Sci. Comput. **28**, 963 (2006).
[31] F. Wegner, *Inverse participation ratio in $2 + \epsilon$ dimensions*, Z. Phys. B Condens. Matter **36**, 209 (1980).
[32] Shinobu Hikami, *Localization length and inverse participation ratio of two dimensional electron in the quantized hall effect*, Prog. Theor. Phys. **76**, 1210 (1986).
[33] Alexander D. Mirlin, *Statistics of energy levels and eigenfunctions in disordered systems*, Phys. Rep. **326**, 259 (2000).
[34] E. Hofstetter and M. Schreiber, *Statistical properties of the eigenvalue spectrum of the three-dimensional Anderson Hamiltonian*, Phys. Rev. B **48**, 16979 (1993).
[35] B. I. Shklovskii, B. Shapiro, B. R. Sears, P. Lambrianides, and H. B. Shore, *Statistics of spectra of disordered systems near the metal-insulator transition*, Phys. Rev. B **47**, 11487 (1993).
[36] J. Šuntajs, T. Prosen, and L. Vidmar, *Spectral properties of three-dimensional Anderson model*, Ann. Phys. (Amsterdam) **435**, 168469 (2021).
[37] Martin Janssen, *Statistics and scaling in disordered mesoscopic electron systems*, Phys. Rep. **295**, 1 (1998).
[38] A. D. Mirlin and F. Evers, *Multifractality and critical fluctuations at the Anderson transition*, Phys. Rev. B **62**, 7920 (2000).
[39] Alberto Rodriguez, Louella J. Vasquez, Keith Slevin, and Rudolf A. Römer, *Multifractal finite-size scaling and universality at the Anderson transition*, Phys. Rev. B **84**, 134209 (2011).
[40] Gil Refael and Joel E. Moore, *Entanglement entropy of random quantum critical points in one dimension*, Phys. Rev. Lett. **93**, 260602 (2004).
[41] Nicolas Laflorencie, *Scaling of entanglement entropy in the random singlet phase*, Phys. Rev. B **72**, 140408(R) (2005).
[42] Jens H. Bardarson, Frank Pollmann, and Joel E. Moore, *Unbounded growth of entanglement in models of many-body localization*, Phys. Rev. Lett. **109**, 017202 (2012).
[43] Richard Berkovits, *Entanglement entropy in a one-dimensional disordered interacting system: The role of localization*, Phys. Rev. Lett. **108**, 176803 (2012).
[44] Bela Bauer and Chetan Nayak, *Area laws in a many-body localized state and its implications for topological order*, J. Stat. Mech. (**2013**) P09005.
[45] An Zhao, Rui-Lin Chu, and Shun-Qing Shen, *Finite-size scaling of entanglement entropy at the Anderson transition with interactions*, Phys. Rev. B **87**, 205140 (2013).
[46] Mohammad Pouranvari, Yuhui Zhang, and Kun Yang, *Entanglement area law in disordered free fermion Anderson model in one, two, and three dimensions*, Adv. Condens. Matter Phys. **2015**, 397630 (2015).
[47] Raffaele Resta and Sandro Sorella, *Electron localization in the insulating state*, Phys. Rev. Lett. **82**, 370 (1999).
[48] R. Resta, *The insulating state of matter: A geometrical theory*, Eur. Phys. J. B **79**, 121 (2011).
[49] Nicola Marzari, Arash A. Mostofi, Jonathan R. Yates, Ivo Souza, and David Vanderbilt, *Maximally localized Wannier functions: Theory and applications*, Rev. Mod. Phys. **84**, 1419 (2012).
[50] Balázs Hetényi, Sel çuk Parlak, and Mohammad Yahyavi, *Scaling and renormalization in the modern theory of polarization: Application to disordered systems*, Phys. Rev. B **104**, 214207 (2021).
[51] L. D. Landau and E. M. Lifshitz, *Quantum Mechanics: Non-Relativistic Theory* (Elsevier, New York, 2013), Vol. 3.
[52] Steven R. White, *Density matrix formulation for quantum renormalization groups*, Phys. Rev. Lett. **69**, 2863 (1992).
[53] U. Schollwöck, *The density-matrix renormalization group*, Rev. Mod. Phys. **77**, 259 (2005).
[54] Cornelius Lanczos, *An iteration method for the solution of the eigenvalue problem of linear differential and integral operators*, J. Res. Natl. Bur. Stand. **45**, 255 (1950).
[55] Yousef Saad, *Numerical Methods for Large Eigenvalue Problems*, 2nd ed. (SIAM, Philadelphia, 2011).
[56] Keith Slevin and Tomi Ohtsuki, *Corrections to scaling at the Anderson transition*, Phys. Rev. Lett. **82**, 382 (1999).
[57] Keith Slevin and Tomi Ohtsuki, *Critical exponent for the Anderson transition in the three-dimensional orthogonal universality class*, New J. Phys. **16**, 015012 (2014).
[58] N. F. Mott, *Electrons in disordered structures*, Adv. Phys. **16**, 49 (1967).
[59] N. Mott, *The mobility edge since 1967*, J. Phys. C **20**, 3075 (1987).
[60] B. R. Bulka, B. Kramer, and A. MacKinnon, *Mobility edge in the three dimensional Anderson model*, Z. Phys. B Condens. Matter **60**, 13 (1985).
[61] B. Bulka, M. Schreiber, and B. Kramer, *Localization, quantum interference, and the metal-insulator transition*, Z. Phys. B Condens. Matter **66**, 21 (1987).
[62] Shinobu Hikami, Anatoly I. Larkin, and Yosuke Nagaoka, *Spin-orbit interaction and magnetoresistance in the two dimensional random system*, Prog. Theor. Phys. **63**, 707 (1980).
[63] Gerd Bergmann, *Weak localization in thin films: A time-of-flight experiment with conduction electrons*, Phys. Rep. **107**, 1 (1984).
[64] Alexander Altland and Martin R. Zirnbauer, *Nonstandard symmetry classes in mesoscopic normal-superconducting hybrid structures*, Phys. Rev. B **55**, 1142 (1997).
[65] Yoichi Asada, Keith Slevin, and Tomi Ohtsuki, *Anderson transition in two-dimensional systems with spin-orbit coupling*, Phys. Rev. Lett. **89**, 256601 (2002).

[66] Ying Su and X. R. Wang, *Role of spin degrees of freedom in Anderson localization of two-dimensional particle gases with random spin-orbit interactions*, Phys. Rev. B **98**, 224204 (2018).
[67] Krzysztof Byczuk, Walter Hofstetter, and Dieter Vollhardt, *Anderson localization vs. Mott–Hubbard metal–insulator transition in disordered, interacting lattice fermion systems*, Int. J. Mod. Phys. B **24**, 1727 (2010).
[68] H. Terletska, C. E. Ekuma, C. Moore, K.-M. Tam, J. Moreno, and M. Jarrell, *Study of off-diagonal disorder using the typical medium dynamical cluster approximation*, Phys. Rev. B **90**, 094208 (2014).
[69] Yi Zhang, Hanna Terletska, C. Moore, Chinedu Ekuma, Ka-Ming Tam, Tom Berlijn, Wei Ku, Juana Moreno, and Mark Jarrell, *Study of multiband disordered systems using the typical medium dynamical cluster approximation*, Phys. Rev. B **92**, 205111 (2015).
[70] C. E. Ekuma, S.-X. Yang, H. Terletska, K.-M. Tam, N. S. Vidhyadhiraja, J. Moreno, and M. Jarrell, *Metal-insulator transition in a weakly interacting disordered electron system*, Phys. Rev. B **92**, 201114(R) (2015).
[71] Yi Zhang, R. Nelson, Elisha Siddiqui, K.-M. Tam, U. Yu, T. Berlijn, W. Ku, N. S. Vidhyadhiraja, J. Moreno, and M. Jarrell, *Generalized multiband typical medium dynamical cluster approximation: Application to* (Ga, Mn) N, Phys. Rev. B **94**, 224208 (2016).
[72] Yi Zhang, R. Nelson, K.-M. Tam, W. Ku, U. Yu, N. S. Vidhyadhiraja, H. Terletska, J. Moreno, M. Jarrell, and T. Berlijn, *Origin of localization in* Ti-*doped* Si, Phys. Rev. B **98**, 174204 (2018).
[73] Krzysztof Byczuk, Walter Hofstetter, and Dieter Vollhardt, *Mott-Hubbard transition versus Anderson localization in correlated electron systems with disorder*, Phys. Rev. Lett. **94**, 056404 (2005).
[74] T. H. Y. Nguyen, D. A. Le, and A. T. Hoang, *Anderson localization in the Anderson–Hubbard model with site-dependent interactions*, New J. Phys. **24**, 053054 (2022).
[75] Gerald Knizia and Garnet Kin-Lic Chan, *Density matrix embedding: A simple alternative to dynamical mean-field theory*, Phys. Rev. Lett. **109**, 186404 (2012).
[76] Sebastian Wouters, Carlos A. Jiménez-Hoyos, Qiming Sun, and Garnet K. L. Chan, *A practical guide to density matrix embedding theory in quantum chemistry*, J. Chem. Theory Comput. **12**, 2706 (2016).
[77] C. Castellani, C. Di Castro, P. A. Lee, and M. Ma, *Interaction-driven metal-insulator transitions in disordered fermion systems*, Phys. Rev. B **30**, 527 (1984).
[78] L. Fleishman and P. W. Anderson, *Interactions and the Anderson transition*, Phys. Rev. B **21**, 2366 (1980).
[79] D. M. Basko, I. L. Aleiner, and B. L. Altshuler, *Metal–insulator transition in a weakly interacting many-electron system with localized single-particle states*, Ann. Phys. (Amsterdam) **321**, 1126 (2006).
[80] Soumya Bera, Henning Schomerus, Fabian Heidrich-Meisner, and Jens H. Bardarson, *Many-body localization characterized from a one-particle perspective*, Phys. Rev. Lett. **115**, 046603 (2015).
[81] Talía L. M. Lezama, S. Bera, H. Schomerus, F. Heidrich-Meisner, and J. H. Bardarson, *One-particle density matrix occupation spectrum of many-body localized states after a global quench*, Phys. Rev. B **96**, 060202(R) (2017).
[82] Takahiro Orito and Ken-Ichiro Imura, *Multifractality and Fock-space localization in many-body localized states: One-particle density matrix perspective*, Phys. Rev. B **103**, 214206 (2021).
[83] S. V. Kravchenko and M. P. Sarachik, *Metal–insulator transition in two-dimensional electron systems*, Rep. Prog. Phys. **67**, 1 (2003).
[84] S. V. Kravchenko, G. V. Kravchenko, J. E. Furneaux, V. M. Pudalov, and M. D'Iorio, *Possible metal-insulator transition at* $b = 0$ *in two dimensions*, Phys. Rev. B **50**, 8039 (1994).
[85] S. V. Kravchenko, Whitney E. Mason, G. E. Bowker, J. E. Furneaux, V. M. Pudalov, and M. D'Iorio, *Scaling of an anomalous metal-insulator transition in a two-dimensional system in silicon at* $b = 0$, Phys. Rev. B **51**, 7038 (1995).
[86] S. V. Kravchenko, D. Simonian, M. P. Sarachik, W. Mason, and J. E. Furneaux, *Electric field scaling at a* $b = 0$ *metal-insulator transition in two dimensions*, Phys. Rev. Lett. **77**, 4938 (1996).
[87] S. Anissimova, S. V. Kravchenko, A. Punnoose, A. M. Finkel'stein, and T. M. Klapwijk, *Flow diagram of the metal-insulator transition in two dimensions*, Nat. Phys. **3**, 707 (2007).
[88] Elihu Abrahams, Sergey V. Kravchenko, and Myriam P. Sarachik, *Metallic behavior and related phenomena in two dimensions*, Rev. Mod. Phys. **73**, 251 (2001).
[89] P. J. H. Denteneer, R. T. Scalettar, and N. Trivedi, *Conducting phase in the two-dimensional disordered Hubbard model*, Phys. Rev. Lett. **83**, 4610 (1999).
[90] P. J. H. Denteneer, R. T. Scalettar, and N. Trivedi, *Particle-hole symmetry and the effect of disorder on the Mott-Hubbard insulator*, Phys. Rev. Lett. **87**, 146401 (2001).
[91] Dariush Heidarian and Nandini Trivedi, *Inhomogeneous metallic phase in a disordered Mott insulator in two dimensions*, Phys. Rev. Lett. **93**, 126401 (2004).
[92] Prabuddha B. Chakraborty, Krzysztof Byczuk, and Dieter Vollhardt, *Interacting lattice electrons with disorder in two dimensions: Numerical evidence for a metal-insulator transition with a universal critical conductivity*, Phys. Rev. B **84**, 035121 (2011).
[93] Geneviève Fleury and Xavier Waintal, *Many-body localization study in low-density electron gases: Do metals exist in two dimensions?*, Phys. Rev. Lett. **101**, 226803 (2008).
[94] Bhargavi Srinivasan, Giuliano Benenti, and Dima L. Shepelyansky, *Delocalizing effect of the Hubbard repulsion for electrons on a two-dimensional disordered lattice*, Phys. Rev. B **67**, 205112 (2003).
[95] Alexander Punnoose and Alexander M. Finkel'stein, *Metal-insulator transition in disordered two-dimensional electron systems*, Science **310**, 289 (2005).
[96] Thomas Vojta, Frank Epperlein, and Michael Schreiber, *Do interactions increase or reduce the conductance of disordered electrons? it depends!*, Phys. Rev. Lett. **81**, 4212 (1998).
[97] Dariush Heidarian and Nandini Trivedi, *Inhomogeneous metallic phase in a disordered Mott insulator in two dimensions*, Phys. Rev. Lett. **93**, 126401 (2004).

[98] Patrick Bultinck, Dorien Clarisse, Paul W. Ayers, and Ramon Carbo-Dorca, *The Fukui matrix: A simple approach to the analysis of the Fukui function and its positive character*, Phys. Chem. Chem. Phys. **13**, 6110 (2011).

[99] Miguel Gonçalves, J. H. Pixley, B. Amorim, Eduardo V. Castro, and Pedro Ribeiro, *Short-range interactions are irrelevant at the quasiperiodicity-driven Luttinger liquid to Anderson glass transition*, Phys. Rev. B **109**, 014211 (2024).

[100] Jonathan M. Carter and Angus MacKinnon, *Disorder and interactions in one-dimensional systems*, Phys. Rev. B **72**, 024208 (2005).

[101] P. Schmitteckert, T. Schulze, C. Schuster, P. Schwab, and U. Eckern, *Anderson localization versus delocalization of interacting fermions in one dimension*, Phys. Rev. Lett. **80**, 560 (1998).

[102] Matthew Fishman, Steven R. White, and E. Miles Stoudenmire, *The ITENSOR software library for tensor network calculations*, SciPost Phys. Codebases 4 (2022).

[103] Matthew Fishman, Steven R. White, and E. Miles Stoudenmire, *Codebase release 0.3 for ITENSOR*, SciPost Phys. Codebases 4 (2022).

[104] Thierry Giamarchi, *Quantum Physics in One Dimension* (Clarendon Press, New York, 2003), Vol. 121.

[105] Daniel C. Mattis, *New wave-operator identity applied to the study of persistent currents in 1D*, J. Math. Phys. (N.Y.) **15**, 609 (1974).

[106] A. Luther and I. Peschel, *Fluctuation conductivity and lattice stability in one dimension*, Phys. Rev. Lett. **32**, 992 (1974).

[107] A. Luther and V. J. Emery, *Backward scattering in the one-dimensional electron gas*, Phys. Rev. Lett. **33**, 589 (1974).

[108] W. Apel, *Conductivity of a one-dimensional system of interacting fermions in a random potential*, J. Phys. C **15**, 1973 (1982).

[109] W. Apel and T. M. Rice, *Combined effect of disorder and interaction on the conductance of a one-dimensional fermion system*, Phys. Rev. B **26**, 7063 (1982).

[110] T. Giamarchi and H. J. Schulz, *Anderson localization and interactions in one-dimensional metals*, Phys. Rev. B **37**, 325 (1988).

[111] T. Giamarchi and H. J. Schulz, *Localization and interaction in one-dimensional quantum fluids*, Europhys. Lett. **3**, 1287 (1987).

[112] Y. Weiss, M. Goldstein, and R. Berkovits, *Friedel oscillations in disordered quantum wires: Influence of electron-electron interactions on the localization length*, Phys. Rev. B **75**, 064209 (2007).

[113] An Zhao, Rui-Lin Chu, and Shun-Qing Shen, *Finite-size scaling of entanglement entropy at the Anderson transition with interactions*, Phys. Rev. B **87**, 205140 (2013).

[114] Richard Berkovits, *Entanglement properties and quantum phases for a fermionic disordered one-dimensional wire with attractive interactions*, Phys. Rev. Lett. **115**, 206401 (2015).

[115] J. I. Cirac, D. Pérez-García, N. Schuch, and F. Verstraete, *Matrix product states and projected entangled pair states: Concepts, symmetries, theorems*, Rev. Mod. Phys. **93**, 045003 (2021).

[116] Tao Xiang, *Density Matrix and Tensor Network Renormalization* (Cambridge University Press, Cambridge, England, 2023).

[117] Z. Qi, Y. Zhang, M. Qin, H. Weng, and K. Jiang, Code and data for: Anderson Localization: A Density Matrix Approach, Github v1.0 (2026), https://github.com/ZiyueQiphys/Density-Matrix-for-Anderson-Localization.

[118] Harry Furstenberg and Harry Kesten, *Products of random matrices*, Ann. Math. Stat. **31**, 457 (1960).

[119] Andrea Crisanti, Giovanni Paladin, and Angelo Vulpiani, *Products of Random Matrices, in Statistical Physics* (Springer Berlin, Heidelberg, 1993).

[120] Emile Le Page, *Theoremes limites pour les produits de matrices aleatoires*, in *Probability Measures on Groups*, edited by Herbert Heyer (Springer, Berlin, Heidelberg, 1982), pp. 258–303.

[121] C. W. J. Beenakker, *Random-matrix theory of quantum transport*, Rev. Mod. Phys. **69**, 731 (1997).